PHOTOINACTIVATION OF PROTEINS BY MOLECULAR HYPERTHERMIA

by

Peiyuan Kang

APPROVED BY SUPERVISORY COMMITTEE:

Dr. Zhenpeng Qin

Dr. Jeremiah J. Gassensmith

Dr. Fatemeh Hassanipour

Dr. Theodore J. Price

To my parents and my family

PHOTOINACTIVATION OF PROTEINS BY MOLECULAR HYPERTHERMIA

by

PEIYUAN KANG, MS

DISSERTATION

Presented to the Faculty of

The University of Texas at Dallas

in Partial Fulfillment

of the Requirements

for the Degree of

DOCTOR OF PHILOSOPHY IN

MECHANICAL ENGINEERING

THE UNIVERSITY OF TEXAS AT DALLAS

May 2020

ACKNOWLEDGMENTS

First and foremost, I would like to express the deepest appreciation to my advisor, Dr. Zhenpeng Qin for his continuous support of my PhD study and research. He is a great mentor who shows me the beauty of science and whose passion inspired me to persevere. Without his patience and guidance, it would be impossible for me to finish this work.

I would like to thank the rest of my dissertation committee: Dr. Jeremiah Gassensmith, Dr. Fatemeh Hassanipour and Dr. Theodore Price for their insightful comments and encouragement. Their discussion and questions inspired me to think more deeply about my research from different angles.

I would like to acknowledge current and former members of the Nano-Thermal Bioengineering Laboratory (NTBEL) for their help in my research and in my life. I am grateful to work in this collaborative team. They are intelligent researchers who do excellent research and inspire me to do my best. Special thanks to Dr. Xiuying Li who not only provided help and advice on my laboratory work but also gave me a hand in difficult times.

I was privileged to work with many collaborators who contributed significantly to this dissertation. Each conversation with Dr. Steven Nielsen is fruitful and he gives us many instrumental suggestions on modeling and simulations. Dr. Jaona "Fidy" Randrianalisoa is a great collaborator and a great teacher who gives me many inspiring thoughts about nanophotonics. Thanks, Dr. Hoyt for providing the photoacoustic equipment for this project and Dr. D'Arcy for helpful discussions. Thanks, Dr. Elisabetta Dejana and Dr. Monica Giannotta for providing antibodies to the MH project. Thanks to Dr. Paul Slesinger for providing the CNiFER cells to us. Special thanks to Dr.

Jamie Moy for teaching me the DRG extraction skill. Thanks to Dr. Zifan Che for training me TEM for hours voluntarily and patiently.

I would like to thank my friends: Dr. Xiaowei Zhu, Dr. Chao Wang, Dr. Lu Zhan, Dr. Tingge Xu, Dr. Zhe Xu, Dr. Xuemin Wang, Dr. Lianjun Wu, Dr. Mohammad Karim, Dr. Chao Wang (from Dr. Minary's Lab.), Ms. Yang Wang, Mr. Yi Guo, Ms. Lin Jiang, Mr. Fenglin Zhou, Mr. Changlong Cui, Mr. Zhongyou Wu, Ms. Candace Benjamin, Mr. Haowei Tai and so on. I want to especially express my sincere appreciation to Dr. Zhuo Chen and Dr. Jonghae Youn who are not only my collaborators but also my friends. Special thanks to Dr. Kejia Yang for giving me career advice.

Special thanks to Mr. Brandon Stevenson-Matthews, who kept me company, comforted me when I was upset and made me a better person.

Most of all, I would like to give heartfelt thanks to my parents and my family. They are my biggest blessing and my deepest loves. Without their measureless love and continuous support, it would be impossible for me to finish my study.

This work was partially supported by National Science Foundation, National Institutes of Health, Cancer Prevention and Research Institute of Texas, American Heart Association and startup fund from University of Texas at Dallas.

March 2020

PHOTOINACTIVATION OF PROTEINS BY MOLECULAR HYPERTHERMIA

Peiyuan Kang, PhD
The University of Texas at Dallas, 2020

Supervising Professor: Zhenpeng Qin, PhD

Spatiotemporal control of protein structure and activity in biological systems has important and broad implications in biomedical sciences as evidenced by recent advances in optogenetic approaches. However, it is challenging to use light to manipulate protein activity in living systems without genetic modification. Plasmonic nanoparticles, due to their unique optical properties, provide exceptional nano-bio interface to control biological activities. Upon laser irradiation, plasmonic nanoparticles converse light energy into heat. This unique energy conversion pathway, known as plasmonic heating, can be precisely engineered on different scales by tuning the laser properties such as pulse duration and energy. Theoretically, it is possible to generate a nanoscale plasmonic heating by using the short laser pulse. In this work, we demonstrated that the nanoscale plasmonic heating can be used to precisely photoinactivate protein activities.

Firstly, we demonstrated that nanosecond pulsed laser heating of gold nanoparticles (AuNP) leads to an ultrahigh and ultrashort temperature increase, coined as "molecular hyperthermia" (MH). MH causes selective unfolding and inactivation of proteins adjacent to the AuNP. Protein inactivation is highly dependent on both laser pulse energy and AuNP size, and has a well-defined impact zone in the nanometer scale. We observed aggregation behavior of protein–AuNP conjugates at high laser intensities that originates from significant protein unfolding.

Secondly, we demonstrated MH can optically switch off protein activity in living cells with high spatiotemporal resolution. We showed that protease-activated receptor 2 (PAR2), a G-protein-coupled receptor and an important pathway that leads to pain sensitization, can be photoinactivated in situ by MH without compromising cell proliferation. PAR2 activity can be switched off in laser-targeted cells without affecting surrounding cells. Furthermore, we demonstrated the molecular specificity of MH by inactivating PAR2 while leaving other receptors intact. Next, we demonstrated that the photoinactivation of a tight junction protein in brain endothelial monolayers leads to a reversible blood–brain barrier opening in vitro. Lastly, the protein inactivation by MH is below the nanobubble generation threshold and thus is predominantly due to the nanoscale heating.

Thirdly, we used a numerical model to study important parameters and conditions for MH to efficiently inactivate proteins in the nanoscale. To quantify the protein inactivation process, impact zone is defined as the range where proteins will be inactivated by nanoparticle localized heating. We found that stretching the laser pulse duration reduces the MH impact zone with the same laser pulse energy. Temperature-dependent material density and specific heat have little effect on MH, while temperature-dependent thermal conductivity decreases the impact zone compared with constant properties. The thermal interface resistance doesn't have effect on MH water below 10^{-8} K m^2 W^{-1}. Lastly, study of nanoparticle geometry suggests that nanosphere has larger impact volume than nanorods with the same particle volume and energy input.

In summary, MH enables selective and remote manipulation of protein activity and cellular behavior. MH is a promising method with broad applicability to switch off protein activity without genetic modification and will find many applications in biomedical sciences.

TABLE OF CONTENTS

LIST OF FIGURES

LIST OF TABLES

LIST OF ABBREVIATIONS

AuNP	Gold nanoparticle
AuNR	Gold nanorod
AuNS	Gold nanosphere
A_0	Prefactor in Arrhenius model
C_{abs}	Absorption cross section area, m^2
Cht	α-chymotrypsin
C_p	Specific heat, J kg^{-1} K^{-1}
CTAB	Cetyl trimethylammonium bromide
DMM	Diffuse-mismatch model
DNP	Diameter of nanoparticle, $2R_{NP}$, m
D_{rod}	Diameter of rod
D_{water}	Diameter of water domain, $2r_{water}$, m
EMD	Equilibrium molecular dynamics
E_0	Activation energy in Arrhenius model
F	Laser fluence, J m^{-2}
G	Interfacial thermal conductance, W K^{-1} m^{-2}
k	Chemical reaction rate constant, s^{-1}
k_{Au}	Thermal conductivity of gold, W m^{-1} K^{-1}
k_{water}	Thermal conductivity of gold, W m^{-1} K^{-1}
LJ	Lennard-Jones
L_{rod}	Length of rod
LSPR	Localized surface plasmon resonance
MD	Molecular dynamics
MH	Molecular hyperthermia
OTS	Octadecyltrichlorosilane
PEG	Polyethylene glycol
Qv	Volumetric heating rate, W m^{-3}
R	The gas constant, 8.314 J K^{-1} mol^{-1}
RK	Kapitza resistance, K m^2 W^{-1}
SAM	Self-assembly monolayer
SAXS	Small angle x-ray scattering
s	Survival fraction of protein
T	Temperature, K
TA	Transient absorption measurement
TDTR	Time-domain thermoreflectance
t_0	Laser duration, s
u(t)	Unit step function

V_{NP}	Nanoparticle volume, m^3
α	Thermal diffusivity, $m^2\ s^{-1}$
μ	Center position of the pulse, s
2μ	Pulse duration, s

CHAPTER 1

REVIEW OF PLASMONIC HEATING AND OPTICAL MANIPULATION OF BIOLOGICAL ACTIVITIES BY NANOATRUCTURES

1.1 Plasmonic nanostructures and surface plasmon resonance

The material properties show unique differences from their bulk counterparts when the matter size is in the nanoscale. Although nanomaterials have been used in various applications for centuries (Figure 1.1A),[1] physics in the nanoscale remained veiled for a long time. Since Dr. Richard Feynman pointed the fact that "there is plenty of room at the bottom" in 1959, a field to study materials with an unparalleled precision is initiated.[2] After development for over 60 years, nanotechnology has made a significant impact on our society.

When metal size is in the nanoscale, they strongly interact with light and exhibit unique optical properties, known as plasmonic resonance. Upon the light irradiation, free electrons in a plasmonic nanostructure can be polarized by light, leading to an oscillating electromagnetic field inside immediately outside the structure surface, known as surface plasmon resonance (SPR).[3] Specifically, for metal nanoparticles smaller than the wavelength of incident light, the curved surface of the particle exerts restoring force to free electrons. This leads to a confined SPR excitation, known as localized surface plasmon resonance (LSPR, Figure 1.1B).[1] Without the variation of optical properties of environment, the LSPR can be tuned by two important factors, *i.e.* nanoparticle material and geometry. These factors can be carefully designed to obtain the best performance of LSPR in different applications (Figure 1.1C).[4]

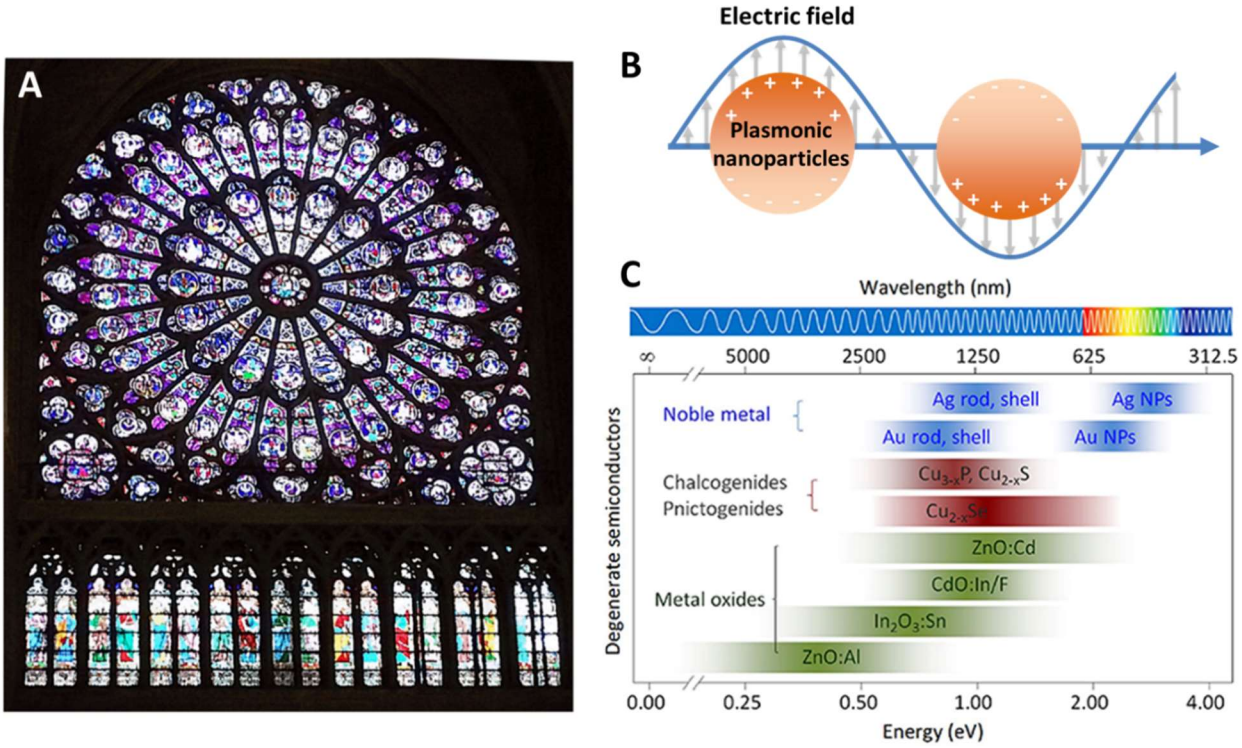

Figure 1.1. Plasmonic nanomaterials. (A) Window from the Notre-Dame Cathedral in Paris. The vivid color originates from the interaction between light and metal oxide particles suspended in the glass. (B) Schematic illustration of LSPR in the plasmonic nanoparticle. The conduction electrons oscillate with electromagnetic field. Redraw and modified from ref. 1. (C) Spectral regions of LSPR for different type of plasmonic nanomaterials. Reproduced with permission, Copyright 2019 American Chemical Society. Copyright 2018 Frontiers.

The selection of material for practical applications should be based on the balance between metal LSPR strength and chemical stability. Silver nanoparticle (AgNP) is one of the best candidates and exhibits strong LSPR strength due to its low optical loss in the visible and near-infrared (NIR) spectra ranges. However, silver nanoparticle is chemically instable and can be easily oxidized.[5] These drawbacks limit practical applications for silver nanoparticles. Aluminum (Al) is another emerging plasmonic material in the visible and ultraviolet (UV) region. Because its natural abundance and low-cost, it shows great potential in various applications. However, same

as silver, aluminum nanoparticle also suffers from quick oxidation which may cause deformation of nanostructures and change of optical properties.[6] Gold nanoparticle (AuNP), on the other hand, demonstrates an excellent chemical stability. Although less LSPR strength compared with AgNP, AuNP still shows an outstanding LSPR properties in UV and visible region (Figure 1.2).

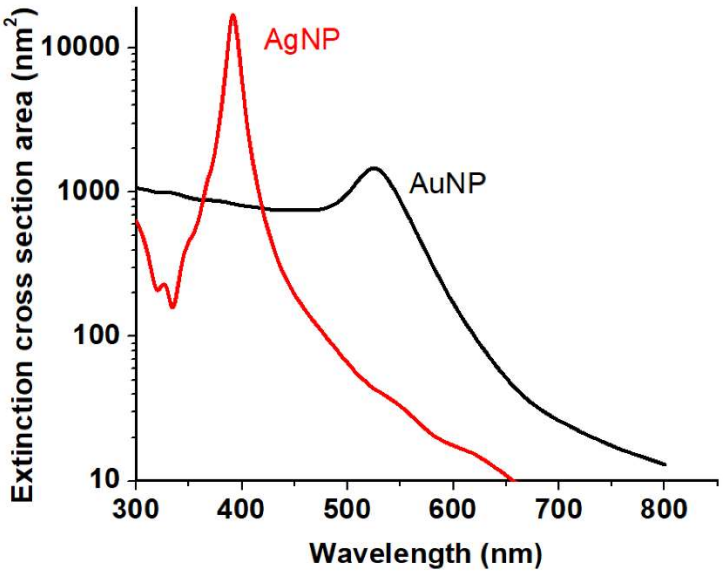

Figure 1.2. The extinction cross section area of AuNP and AgNP with the same size (30 nm in diameter).

The SPR can also be altered by tuning the plasmonic nanoparticle geometries, i.e. size and shape. Different geometries support different LSPR modes with varied optical properties. In general, the increase of nanoparticle size will lead the red shift of LSPR band and increase of LSPR band intensity.[7] For example, Gold nanosphere (AuNS) with diameter of 20 nm has LSPR band around 520 nm while the one for 100 nm AuNS is around 550 nm (Figure 1.3A). For a small particle, electromagnetic interaction between different parts of the particle is instantaneous, which is not valid for bigger particles. This is known as retardation. The red shift of LSPR band mostly originates from size effect of retardation.[7] Also, the obvious band broadening of AuNS larger than

100 nm originates from higher order electron oscillation.[8] Shape of the nanoparticle also has great effects on LSPR mode. For example, gold nanorod (AuNR) has two LSPR bands in visible and NIR region separately (Figure 1.3B). The visible band originates from the electron oscillation along the short dimension, known as transverse mode. And the band in NIR region is due to the electron oscillations along the long axis, referred to longitudinal mode. The LSPR of AuNRs can be tuned by varying the ratio between the radius and length, known as aspect ratio.

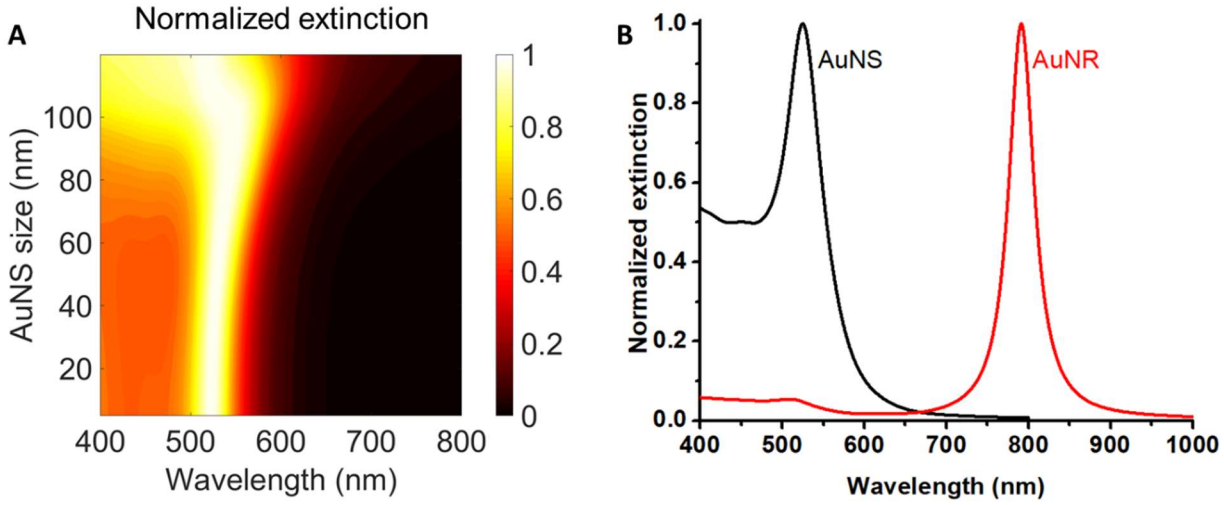

Figure 1.3. Effect of geometry on LSPR. (A) Normalized extinction for different size of gold nanospheres. (B) Normalized extinction of gold nanosphere (AuNS) and gold nanorod (AuNR) with the same particle volume.

1.2 Energy conversion induced by LSPR in different scales

Upon the light irradiation, LSPR greatly enhances the light-matter interaction and causes a series of energy conversion. The decay of LSPR enables the energy conversion from light to matters among different channels, namely radiative decay and non-radiative decay (Figure 1.4A).[9] Radiative decay of LSPR results in phonon emission. On the other hand, non-radiative decay of LSPR converts the light energy into thermal energy and transfers to surrounding matter. These

complicated energy conversion pathways bring several interesting phenomena. Depending on their impact region, they can be categorized into near-field and far-field effects (Figure 1.4B).

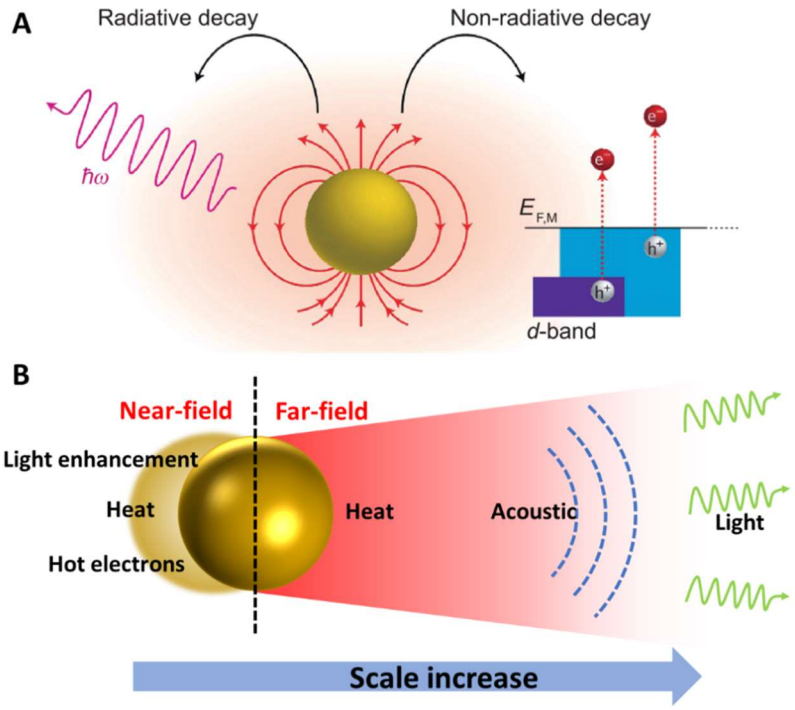

Figure 1.4. Energy conversion by the plasmonic nanoparticle. (A) LSPR decay can be radiative and non-radiative. Radiative decay emits phonons and non-radiative decay create electrons with high kinetic energy. Reproduced with permission, Copyright 2016 Nature Publishing Group. (B) Schematic illustration of near-field and far-field effects induced by LSPR decay.

First, the radiative decay of LSPR produces a significant enhancement of light intensity close to nanoparticles, known as near-field enhancement (Figure. 1.5A).[10] This confinement of light field offers a way to overcome the optical diffraction limit and enables a route to sub-wavelength optics (Figure 1.5B).[11, 12] When the near-field enhancement happens in a nanocavity, the confined light field generates pressure on molecules and leads to optical trapping (Figure 1.5C). Compared with conventional optical trapping techniques, near-field enhanced optical trapping can provide unparalleled spatial control due to the ultra-small volume of the enhanced light field.[13, 14]

Also, the enhanced local field can be also utilized to improve the behavior of fluorophore in terms of both lifetime and quantum yield.[15] Local field enhancement can be also used to generate coherent extreme-ultraviolet light. For instance, high-harmonic generation can be achieved by the local field enhancement induced by metallic nanostructures.[16]

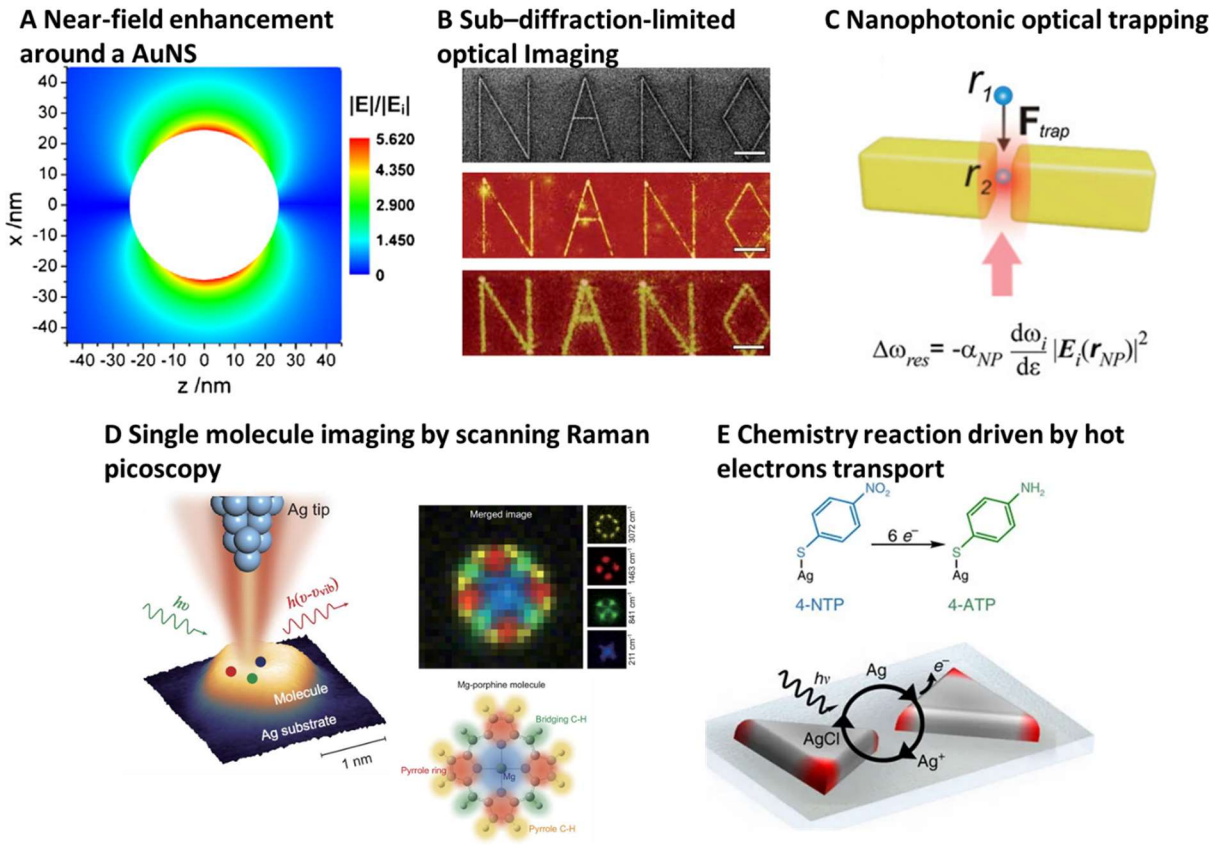

Figure 1.5. SPR and applications. (A) Electrical field enhancement around a gold nanosphere. Reproduced with permission, copyright 2012 Elsevier Science B.V. (B) Sub–diffraction-limited optical Imaging with a silver superlens. Reproduced with permission, copyright 2005 Science. (C) Nanoparticle optical trapping in plasmonic nanocavity. Reproduced with permission, copyright 2014 American Chemical Society. (D) Plasmonic nanocavity enhances Raman scattering and allows image single molecules at ångström level spatial resolution. Reproduced with permission, copyright 2019 China Science Publishing & Media Ltd. (Science Press). (E) Plasmonic hot electron transport drives nano-localized chemistry: reduction from 4-NTP to 4-ATP. Reproduced with permission, copyright 2017, Nature Publishing Group.

Second, in the far-field, emitted phonons that re-emitted can be detected as light scattering. Two types of scattering can occur, known as Rayleigh scattering and Raman scattering.[17] Rayleigh scattering emits photons with the same energy as the incident light. Raman scattering, on the other hand, emits photons with different energy from the incident light. The scattering, as far-field effects, reflects the local chemical environment adjacent nanomaterials and serves as sensitive detection methods for biomolecules. Especially, the LSPR significantly enhances the Raman scattering of molecules adjacent to a plasmonic nanoparticle surface and increases the detection sensitivity by several magnitudes. For example, Zhang et al. developed a method to analyses the Raman scattering for single molecules using Ag tip and substrate nanocavity, called scanning Raman picoscopy (SRP, Figure 1.5D).[18] They demonstrated that SPR can sensitively image the individual vibrational modes for single Mg-porphine molecule at the ångström level.

Third, the non-radiative decay of LSPR is responsible for generating hot electrons ejection with very high kinetic energies. Due to the extremely fast decay of LSPR, hot electrons related energy transfer is a typical near-field effect around plasmonic nanostructures.[19] Although the function and mechanism of hot electrons related energy transfer are still under hot debate,[20] this phenomenon is responsible for various plasmon enhanced chemical reaction applications such as photodecomposition of organic pollutants, solar water splitting, and synthesis of organic molecules. For example, Cortes et al. spatially map hot-electron-driven reduction chemistry (i.e. 4-NTP to 4-ATP) with 15 nm resolution as a function of time and electromagnetic field polarization for different plasmonic nanostructures (Figure 1.5E).[21]

1.3 Plasmonic heating

1.3.1 Fundamentals of plasmonic heating

Following the photo excitation of hot electrons, most of the energy carried by hot electrons will transfer to metal phonon which heats up the particle as well as the surrounding medium.20 This light-thermal energy conservation by plasmonic nanoparticle is known as plasmonic heating. The plasmonic heating is one of the most interesting phenomena from LSPR due to its flexibility of engineering in a wide scale. Here, we will focus on the fundamentals of plasmonic heating and demonstrate that the plasmonic heating can be tuned over a wide range.

The heat generation of a single plasmonic nanoparticle (Q_{NP}, W) can be simplified and described by the following equation:

$$Q_{NP} = C_{abs} \cdot I(t) \tag{1.1}$$

Where Cabs is absorption cross section (m^2) of nanoparticle and I is intensity profile of the incident light (W m^{-2}). These two factors are most important for tuning the plasmonic heating.

The absorption cross section (C_{abs}), as one of the optical properties, arises from the LSPR of plasmonic nanoparticle and is highly dependent on nanoparticle material and geometry, as stated previously. For spherical particles, Cabs can be precisely calculated using Mie theory which is an exact analytic solution to Maxwell equations for spheres with arbitrary size.[7] For a spheroidal particle much smaller than the excitation wavelength, Mie-Gans theory can give an analytic solution that approximately describe its spectra.[7] For particles with other shapes, the estimation of optical properties requires numerical methods, including boundary element method (BEM),[22] discrete-dipole approximation (DDA)[23] and finite difference in the time domain (FDTD).[24] In

terms of experimental measurement methods, spectrometry can be used to determine the extinction (sum of absorption and scattering) of nanoparticle colloidal solution. For small nanoparticles, the light scattering is small compared with absorption, thus extinction can be treated as absorption approximately. Furthermore, some scattering-based methods enable optical analysis at the single particle level, such as single nanoparticle spectroscopy[25] and dark-field microscope.[26]

The power profile of light source (I(t)) is another key factor that significantly affects the plasmonic heating. As an energy transport phenomenon, plasmonic heating area is highly related to energy transport time. Therefore, by varying the light duration and intensity, plasmonic heating can be precisely tuned in different scales. Owing to the development of laser technology, we now can study the plasmonic heating by optically exciting plasmonic nanoparticles with a controlled energy level and a wide range of duration, i.e. femtosecond (10-15 s) to continuous light irradiation. To demonstrate that plasmonic heating in different scales can be achieved by varying the light source, a precise description of energy conversion and transport in plasmonic heating is necessary.

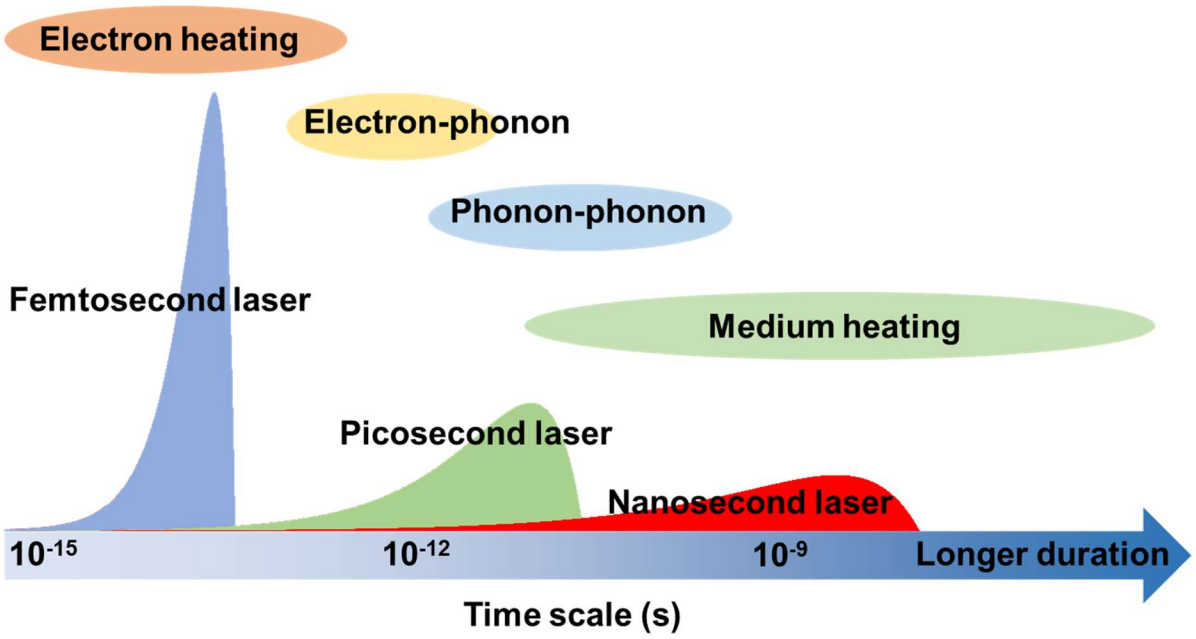

Figure 1.6. Schematic illustration of pulsed laser and transient events in plasmonic heating.

Upon light irradiation, free electrons obtain kinetic energy from light irradiation. Due to the electron-electron scattering, the thermal equilibrium will soon be reached within the electronic system after few hundreds of femtoseconds (Figure 1.6). If the light irradiation time is shorter than the electron-electron thermalization time, then it is possible to selectively excite electrons and observe the energy transport within the electronic system.[27] Following the thermalization of electrons, the electron-phonon energy transfer will take place within next few picoseconds (10^{-12} s). Subsequently, the phonon-phonon interaction results in heat transfer in nanoparticle and to surrounding medium within tens of picoseconds.[28] This energy transfer process can be described by two temperature model (TTM, Equation 1.2-1.3).

$$C_e \frac{\partial T_e}{\partial t} = \frac{1}{r^2}\frac{\partial}{\partial r}\left(k_e r^2 \frac{\partial T_e}{\partial r}\right) - G(T_e - T_l) + Q_v(x,t) \qquad (1.2)$$

$$C_l \frac{\partial T_l}{\partial t} = \frac{1}{r^2}\frac{\partial}{\partial r}\left(k_l r^2 \frac{\partial T_l}{\partial r}\right) + G(T_e - T_l) \quad (1.3)$$

Here, C_e is electron specific heat, C_l is phonon specific heat, k_e is electron thermal conductivity, k_l is phonon thermal conductivity, G is electron-phonon coupling factor, and Q_v is volumetric heat generation (Q_{NP}/V_{NP}, W m^{-3}). TTM is important to describe the heat transfer in short time scale. When the laser irradiation duration is longer than one nanosecond, the solution of TTM will be same as traditional heat transfer model, known as one temperature model (OTM).[29]

Importantly, the heat transfer in the surrounding medium (e.g. water) can be also engineered at different time scales by controlling the light energy input. This is because the heat diffusion is highly related to time. The thermal relaxation time (τ_{rel}, s) for a sphere is given by the following equation:

$$\tau_{rel} = \frac{d^2}{27\alpha} \quad (1.4)$$

Here, d is the diameter of heating volume (m), and α is thermal diffusivity (m^2 s^{-1}). τ_{rel} is defined as when the central temperature decreases to 50% of the initial value, assuming a Gaussian temperature distribution.[30] When applying laser pulse shorter than diffusion or relaxation time of the irradiated volume, the heat does not have enough time to dissipate away. For short or ultrashort laser, the laser power profile is intense over the laser duration, however the total energy of one pulse is limited and is not enough to heat a large scale (Figure 1.6). Therefore, under the irradiation of short laser pulse, heat will be confined around the plasmonic nanoparticle and causes a near-field plasmonic heating, known as thermal confinement. Depending on the laser pulse duration, the near-field plasmonic heating can be in the nanoscale. On the other hand, when laser duration is long, the heat generated in plasmonic nanoparticles will continue to dissipate away. During this

process, the heating from different particles starts overlapping, known as collective heating. When the total energy input in the system is higher than the total energy lost from the system, a global heating can be finally reached. This far-field heating effect is widely used in thermal therapy such as photothermal therapy for cancer.[31]

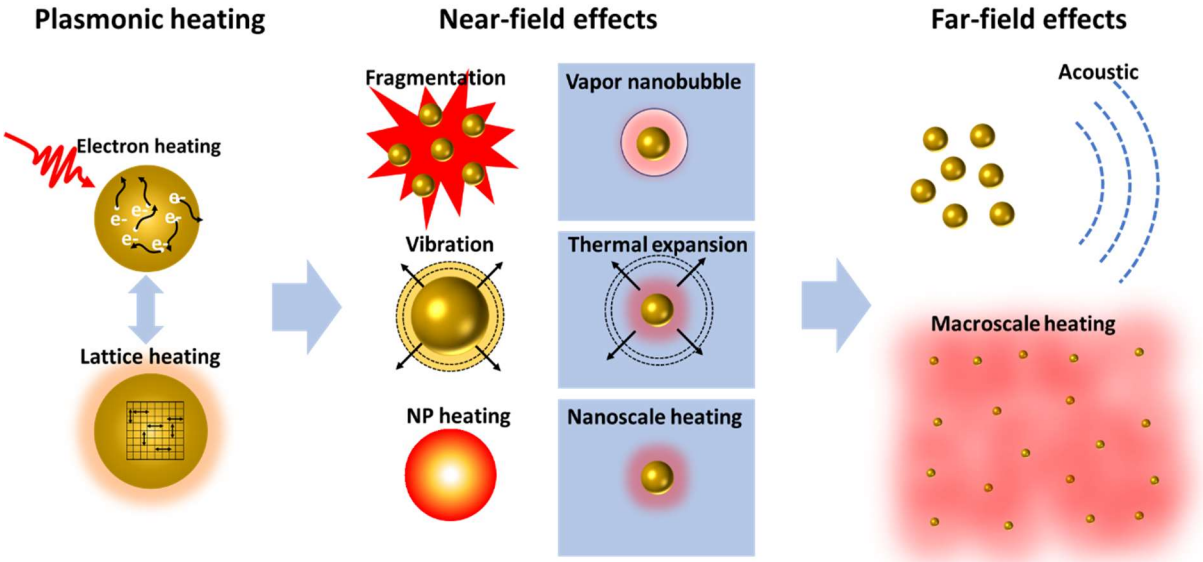

Figure 1.7. Phenomena induced by plasmonic heating in the near-field and the far-field.

Besides heating, there will be several interesting thermophysical responses of nanoparticles and surrounding medium, especially under irradiation of ultrashort (fs and ps) and short laser (ns) (Figure 1.7). The first one is thermal expansion of nanoparticles. The sudden temperature raise in lattices causes the particle expansion and vibration with a period of few picoseconds. The vibration modes (also known as breathing mode) is dependent on particle shape, and can be detected by transient optical measurement.[32] Second, when the laser energy is high enough, the temperature of the nanoparticle reaches phase transition point, which causes the particle melting. The phase transition combined with the mechanical stress in particle will decrease the particle stability and causes particle reshaping or fragmentation, known as laser instability.[33] Third, the sudden heating

in surrounding medium will also causes the thermal expansion of medium. This thermal expansion further causes the pressure change which will propagate away from the plasmonic nanoparticle in the speed of sound.[34] This phenomenon is called photoacoustic effect which has been widely used in biomedical imaging applications. Lastly, if the laser energy is high enough, the medium heating will cause vaporization and create a vapor nanobubble around the plasmonic nanoparticle. This is can be used as an effective method to pin holes on cell surface for molecular delivery into the cell without killing cells.[35]

To summarize, the plasmonic heating is one of the most interesting effect arise from LSPR and be precisely tuned and designed. This process has a great flexibility to be engineered in different temporal and spatial scales by varying laser properties, i.e. laser duration and energy. Through studying the plasmonic heating, we will have a better understanding of the thermophysical processes in the nanoscale. Also, it provides new opportunities for plasmonic nanoparticle applications.

1.3.2 Responses of biomolecules to plasmonic heating

The plasmonic heating is a unique tool that provides flexibility to engineer heat transfer on different scales. It is used in various bio-applications from the molecular level to tissue level. Here, we discuss the biological responses of several important biomolecules to plasmonic heating, including DNA, proteins and lipids.

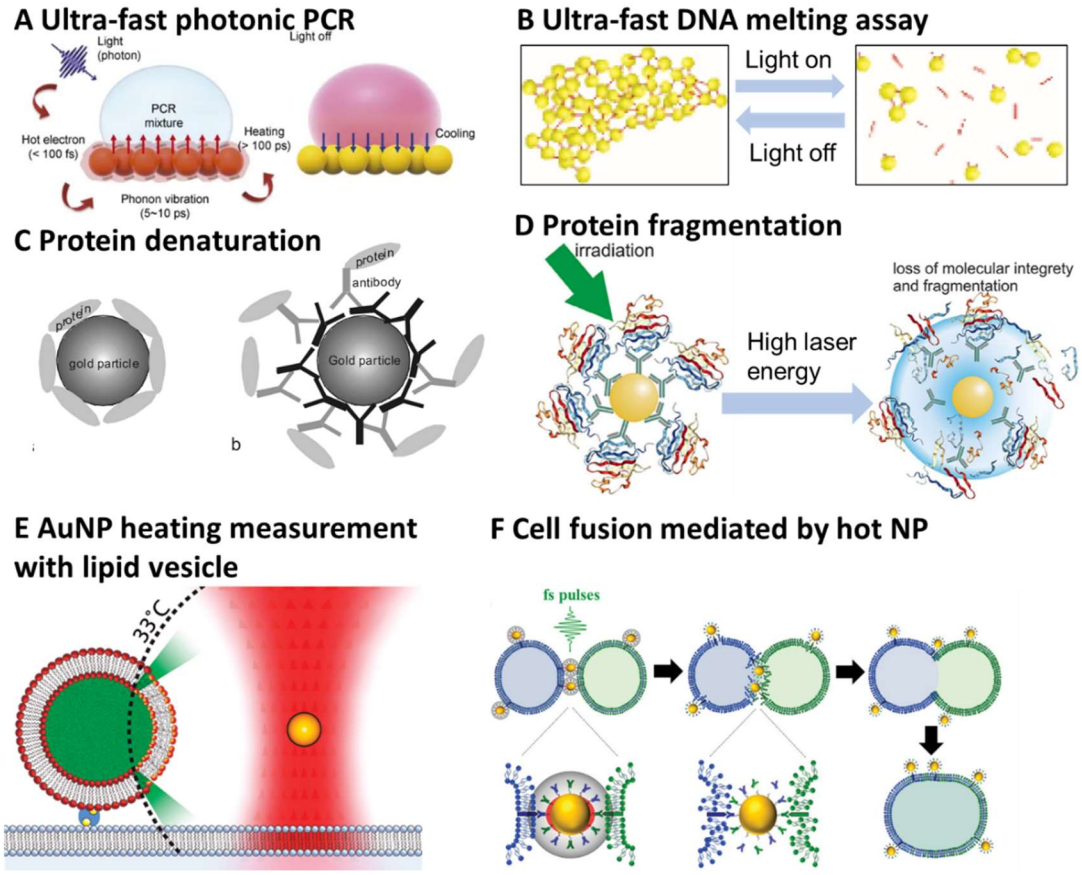

Figure 1.8. Plasmonic heating of biomolecules and applications. (A) Ultra-fast PCR achieved by plasmonic heating from AuNP film. Reproduced with permission, copyright 2015 Nature Publishing Group. (B) Ultra-fast DNA melting assay. Reproduced with permission, copyright 2008 American Chemical Society. (C) Protein denaturation by plasmonic heating of AuNP. Reproduced with permission, copyright 2003 SPIE. (D) Protein fragmentation induced by high energy laser heating of AuNP. Reproduced with permission, copyright 2019 John Wiley & Sons, Inc. (E) AuNP heating profile measurement by lipid vesicles. Reproduced with permission, copyright 2011 American Chemical Society. (F) Cell fusion mediated by AuNP plasmonic heating. Reproduced with permission, copyright 2013 John Wiley & Sons, Inc.

DNA is one of the most important molecules in organism. The double-strand structure of DNA is formed by hydrogen bonds between nucleobases, which is sensitive to temperature change. Increasing the temperature to 94-96 °C will break the hydrogen bonds and causes DNA melting or denaturation. This is an important step in polymerase chain reaction (PCR), known as

thermocycling.[36] The traditional thermocycling uses heating block which limits the thermocycling rate (heat/cooling rate). Plasmonic heating of nanoparticle, on the other hand, can achieve a much higher thermocycling rate due to their small size and high heat transfer efficiency. By taking advantage of plasmonic heating, a technique was developed called photonic PCR.[37] For example, 30 ultrafast thermal cycling from 55°C to 95°C can be achieved within 5 minutes with the help from gold nanoparticle film (Figure 1.8A).[38] The plasmonic heating can be further controlled precisely to achieve a reversible heating of DNA. For example, Stehr et al. demonstrated the DNA-AuNP aggregates can be reversely breakdown by a 300 ns laser pulse irradiation (Figure 1.8B).[39] They further demonstrated that double-stranded DNA melt on the microsecond time scale and the AuNP aggregates lose their structure integrity on the millisecond time scale. This melting assay can be used as a rapid and high-through put DNA analysis technique. The plasmonic heating can be also used to release DNA molecules from the particle surface. For instance, Huo et al. designed an AuNP-DNA complex which can be disassembled by plasmonic heating up on NIR light irradiation. With a well-designed gene silencing sequence, this method is demonstrated to effective silence the targeted gene expression both in vitro and in vivo.[40]

Protein is another important molecular machinery in biological systems. Due to their complicated structures, precise control of protein activity is a sophisticated task. So far, most methods are based on biological and biochemical techniques such as gene-editing and gene-silencing which have debatable translational medical value. On the other hand, due to the precision and flexibility of plasmonic heating, it is possible to use plasmonic nanostructures to manipulate function of proteins. Here we give a brief introduction on efforts had been done so far. Huttmann et al. demonstrated the enzyme can be inactivated by AuNP after nanosecond and picosecond laser

plasmonic heating. They introduced the possibility of using AuNP to inactivate protein precisely (Figure 1.8C). However, in their experiments, it is required to either use laser pulse with high energy (>1000 mJ cm^{-2}) or a large number laser pulses (>100 pulses).[41] Similarly, Pitsillides et al. demonstrated that the anti-fluorescein antibody can be selectively inactivated by plasmonic heating.[42] Instead using AuNP, Steel et al. utilized plasmonic heating of a gold nanofilm to inactivate the proteins absorbed on its surface.[43] In this work, the temperature can be monitored by transient optical method and be used to calculate kinetics of the protein inactivation. They showed the protein inactivation under nanosecond laser pulse follows the traditional Arrhenius law. As an alternative to conventional temperature-jump method, this work offers opportunities to study protein denaturation in the nanosecond range. However, the data size of this study is small, and it is hard to apply this method to control protein function in biological systems. Besides protein inactivation, protein degradation by plasmonic heating was also reported. For instance, Takeda et al. recognized the protein degradation after numerous laser pulses, which they firstly interpreted as a nanoplasmonic effect and later interpreted as plasmonic heating effect.[44, 45] Similarly, Rahmanzadeh et al. also observed fragmentation of the Ki-67 protein by plasmonic heating with high energy laser irradiation (Figure 1.8D).[46] The mechanism of this phenomenon is still unknown and further studies are necessary.[45]

Lipid is the basic component of cell membranes which provides an enclosed environment for cells. At certain temperatures, lipid structures will go through a transition from ordered phase (gel phase) to disordered phase (liquid crystalline phase), known as the transition temperature. Plasmonic heating of nanoparticles, as a well-controlled nanoscopic source of heat, provides a way to study the lipid thermal response in the nanoscale. For instance, Urban et al. used single AuNP

to create a nanoscopic heating rapidly and induced a nanoscale reversible gel-fluid phase transitions in phospholipid membranes.[47] Furthermore, combining with optical tweezer technique, Kyrsting et al. utilized plasmonic heating of AuNP to transiently control the lipid vesicle permeability. Knowing the transition temperature, the footprint of the lipid phase transition can be used to measure the plasmonic heating in the nanoscale (Figure 1.8E).[48] By taking advantage of the phase transition of lipid bilayers, plasmonic heating of AuNP can merge the nanovesicles and even cells. For instance, Yeheskely-Hayon et al. inserted AuNPs in between different cells and induced cell fusion using femtosecond laser pulses. The AuNPs are modified with two different antibodies which allow the AuNP to specifically bind to two types of cell simultaneously. This is a potential method to create a specific cell-cell interaction (Figure 1.8F).[49]

In summary, plasmonic heating provided a unique nano-bio interface and can be used to precisely manipulate the bioactivity of molecules.

1.4 Optical manipulation of biological activity enabled by nanostructures

There has been significantly interested to precisely manipulate biological activity. And using light as the stimuli provides an unparalleled spatiotemporal control for biological activity manipulation. Here, I introduce examples of optical manipulation methods, especially ones enabled by nanostructures. Depending on the triggering mechanism, Table 1.1 lists the examples discussed here.

Table 1.1. Examples of studies on optical manipulation of biological activity enabled by nanostructures.

Triggering mechanism	Photosensitive nanostructures	Application	References
Light	Upconversion nanoparticle (UCNP)	Deep brain stimulation by optogenetics	50
Reactive oxygen species	Titanium Dioxide (TiO_2)-gold nanocluster (AuNC)-graphene	melanoma skin cancer treatment by photodynamic therapy (PDT)	51
	Fluorescent proteins	Selective protein inactivation by chromophore assisted light inactivation (CALI)	52
Molecular structure control	Synthetic photoswitches peptides	G protein coupled receptor (GPCR) activity control	53
Electrical field	Quantum dot	Neuron firing	54
Mechanical stress	Gold coated Mechanosensitive nanovesicles	Molecule release in deep brain	55
	Single wall carbon nanotube (SWNT) & AuNP	Stimulated cell differentiation	56
Photothermal	Solica coated gold nanoshell (Au@SiO_2)	Cancer treatment by photothermal therapy (PTT)	57
	Coppor sulfide (CuS) nanoparticle	Activation of TRPV1 and attenuation of atherosclerosis	58
	AuNR	Transient receptor potential vanilloid 1 (TRPV1) activation induced neuron firing	59
	AuNR and AuNS	Membrane potential changing induced neuron firing	60

1.4.1 Optogenetics improved by UCNP

In 2005, optogenetics was introduced and allows scientists to control neuron cells behavior with light simulation.[61] The invention of this technique is an obvious milestone in neurosciences, since it helps us understand how specific cell type contributes to complex neural circuits and brain functions. Optogenetics utilizes genetics to express photosensitive proteins and enables light

manipulation of targeted cells. Most applications use opsin, a group of photosensitive proteins can be found in photoreceptor cells of the retina. Most opsins only response to visible light which has a limited tissue penetration. To achieve a deep brain stimulation, an efficient light delivery method is required. Chen et al. utilizing upconversion nanoparticles (UCNP) enables optogenetics with NIR light which has an enhanced tissue penetration (Figure 1.9A).[50] They demonstrated that the UCNPs can serve as optogenetic actuators of transcranial NIR light to stimulate deep brain neurons.

1.4.2 Reactive oxygen species

Light can be used to trigger the chemical reactions enabled by nanomaterials. Photodynamic therapy (PDT) utilizes photosensitizers to generate reactive oxygen species (ROS) under light irradiation, and oxidize cellular macromolecules for cell ablation.[62] This method is a safe, potent and cost-effective way to treat cancer. Photosensitive nanoparticle is an emerging agent for PDT applications. Compared with traditional photosensitizers (based on small molecules such as nonporphyrinoid compouds), nanoparticle has several advantages including easy surface modification, long circulation time, and cancer site specificity.[63] Despite there are several of polymer nanocomplex for PDT purposes, numerous of nanomaterials have been focused due to the ability to generate ROS efficiently accompanying with unique optical and chemical properties, such as fullerenes and titanium dioxide nanoparticles. For instance, Cheng et al. designed a sophisticated nanocomposite with titanium dioxide (TiO_2), gold nanocluster (AuNC) and graphene to enhance the light utilization in PDT for melanoma skin cancer treatment (Figure 1.9B). With

this nanocomposite, they demonstrated the nanocomposite has an improved ROS generation efficiency for simulated sunlight and enhances cancer inhibition.[51]

With the similar mechanism as PDT, chromophore-assisted light inactivation (CALI) uses photosensitizer to generate ROS and specifically inactivate protein of interest. Because the lifetime for ROS is a few microseconds, which only allows ROS to diffuse in the nanoscale. CALI can inactivate protein with good specificity. Besides using small molecules as photosensitizers, CALI also genetically encodes the fluorescent protein into proteins of interest, which provides great flexibility and specificity to control protein inactivation. For instance, engineered green fluorescent protein (EGFP) was demonstrated to inactivate protein of interest without photodamaging cells.[52] However, CALI's efficiency is dependent on the expression level of the protein photosensitizer and the cellular microenvironment such as oxygen concentration and endogenous reducing agent (e.g. glutathione).[64]

1.4.3 Molecular structure change

Synthetic photoswithes are emerging tools to control protein activity by light. It is based on light induced structural change of photoresponsive small molecules (mostly based on azobenzene) to transiently control protein activity. For example, Gomez-Santacana et al demonstrated the G-protein coupled receptor (GPCR) activity can be controlled by light through a photoswitch modified peptide (Figure 1.9C).[53] The peptide can change from antagonist to angoist with light irradiation. Specific wavelength is required to activate the photoswitch. However, currently there are limited number of photoswitches and thus narrow options of light source (i.e. wavelength).

1.4.4 Electrical field

The light energy can also be used to create an electrical field and generate effect on ion channels or cell membrane potentials. Upon the light irradiation, quantum dot (QD) experiences electron-hole separation or electric dipole moment. The potential created by QD decays fast from the surface of the particle, and can only effectively affect cell membrane in the nanoscale. Lugo et al. utilized QD to trigger the potential and ionic current in cells by light irradiation (Figure 1.9D).[54]

1.4.5 Mechanical stress

When plasmonic nanoparticle is irradiated by fast laser pulse, the surrounding medium experiences heating and a pressure transient change, known as photoacoustics or photomechanics. This mechanical force can be also used to control molecules and modulate biological activity. Xiong et al. demonstrated that mechanoresponsive nanovesicles with gold-coating has an enhanced sensitivity to light, and can release molecules with much lower power than regular gold coated nanovesicles (Figure 1.9E).[55] They further demonstrated the photo-release can be achieved down to a depth of 4 mm in mouse brain which covers most depth of the mouse brain. Also, Greens et al. shows that the photoacoustic signal generated by single-walled carbon nanotubes (SWNT) and AuNPs can be an effective stimulation on marrow's differentiation toward osteoblasts.[56]

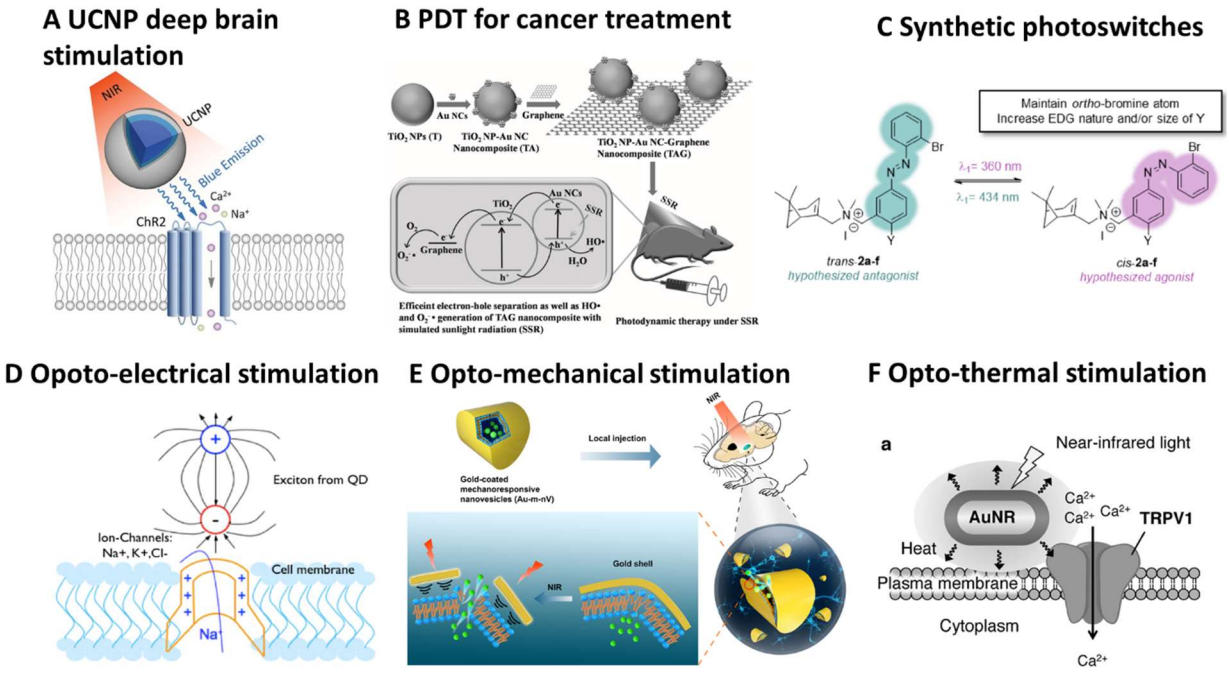

Figure 1.9. Optical manipulation of biological activity enabled by nanostructures. (A) Deep brain stimulation by near-infrared light (NIR) enabled by upconversion nanoparticle (UCNP). Reproduced with permission, copyright 2018 Science. (B) Photodynamic therapy (PDT) for melanoma skin cancer by TiO_2-AuNC-graphene heterogeneous nanocomposites. Reproduced with permission, copyright 2014 John Wiley & Sons, Inc. (C) Synthetic photoswitches. Reproduced with permission, copyright 2018 John Wiley & Sons, Inc. (D) Cellular activity mediated by quantum dot (QD). Reproduced with permission, copyright 2012 Optical Society of America. (E) NIR triggered release by ultra-photosensitive nanovesicles Reproduced with permission, copyright 2020 John Wiley & Sons, Inc. (F) Plasmonic heating triggers neuron firing by activating TRPV1 receptors. Reproduced with permission, copyright 2015 John Wiley & Sons, Inc.

1.4.6 Photothermal effect

Some molecules or nanostructures can absorb the light energy and convert into thermal energy, known as photothermal effect. Specifically, the photothermal effect by plasmonic nanostructures is called plasmonic heating. Some dye molecules and carbon-based nanostructures also have strong heat generation under light irradiation with certain wavelength.[65, 66] Photothermal effect is one of the most widely used tool in biomedical sciences. With a long energy input

duration, the photothermal can generate a global tissue heating for tumor ablation, known as photothermal therapy (PTT). Hyperthermia, based on a similar idea, creates temperature raise for several degrees Celsius in tumor with a long-term (minutes) energy input, while not necessarily by light irradiation. Gold nanomaterials are widely used in these applications due to their unique optical properties. O'Neal et al. demonstrated tumor resorption can be achieved by photothermal effect of gold silica nanoshell under NIR light irradiation for 5 mins.[57] It is worth noting that the PTT and hyperthermia for cancer treatment involve not only the thermal damage of tumor cells, but also immune response to the cancer cell damages.[58]

Instead of killing cancer cells, photothermal can be also used to control cellular behaviors. Gao et al. demonstrated the photothermal heating of copper sulfide nanoparticles can activate the transient receptor potential cation channel subfamily V member 1 (TRPV1) channels in vascular smooth muscle cells and leads to autophagy and impedes foam cell formation. This could be a therapeutic tool to locally and temporally attenuate atherosclerosis.67 Importantly, TRPV1, as a thermosensitive cation channel, shows great potential to stimulate the cells combining with photothermal effect. For instance, Nakatsuji et al. utilized highly localized photothermal heating from AuNR to activate TRPV1 and stimulate cells (Figure 1.9E). This technique can safely modulate cation influx without damaging cell membrane.[59] Under the external stress, cell may express heat-shock protein (HSP) as a protective mechanism. Robert et al uses AuNR to generate a mild heating on substrate and induce HSP expression in cells.68 This work provided a way to control protein expression on the single cell level. The heating can also induce membrane capacity change and causes neuron cell polarization. Carvalho-de-Souza et al. showed the binding of AuNR

to neurons enables the photosensitivity of neurons without genetic modification. They demonstrated that the neuron can be fired by light irradiation with a rate of 40 Hz.[60]

To summarize, nanostructures response to light provide opportunities to control biological activities with great precision. These techniques not only help us better understand the fundamental knowledge of biology activities in different systems, but also offer us various therapeutic tools for disease treatment.

1.5 Conclusion and outlook

Light responsive nanomaterials have attracted intense research in recent years due to their potential of controlling biological systems with great spatial and temporal control. As an outstanding light responsive nanomaterial, plasmonic nanoparticle such as AuNP, provides us great interface to control biological process in different scales. In this chapter, we have discussed many of the important optical and thermophysical processes in different scales when plasmonic nanoparticle interacts with light. We firstly introduced the fundamentals of LSPR and some important factors of plasmonic nanoparticles in LSPR generation. Secondly, we introduced important energy conversion phenomena induced by LSPR. Specifically, we have introduced near-field and far-field effects arise from LSPR by showing some example applications of the near-field enhancement, LSPR mediated scattering and hot electron related chemical reactions. Then, we focused on plasmonic heating and demonstrated plasmonic heating can be engineered in both the near-field and the far-field by adjusting the incident light duration and energy. Specifically, we introduced the thermophysical responses of biomolecules (i.e. DNA, proteins and lipid) to plasmonic heating by showing some bio-applications of plasmonic nanomaterials. Lastly, we

reviewed examples on optical manipulation of biosystem enabled by nanostructures. In summary, based on the principles of plasmonic heating reviewed here, it is increasingly possible to control biology at the molecular, cellular and tissue level by simply turning on a laser "switch".

In this thesis, we present a method which uses the nanoscale plasmonic heating of AuNPs to precisely inactivate proteins, called molecular hyperthermia (MH).

In chapter 2, I will introduce the concept of MH and demonstrate the feasibility of protein inactivation by MH. We will show that nanosecond pulsed laser heating of AuNP leads to an ultrahigh and ultrashort temperature increase, which causes selective unfolding and inactivation of proteins adjacent to the AuNP in solution.

In chapter 3, I will further prove that MH can be used in living system by showing the protein inactivation by MH in live cells. Two examples of proteins inactivation by MH will be shown to demonstrate MH is a promising method with broad applicability to switch off protein activity in live cells without genetic modification.

In chapter 4, I will numerically investigate protein inactivation by MH. The numerical model enables us to quantitatively investigate the important parameters for MH and provides a better understanding of the protein inactivation response to the near-field plasmonic heating.

In chapter 5, I will draw conclusions and point out some important questions for the future development of MH.

CHAPTER 2

MOLECULAR HYPERTHERMIA: SPATIOTEMPORAL PROTEIN UNFOLDING AND INACTIVATION BY NANOSECOND PLASMONIC HEATING

This chapter has been published as a paper in Small: Kang, P.; Chen, Z.; Nielsen, S. O.; Hoyt, K.; D'Arcy, S.; Gassensmith, J. J.; Qin, Z., Molecular hyperthermia: Spatiotemporal protein unfolding and inactivation by nanosecond plasmonic heating. Small 2017, 13, 1700841-1700847.

2.1 Introduction

Proteins are the functional machinery of biological systems and the development of techniques to change a protein's conformation and control its function with both high spatial and temporal resolutions is a crucial pursuit in the development of next-generation medicine. This capability is being rigorously pursued as it offers significant and broad implications for uncovering a protein's folding and unfolding mechanisms, elucidating a protein's biological function *in situ,*[69-71] non-invasively manipulating biological activity,[61] and developing novel therapeutics for disease treatment. This is partially evidenced by the development and application of optogenetic approaches that have utilized light-responsive activity-modulating proteins in the last decade.[61, 72] While the genetic modification represents a challenge for clinical translations, such novel approaches to spatiotemporally modify protein conformation and function promise to lead to paradigm shifting advances.

Nanoparticles offer a direct interface with proteins and there have been significant advances in using nanoparticles for the long-term labeling and tracking of proteins in living cells owing to their excellent photostability.[73-75] While nanoparticle labeling has led to new understanding of protein localization and dynamics in live cells, the ability to further manipulate protein structure and activity with a high spatiotemporal resolution represent a significant advancement with a wide range of new possibilities and applications. Continuous wave laser heating of plasmonic nanoparticles is known to induce a macroscopic temperature change and have been widely studied for photothermal hyperthermia therapy.[31] Recently, Thompson et al. demonstrated that gold nanorod heating under continuous wave laser leads to enzyme inactivation [76] and attributed this effect to the nanoscale heating effect in addition to the macroscopic heating.

The laser heating increases the medium temperature by 10 to 20°C, however, such a temperature change is insufficient to inactivate enzymes by holding the enzymes at equivalent temperatures without nanoparticles. While promising, the large temperature change may lead to changes in other cellular proteins at hyperthermic temperatures.

Pulsed laser heating of plasmonic gold nanoparticle (AuNP) is known to create a highly localized heating.[30, 41, 77, 78] Here we utilize AuNP and pulsed laser heating to generate a highly localized ultrahigh temperatures in a few nanoseconds to cause ultrafast protein unfolding and inactivation. To test the idea, we conjugated an enzyme protein, α-chymotrypsin, to AuNP through either the covalent bound or electrostatic absorption. By measuring and comparing the enzyme activity before and after the nanosecond laser irradiation, we determined the fraction of protein inactivated by the nanosecond plasmonic heating. The heating is localized within a few nanometers around the nanoparticle without changing the bulk medium temperature. We then systemically investigated the effects of AuNP size, distance between AuNP and protein, and laser pulse number on the protein inactivation, and found a well-defined protein inactivation impact zone around the AuNP in the nanometer scale as a function of laser pulse energy and AuNP size. We further examined the fate of AuNP and AuNP-protein conjugate after laser treatment, and uncovered the AuNP aggregation due to protein unfolding at high laser intensities. Both the high spatial (nanometers) and temporal (nanoseconds) capabilities offered by this new technique will find broad applications in the biophysical study of protein folding/unfolding, inactivation of protein activity *in situ* to elucidate protein function, remote manipulation of biological activity, and development of novel methods to treat diseases.

2.2 Experimental section

2.2.1 Gold nanoparticle (AuNP) synthesis

All glassware and magnetic stir bars were cleaned with aqua regia for 30 min and rinsed with Millipore water.15 nm colloidal AuNP was synthesized by the Frens' method as previously reported.[79, 80] Briefly, 1 mL $HAuCl_4$ (25 mM) was add to 98 mL water in a 250 mL Erlenmeyer flask and brought to a boil. Under rigorous stirring, 1 mL sodium citrate (112.2 mM) was rapidly added to allow the reaction for 10 min. The flask was then removed from the hot plate after the reaction was completed.

30 nm AuNP was synthesized using 15 nm AuNP as the seed.[11] Briefly, 15 nm AuNP concentration was adjusted to 2.23 nM. 880 µL of $HAuCl_4$ (25 mM), sodium citrate (15 mM) and 12.5 mL 15 nm AuNP (2.23 nM) were added into 86 mL water. Under rigorous mixing, 880 µL hydroquinone (25 mM) was added into the vortex swiftly to observe the immediate color change. The solution was stirred for half an hour under high speed stirring, and then changed to low speed stirring overnight.

5nm colloidal gold nanoparticle was synthesized following a previously reported procedure.[81, 82] Briefly, 1mL of $HAuCL_4$ (25mM) was added to 80mL water in 250mL Erlenmeyer flask, and the solution was heated to 60°C in a water bath. The reduction solution was prepared by mixing 16mL water, 4mL Trisodium citrate (1% w/v), 1mL tannic acid (1% w/v) and 1mL Potassium carbonate (3.26mg/mL). The reduction solution was kept in hot water bath until the temperature reaches 60°C. Under vigorous stirring, the reduction solution was added swiftly into

the flask at one time and the reaction was kept at 60 ºC for half hour, and then at 90 ºC for 10 mins. The flask was then removed from the water bath and allowed to cool to the room temperature.

2.2.2 Egg white experiment

15 nm AuNP (200 uL, 6 nM) was added to 200 uL water and egg white respectively. Samples were mixed by pippetting gently and allowed to incubate for 30 mins. Laser experiment was conducted to irradiating samples by nano second laser pulse with energy density in 114 ± 4 mJ/cm^2. Samples in the bulk heating group were heated in a water bath at 100 °C for 10 mins. All samples were placed on a glass slide for photography, with a visual guide underneath (Figure 2.2A).

2.2.3 Covalent conjugation of protein onto AuNP

AuNP was first coated with heterofunctional polyethylene glycol (PEG) molecules (1kDa, Nanocs, thiol and carboxyl functionalization on the two ends) by incubation for 2 hours at room temperature with slow stirring. The ratio of PEG molecule to AuNP is dependent on both PEG molecular weight and AuNP size, as previously reported.[83] In our experiment, the ratio of PEG to AuNP was 1000, 5500, and 100,000 for 5 nm, 15 nm and 30 nm AuNPs, respectively. The excess PEG was removed by centrifugation (3 times, 25 min each). Centrifugation speed was dependent on AuNP size (2000 g for 30 nm, 10000 g for 15 nm, and 100,000 g for 5 nm). All particles were stored at 4 °C. To test whether the PEG is fully coated onto AuNP, standard PBS (1X) solution was added into PEG-coated AuNP. Any color change indicates unsuccessful PEG coating. PEG

length is estimated by calculations reported before; the R_{min} of folded PEG on AuNP is calculated as its Flory radius (R_F).[84]

$$R_F = aN^{3/5} \tag{2.1}$$

Here, we take a=3.5 Å which is the length of one repeating unit of PEG. N=1000/44=22.73. The full expansion of PEG is calculated simply with $L_{max} = aN = 7.95\ nm$.

α-chymotrypsin (Cht, from bovine pancreas, type II) was purchased from Sigma-Aldrich (C4129). 2 mL Cht (2 mg/mL) was dialyzed twice, with a duration of 0.5 hour each time and in at least 1 L of Cht stock buffer which contains HCl (1 mM) and $CaCl_2$ (2 mM). After dialysis, Cht solution was stored at -20°C. The concentration of Cht can be determined by absorbance at 280 nm with extinction coefficient E_{280}= 50000 M^{-1} cm^{-1}.

The size of Cht is estimated by assuming the protein shape is a sphere. The protein minimal radius R_{min} is calculated from the equation below,

$$R_{min} = 0.066M^{1/3} \tag{2.2}$$

M is the molecular weight in Dalton. R_{min} is in nanometers.

To conjugate the protein onto AuNP, AuNP was re-suspended in MES buffer (100 mM pH=5.5). 1-Ethyl-3-(3-dimethylaminopropyl) carbodiimide (EDC) solution (2 mM) and sulfo-N-hydroxysuccinimide (sulfo-NHS) solution (4 mM) were then prepared. 100 μL of EDC and 400 μL of sulfo-NHS were mixed and then added into 1 mL gold nanoparticle, immediately followed by rigorous stirring. The mixture was then incubated for 15 min at room temperature and AuNP was then cleaned by centrifugation to remove unreacted EDC and sulfo-NHS. After washing, AuNP was then re-suspended in HEPES buffer (10 mM pH=8.0) and mixed with Cht, immediately

followed by rigorous stirring. After reacting for 2 hours, the excess protein was removed three times by centrifugation. The protein-conjugated AuNP was stored at 4 °C and used within 2 days.

2.2.4 Electrostatic adsorption of protein to gold nanoparticle

The formation of a protein corona on AuNP is highly dependent on pH.[83] From previous work,[41, 45, 85] the optimum pH for protein passive adsorption is around the isoelectric point, i.e. pH = 8.9 for Cht. We dissolve the protein into Tris-HCl buffer with pH=8.8; under vigorous stirring, AuNP was injected into the protein solution. The ratio of Cht to AuNP is dependent on the gold nanoparticle size and kept the same as for covalent conjugation. The excess protein was removed by centrifugation.

2.2.5 α-chymotrypsin activity assay

We used a substrate cleavage assay to measure α-Cht activity.[86] Briefly, the substrate solution was made by adding Suc-Ala-Ala-Pro-Phe-NA (Sigma-Aldrich S7388) into the buffer solution which contains 0.1 M tris and 0.01 M $CaCl_2$ and the pH was adjusted to 8.0 by adding HCl. The substrate concentration was kept at 1 mM. To test the sample enzymatic activity, 12 μL sample and 60 μL substrate solutions were mixed together. The absorbance was recorded at 410 nm for 2 minutes using a BioTek Synergy 2 Multi-Mode plate reader. The slope of the absorbance change was used to calculate the enzyme activity.

2.2.6 Alkaline phosphatase (ALP) activity assay

We used a substrate cleavage assay to measure ALP activity.[87] Briefly, the substrate solution was made by adding 4-Nitrophenyl phosphate disodium salt hexahydrate (pNPP, Sigma-

Aldrich p4744) into buffer solution which contains 0.1 M Diethanolamine and 0.5 mM $MgCl_2$ with the pH adjusted to 9.8 at 37 °C by adding HCl. Similar to the Cht activity, the substrate concentration is much higher than the enzyme concentration, specifically at 10 mM. To test the sample enzyme activity, 12 µL sample and 60 µL substrate solutions were mixed together. The absorbance was recorded at 405 nm for 2 minutes using a plate reader at 37 °C. The slope of the absorbance change was used to calculate the enzyme activity.

2.2.7 Nanoparticle characterization

AuNP samples were measured by dynamic light scattering (DLS) using a Malvern Nano ZS (Malvern instruments, UK). Each sample was set to equilibrate to 25 °C for 120 seconds. UV-vis spectra of AuNPs were obtained by using a Beckman DU800. AuNP concentration was determined by the formula below:

$$C = \frac{A}{\varepsilon b} \tag{2.3}$$

In which C is the AuNP concentration (mol/L), A is the absorbance, b is the path length which is 1cm for our case, and ε is determined by the following formula,[82]

$$\varepsilon = 12402.24\left(\frac{3}{2}\pi D^3\right)^{1.0643} \tag{2.4}$$

Transmission electron microscopy (TEM) data was measured using a JEM 2100F analytical TEM. The nanoparticle sample was placed as a droplet on the copper mesh (PELCO 160, PELLA Inc.) and air-dried for 2 hours before imaging.

Native agarose gel electrophoresis was performed to further check protein conjugation onto AuNP and changes after laser treatment. Samples were loaded in 1% agarose (Fisher Scientific

Inc.) and run in 1X TBE buffer (Tris-Brorate-EDTA buffer, Fisher Scientific Inc.) at 60 V for 1.5 hours, followed by coomassie blue staining to visualize proteins.[88]

2.2.8 Nanosecond laser experiment

The sample was irradiated by a nanosecond laser pulse generated from a Nd:YAG laser (Quantel Q-smart). The laser wavelength is fixed at 532 nm. The laser pulse has a Gaussian temporal profile and the duration is 6 ns. The 40 μL sample was diluted to OD=0.1 and held in a micro UV cuvette. The laser beam was guided to pass into the cuvette. The laser pulse energy was monitored by a beam splitter with 88% of the laser energy directed to the sample and 11% to the laser power meter (FieldMaxII, Coherent USA). After the laser treatment, 12 μL of sample was taken to measure the protein activity.

2.2.9 Photoacoustic experiment

Photoacoustic experimental data was collected using a 5 MHz single element ultrasound transducer (V308-SU Olympus) in series with a 25 Watt power amplifier (325LA E&I) and digital oscilloscope for signal measurement. Samples are prepared in DI water and placed in a dialysis bag to seal and hold the 30 nm AuNPs. The laser is exposed perpendicular to the sample bag to allow collection of the photoacoustic signal.

2.2.10 Circular Dichroism (CD) spectrometer characterization of protein unfolding

Protein secondary structure and its thermal stability is analyzed by far-UV CD spectroscopy (Aviv CD spectrometer model 430).[89, 90] α-Cht samples are prepared at

approximately 1mg/mL. The mean residue weight ellipticity θ_{MRV} is calculated using the following equation:

$$\theta_{MRV} = \frac{\theta}{cdn} \tag{2.5}$$

Here θ is the observed ellipticity (deg), c is the Cht concentration (mg/mL), d is the path length of the cuvette (0.1 cm), and n is the number of peptide bonds in Cht (n for Cht is 241 based on its PDB database entry).

As a control experiment, a protein sample was heated in a water bath to 100 °C and an oil bath to 150 °C for 40 min. Further, the protein thermal stability was measured by increasing the temperature from 25 °C to 105 °C and recording every 2 °C with 1 min equilibrium time and 2 s averaging time. The heating rate was set to 5 °C per minute. The mean residue molar ellipticity was measured at 230 nm which corresponds to the α-helix structure.

A Boltzmann fit (Equation 2.6) of signal was done by Origin 9.1 software.

$$y = A_2 \frac{(A_1 - A_2)}{1 + \exp\left(\frac{x - T_{M,app}}{dx}\right)} \tag{2.6}$$

The center of the sigmoidal curve, defined as the melting temperature $T_{M,app}$ of Cht, is approximately 60°C.

2.2.11 ThermoFluor assay of protein unfolding

SYPRO orange dye was used to test the Cht thermal unfolding and aggregation kinetics.[91] The dye can generate a strong fluorescence yield once bound to the hydrophobic interior of the protein which can be exposed by thermal unfolding. Aggregation of protein can be monitored by the flurescence signal decrease due to protein precipitation. Cht was diluted in Cht stock buffer to 5 μM mixed with 200X diluted SYPRO orange solution (S6651, Thermo Fisher Inc). Samples

were kept in a 96 well plate and heated from 25 °C to 99 °C with a 30 s equlibrium time and 0.5 °C increment. The fluorescence measurements were obtained by q-PCR (CFX96 touch, Biorad).

2.3 Results and discussion

First, we analyzed the temperature response of AuNPs and the surrounding medium in response to nanosecond laser pulses. As shown in Figure 2.1A, the AuNP sample was irradiated by a 532 nm nanosecond laser. When measuring the bulk solution temperature with a thermal couple, no temperature change in the medium was observed from the laser treatment (Figure 2.1C), indicating that the thermal response is limited to the nanoscale. We then analyzed the heating of an individual AuNP by using AuNP optical absorption properties and solving the heat conduction equation. Figure 2.1B shows the temperature profile of a single nanoparticle after a single 6 ns laser pulse exposure. The temperature of AuNPs rises rapidly due to plasmonic absorption. The temperature with AuNP is uniform due to the small size and high thermal conductivity (thus very small Biot number). The heat diffuses from AuNP to the surrounding water and causes a significant temperature increase and steep temperature gradient within several nanometers around AuNP. Importantly, the temperature rise is limited to the nanoparticle and its immediate surrounding medium. Because the laser input energy is insufficient to heat up the entire solution (Figure 2.1C). When measuring the bulk solution temperature with a thermal couple, no temperature change in the medium was observed from the laser treatment, indicating that the thermal response is limited to the nanoscale. This is fundamentally different from photothermal therapy, which requires macroscopic temperature changes that lasts seconds to minutes and lead to cell death within the entire tumor.[92] This nanoscale confinement can cause significant superheating to the water

adjacent to the nanoparticle and previous studies have confirmed that the water can be superheated to 85% of its critical temperature, or up to 276 °C, without vaporization.[30, 93, 94] The laser energy density values used in this study are considered below the vaporization threshold based on previous measurements (400 mJ cm^{-2} for 250 nm gold nanoshells and 10 ns laser pulse, and dramatically increased vaporization threshold for smaller AuNP).[95] To further confirm the nanoscale GNP heating, we measured the photoacoustic signal (Figure A1) corresponding to thermoelastic expansion of the GNP and water,[34] which is a result of the nanoscale heating. Furthermore, gold nanocrystals have vortexes and edges (Figure A5) and lead to higher heat generation[96] and altered temperature distribution of water around the AuNP. The effect of AuNP shape on the nanosecond thermal responses and protein inactivation will be demonstrated in Chapter 4.

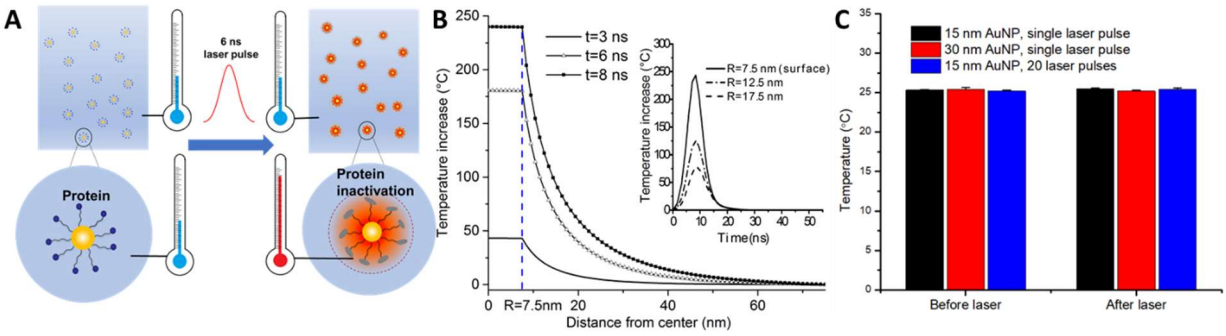

Figure 2.1. Plasmonic heating of AuNP with nanosecond laser pulses. (A) The nanosecond laser pulse heats up AuNPs without increasing the solution temperature. The nanoscale plasmonic heating induces protein inactivation adjacent to AuNP. (B) Spatial and temporal temperature profile (from room temperature) of 15 nm AuNP in response to a 6 ns laser pulse with a Gaussian profile (87 mJ cm^{-2}). The heating is confined tens of nanometers within the AuNP surface and lasts less than 25 ns (insert). The experimental conditions do not cause vapor bubble formation. (C) The nanosecond heating does not change the bulk temperature of the AuNP solution. The temperature was measured before and after laser pulse irradiation for 15 nm and 30 nm AuNP solutions. The laser energy densities used here are consistant with the highest energy used in the protein inactivation experiment. Briefly, for single pulse, the energy densities of laser are 603 ± 5 mJ cm^{-2} (15 nm AuNP) and 611 ± 6 mJ cm^{-2} (30 nm AuNP). For 20 laser pulses, energy of 248 ± 4 mJ cm^{-2} per pulse was used. There is no measurable bulk temperature change after laser irradiation even at the highest laser energy level.

Next, we demonstrated experimentally that proteins adjacent to AuNP can be efficiently and selectively unfolded and inactivated by nanosecond laser pulses. AuNP with a diameter of 15 nm were synthesized. First, AuNP was mixed with egg white and treated by nanosecond laser pulse. Compared with bulk heating (100 °C, 10 min) that causes egg white protein unfold and aggregate (i.e. opaque appearance), the nanosecond laser pulse doesn't change sample macroscopic properties (i.e. stays transparent, **Figure 2.2A**). This shows that the nanosecond laser pulse selectively causes nanoscale protein unfolding and inactivation close to AuNP, without affecting most proteins that are not bound to AuNP. To further investigate the selective protein inactivation, proteins were either absorbed directly to the AuNP or conjugated with a polyethylene glycol (PEG, 1 kDa) spacer between the protein and AuNP. Here we used a protein enzyme, α-chymotrypsin (Cht), as its activity can be readily measured by a colorimetric assay. Approximately 15 Cht molecules are bound to one 15 nm AuNP (Figure A4). To check the Cht thermal stability, circular dichroism (CD) spectrum of Cht was performed (Figure A2). The denaturation temperature for Cht α helix structure was found to be 59 °C under both bulk and slow heating. After applying a single 6 ns laser pulse, the activity of Cht-AuNP conjugate showed a laser energy dependent inactivation (Figure 2.2B). When Cht was not conjugated to the AuNP or no AuNP was present, the protein remained intact and catalytically active. The addition of the 1 kDa PEG spacer between AuNP and Cht required an increase in the laser energy to achieve similar level of protein inactivation. Specifically, the 1 kDa PEG spacer increased the laser pulse energy required for 50% of protein inactivation from 82 to 127 mJ cm^{-2}. This is because the presence of PEG molecules increases the distance between Cht molecules and AuNP. The PEG spacer length can be calculated using a previously reported method,[84] leading to an estimated PEG layer thickness in the range of

2.28 nm (mushroom structure) to 7.95 nm (fully expanded) as detailed in the supplemental information. Since the temperature decreases rapidly from the AuNP surface, the local temperature change that the protein experiences in the presence of a PEG spacer is much lower than the case without the PEG spacer.

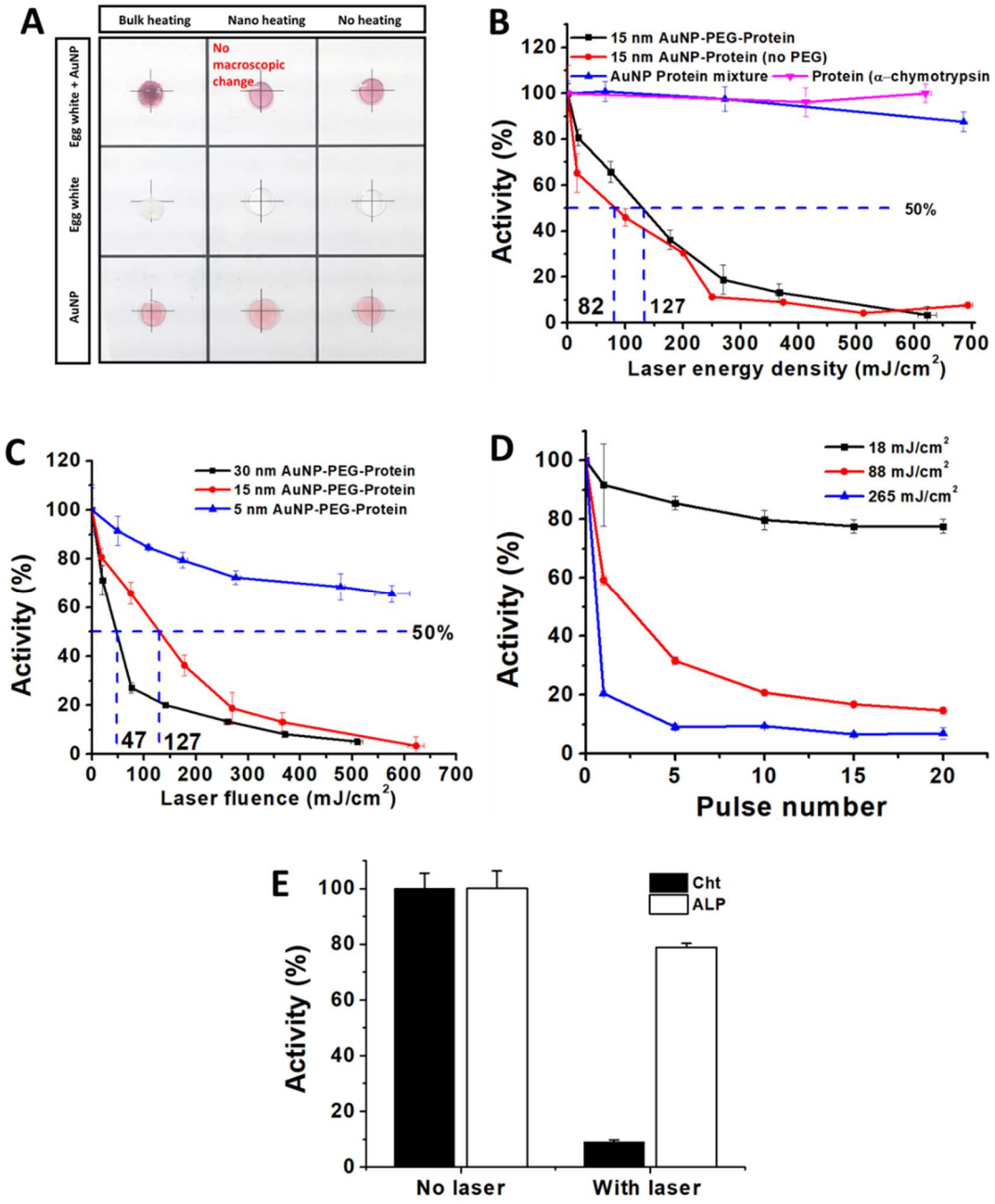

Figure 2.2. Experimental characterization of the nanosecond protein inactivation. (A) The nanosecond protein inactivation is specifc to proteins around the AuNP surface. Inactivation or denaturation of egg white make itself opaque. First column shows bulk heating of the egg white-AuNP mixture, egg white only, and AuNP only, while the second and third columns show the nanoscale heating and no treatment for the same samples, respectively. The bulk heating changes the egg white and egg white-AuNP mixture to an opaque appearance, compared with the transparent appearance of nanoscale heating treatment and no treatment. A background cross label

is used for visualization. Laser pulse energy density is 114 ± 4 mJ cm^{-2} for the nanoscale heating. (B) Effect of the distance between AuNP and protein on the protein inactivation. Legends: Protein refers to α-chymotrypsin (Cht); AuNP protein mixture refers to simply mixing Cht with the polyethylene glycol (PEG) protected AuNP without conjugation; 15 nm AuNP-PEG-Protein refers to α-chymotrypsin conjugated onto AuNP via 1kDa PEG spacer; 15 nm AuNP-Protein refers to α-chymotrypsin conjugated to AuNP by electrostatic absorption. (C) Effect of AuNP size on the protein inactivation (diameter, 5 nm, 15 nm and 30 nm). Protein is conjugated to AuNP surface via a 1 kDa PEG spacer. (D) Effect of laser pulse number on the protein inactivation; and (E) Specificity of the nanosecond protein inactivation. ALP refers to alkoline phosphatase. Cht is conjugated to AuNP surface while ALP is not conjugated to AuNP surface. Laser energy density is 510 ± 25 mJ cm^{-2}, AuNP size is 15 nm.

We further studied different AuNP sizes (5 nm, 15 nm and 30 nm) and found that the larger 30 nm AuNP requires less laser energy for Cht inactivation compared with smaller 5 nm and 15 nm (Figure 2.2C). The laser pulse energy required for 50% protein inactivation reduced from 127 mJ cm^{-2} for 15 nm AuNP, to 47 mJ cm^{-2} for 30 nm AuNP. Interestingly for 5 nm AuNP, the protein activity remained at 66% even at a very high laser pulse energy density 576 mJ cm^{-2}, while all protein activity was lost when conjugated to 15 nm and 30 nm AuNP. This clearly demonstrates that the protein inactivation due to the nanoscale plasmonic heating is strongly size dependent, since large AuNP absorbs more laser energy than smaller AuNPs and thus leads to higher temperature changes. Next, we examined the use of multiple laser pulses (Figure 2.2D). The catalytic efficiency of Cht continued to decrease for up to 10 laser pulses, beyond which no further loss in protein activity was observed. The final protein inactivation at 10 laser pulses shows a strong laser pulse energy dependence. Finally, we demonstrated that protein inactivation is specific to the protein that is tagged or linked to the AuNP in solution. By linking AuNP to Cht but not alkaline phosphatase (ALP), the Cht activity was selectively reduced without significantly affecting the function of ALP. As shown in Figure 2.2E, one laser pulse decreased the Cht activity

to 9% but ALP activity still stayed high at 79%. The slight decrease in the ALP activity may be due to some passive absorption of ALP to AuNP.

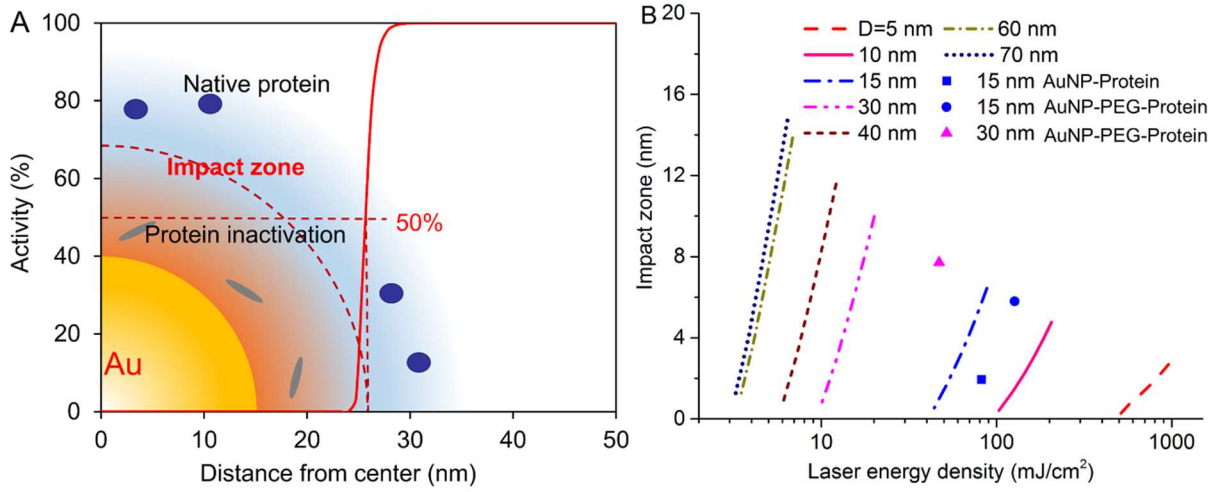

Figure 2.3. Impact zone for the nanosecond laser pulse induced protein inactivation around AuNPs. (A) Schematic of the protein cinactivation impact zone and analytical result of the predicted protein activity due to the nanoscale heating. (B) Effect of laser energy and AuNP size on the impact zone.

Furthermore, we analyzed the kinetics of nanosecond plasmonic heating-induced protein inactivation. Molecular dynamic simulations of protein unfolding at elevated temperatures (up to 550 K) have suggested that proteins can unfold as fast as within nanoseconds.[97, 98] However, the experimental measurement at such short time scales has been challenging. Earlier T-jump experiments measured protein unfolding kinetics within milliseconds [99] and recently a laser gold film heating study by Steel et al. confirms protein unfolding and inactivation within tens of nanoseconds.[43] Further comparison of the measured protein inactivation rate suggests that protein inaction follows an Arrhenius behavior, although the inactivation rate spans over 10 orders of magnitude (k, 10^{-3} to 10^{8} s^{-1}) in a wide temperature range. As an approximation, the nanosecond protein inactivation around AuNP was calculated using the Arrhenius kinetics (activation energy

= 244.05 kJ mol-1, and frequency factor = 9.75×1038 s-1).[99] The result suggests that the combination of the rapid temperature rise and the sharp temperature gradient creates a highly localized region of protein inactivation next to the nanoparticle surface, referred to as the impact zone. Here we quantitatively define the impact zone (z) as the distance between the AuNP surface to the position where the protein has 50% of its original activity after the nanosecond laser pulse treatment (Figure 2.3A).

$$z = R_{50\%} - R_{NP} \tag{2.7}$$

By analysing a range of AuNP sizes (5 nm to 70 nm) and laser pulse energies, the impact zone ranges from 0 nm up to 16 nm (Figure 2.3B). Larger nanoparticles require less laser intensity to inactivate proteins and also generate larger impact zones, due to the higher laser energy absorption and lower surface-to-volume ratio for heat dissipation. Very small 5 nm AuNP gives a very small impact zone and thus does not inactivate proteins efficiently as evidenced by our measurement (Figure 2.2C). Also, increasing laser energy density for the same AuNP size increases the impact zone due to the higher temperature which accelerates protein unfolding and inactivation, consistent with our experimental observations in Figure 2.2. Here we note that the increase in laser energy is limited by the possibility of vaporization which has been shown to repel the protein from AuNP surface with shorter picosecond laser pulse durations.[100] Further comparison of the theoretical analysis and experimental measurement shows that the laser energy for the protein inactivation is on the same order of magnitude (tens to hundreds of mJ cm^{-2}). Here, the location of the protein was taken as 1.9 nm based on a spherical protein shape approximation.[101] The length of the 1 kDa PEG spacer was estimated to be approximately 4.0 nm for 5 nm AuNP, 3.9 nm for 15 nm AuNP and 5.8 nm for 30 nm AuNP based on hydrodynamic measurements

(Figure A3). The slight difference in the PEG length estimation may be attributed to the different footprint of PEG on the two AuNP sizes.[83]

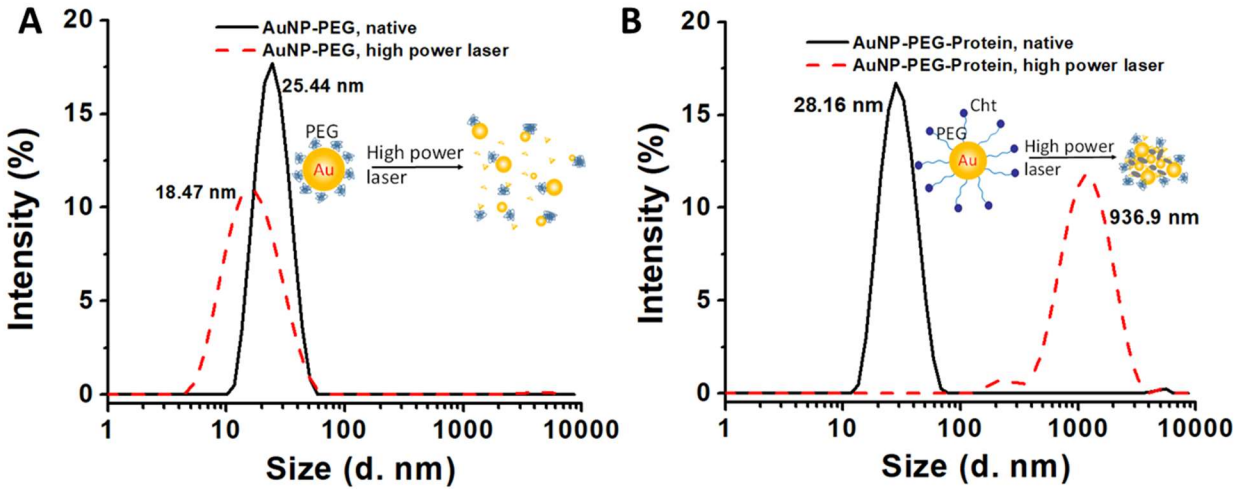

Figure 2.4. Protein unfolding leads to aggregation of protein-AuNP conjugate at high laser intensities. (A) PEG-coated AuNP is sTable under all laser intensities attempted (up to ~609 mJ cm^{-2}). (B) High laser intensity (609 mJ cm^{-2}) leads to protein-AuNP conjugate aggregation while moderate laser intensity (137 mJ cm^{-2}) does not cause aggregation.

Lastly, we examined the fate of AuNP and AuNP-protein conjugate after laser treatment. By comparing TEM images (Figure A5) before and after the laser treatment, no significant AuNP structure change was observed at moderate laser intensities (137 mJ cm^{-2}) while AuNP fragmentation was observed at high laser intensity (~600 mJ cm^{-2}). This is consistent with previous reports on the laser fragmentation of plasmonic nanoparticles with high laser intensities.[102] Interestingly, when comparing PEG and Cht conjugated AuNP, the PEG coating stabilizes the AuNP while the Cht-AuNP conjugate shows significant aggregation after high energy laser pulse treatment, as seen in the DLS (**Figure 2.4**), agarose gel electrophoresis (Figure A6), and UV-Vis measurements (Figure A7). This is possibly a result of protein unfolding, which exposes the

hydrophobic interior and leads to the aggregation of the Cht-AuNP conjugate, similar to the protein aggregation after complete unfolding (Figure A8).[103, 104]

2.4 Conclusion

In conclusion, the nanosecond plasmonic AuNP heating selectively unfolds and inactivates targeted proteins and offers a novel platform to remotely manipulate protein structure and activity without genetic modification. The effects of AuNP size, laser energy and pulse number on the protein inactivation process were systematically studied. Our findings not only quantified the protein inactivation kinetics but also revealed the aggregation behaviour of protein-AuNP conjugates at high laser intensities and thus significant protein unfolding. Further work is warranted to investigate the ultrafast kinetics of the protein unfolding by time-resolved X-ray scattering[105-107] and detailed structural change using hydrogen/deuterium exchange and mass spectrometry (H/DX-MS).[108-110] In particular, further work is needed to understand the mechanism and kinetics of protein unfolding at these extremely high temperatures and very short time scales (nanoseconds). Furthermore, the selective protein inactivation combined with nanomaterial labeling may prove useful for basic protein functional research,[64, 111, 112] remote control of biological activity and behavior, and in therapeutic applications.

CHAPTER 3

TRANSIENT PHOTO-INACTIVATION OF CELL MEMBRANE PROTEIN ACTIVITY WITHOUT GENETIC MODIFICATION BY MOLECULAR HYPERTHERMIA

This chapter has been published as a paper in ACS Nano: Kang, P.; Li, X.; Liu, Y.; Shiers, S. I.; Xiong, H.; Giannotta, M.; Dejana, E.; Price, T. J.; Randrianalisoa, J.; Nielsen, S. O.; Qin, Z., Transient photoinactivation of cell membrane protein activity without genetic modification by molecular hyperthermia. ACS Nano 2019, 13, 12487-12499.

3.1 Introduction

Selective and remote manipulation of protein function in living systems is important to elucidate the protein function and develop precise therapeutics for disease treatment. Advances in tool development have made significant impact in this direction. Among the various modalities, optical control of protein activity in live cells offers unparalleled spatial and temporal resolution. Current approaches include optogenetics,[113, 114] chromophore-assisted light inactivation (CALI)[115, 116] and synthetic photoswitches.[53, 117] Optogenetics uses light to control cell activity, especially in neurons that have been genetically modified to express photo-sensitive proteins. Over the last decade, this technique has been instrumental in our understanding on how specific cell types contribute to brain activity and neurological diseases. While it has had transformative impact in the field, optogenetics requires genetic modification to enable the photosensitivity of target proteins. CALI is probably the most general method for optical control of protein activity with high spatial and temporal resolution and has been used in many areas in cell biology. CALI utilizes a photosensitizer to produce reactive oxygen species (ROS) and inactivate the adjacent proteins during light exposure. While small molecule photosensitizers (typically xanthene-based) have a high efficiency to generate ROS, it is challenging to design small molecules to target proteins in live cells. On the other hand, photosensitizers such as KillerRed are genetically encoded in target cells. Importantly, CALI efficiency is dependent on the expression level of photosensitizer when genetically encoded and on the cellular microenvironment such as oxygen concentration and endogenous reducing agent (glutathione).[64] Synthetic photoswitches (*e.g.* based on azobenzene) have also emerged as a promising strategy to control protein activity with light, but currently there are a very limited number of photoswitches and thus narrow options of light source (*i.e.*

wavelength). Therefore, it remains challenging to optically control protein activity in live cells without genetic modification and independent of the cellular microenvironment.

Nanoparticles provide an interface to manipulate the function of living systems from cells[118, 119] to macromolecules such as proteins.[120] Cellular behavior control with noninvasive stimulation such as magnetic,[121, 122] acoustic[123] and optical methods[60] can be achieved with the assistance of nanoparticles. Among these stimulation methods, optical control of cellular behavior[76, 124] using plasmonic nanoparticles provides the highest spatiotemporal resolution, including neuron firing,[59, 60, 125-127] heat shock protein expression,[68] and optoporation.[35, 128, 129] Continuous photothermal stimulation of plasmonic nanoparticles leads to global heating in the tissue (Figure. 1) and has been used for hyperthermia therapy of cancer. Physically, it is possible to apply short laser pulses to excite plasmonic nanoparticles and create a nanoscale hotspot, or "thermal confinement" when the pulse duration is less than the timescale of heat diffusion.[30, 41, 130] The possibility of "molecular hyperthermia" (MH) was introduced recently, defined as using ultrashort laser pulses (nanosecond) to excite a plasmonic gold nanoparticle (AuNP) as a nanoheater to unfold and inactivate targeted proteins with a very well-defined impact zone (on the nanometer length scale).[41, 99, 131] The heating is confined within nanometers of the nanoparticle (nanoscale hotspots) and doesn't cause bulk heating, which allows for the possibility to control protein activity without affecting the cell viability. While it has been shown that MH can photo-inactivate isolated proteins of interest, it remains unclear whether MH works in complex cellular environments.

In this report, we demonstrate that MH can inactivate protein *in situ* and control cellular activity with two examples. In the first example, we targeted a membrane receptor, protease

activated receptor 2 (PAR2), which is important in pain sensitization signaling.[132, 133] Ca^{2+} imaging analysis demonstrates that PAR2 can be inactivated *in situ* by MH without compromising cell proliferation. In the second example, we demonstrate the photo-inactivation of a tight junction protein in brain endothelial monolayers, which is important in maintaining the blood-brain barrier (BBB),[134, 135] but also limits therapeutic delivery to the brain. MH of tight junction protein (junctional adhesion molecule A, or JAM-A) leads to a reversible BBB opening *in vitro* that recovers within 6 hours. We further demonstrated that the energy levels for MH is insufficient to form vapor nanobubbles around AuNP. Our results indicate that MH is a promising approach to manipulate protein activity in live cells without genetic modification and develop therapeutics with high spatiotemporal resolution.

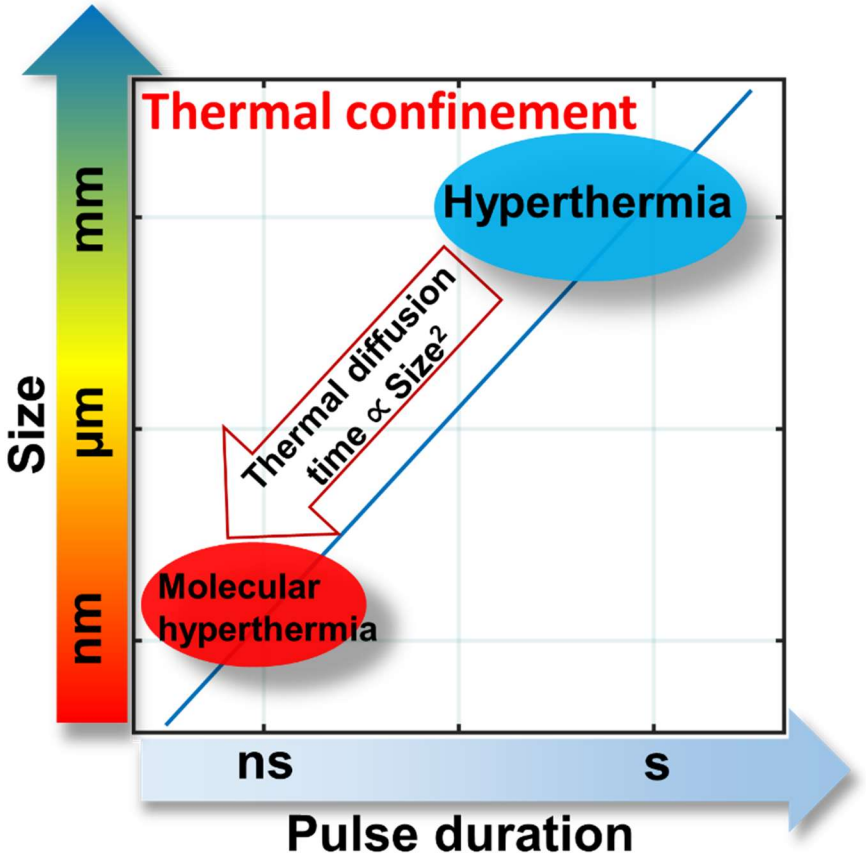

Figure 3.1. Schematic to illustrate the time and length scales of molecular hyperthermia (MH) compared with hyperthermia. Area left of the line represents thermal confinement. The thermal diffusion time is proportional to the square of size.[136]

3.2 Methods

3.2.1 Reagents and cells

Tetrachloroauric (III) trihydrate ($HAuCl_4 \cdot 3H_2O$: 99.9%), sodium citrate tribasic dehydrate (≥99%) and hydroquinone (≥99%) were purchased from Sigma-Aldrich. Heterobifunctional polyethylene glycol OPSS-PEG-SVA (3.4 kDa, OPSS-PEG-SVA-3400) were purchased from Laysan Bio Inc. Poly(ethylene glycol) 2-mercaptoethyl ether acetic acid (Thiol-PEG-Carboxyl,

600 Da, PG2-CATH-600) were purchased from Nanocs Inc. Fluorescein isothiocyanate–dextran (FITC-dextran) and WST-1 cell proliferation reagent (05015944001) was purchased from Sigma-Aldrich. Propidium iodide (PI) is purchased from Cayman chemical (14289). Mouse IgG isotype control (Ctrl Ab, 31901) was purchased from Invitrogen. Anti-PAR2 antibody (MAB3949) was purchased from R&D systems. Anti-JAM-A antibody BV16 was kindly provided by Dr. Elisabetta Dejana's lab.[134] Human cerebral microvessel endothelial cells (hCMEC/D3) were purchased from EMD Millipore. HEK293 cell with Ca^{2+} indicator TN-XXL was kindly provided by Dr. Paul Slesinger's lab.[137] PAR2 agonist 2-aminothiazol-4-yl-LIGRL-NH_2 (2AT) was provided by Dr. Theodore Price's lab.[138] Somatostatin (SST) was purchased from Sigma-Aldrich (S9129). Pierce modified lowery protein assay kit was obtained from ThermoFisher Scientific (23240).

3.2.2 Gold nanoparticle synthesis

AuNP seeds were synthesized following the modified Frens' method.[79] Briefly, 1 mL $HAuCl_4$ (25 mM) was added to 98 mL pure water and allowed to boil on a hot plate with vigorous stirring. 1 mL sodium citrate (112.2 mM) was then added swiftly and reacted for 10 minutes. After cooling the solution to room temperature, water was added to bring the volume to 100 mL. The AuNP seeds had a concentration of 2.23 nM and average size of 15 nm in diameter. AuNP seeds were stored in room temperature and used within one week.

To synthesize 45 nm AuNPs, we first mixed 94.4 mL pure water with 973 µL $HAuCl_4$ (25 mM), 973 µL sodium citrate (15 mM) and 3.7 mL AuNP seeds (2.23 nM). With vigorous stirring, 973 µL hydroquinone solution (25 mM) was injected rapidly. The solution quickly switched color to purple and then to red in a few minutes. The reaction was done overnight at room temperature.

Then the 45 nm AuNPs were concentrated by centrifugation (1300 g, 30 minutes) and stored at 4 °C for use within one month.

3.2.3 Surface modification of AuNPs and characterization.

Antibody conjugation to AuNP was performed following a previously reported protocol.[139] First, the antibody for PAR2 or JAM-A was dissolved in phosphate buffer saline (PBS, 1X, pH=7.4) with a concentration of 0.5 mg/mL. To modify the PEG onto the antibody, the antibody solution was then added in OPSS-PEG-SVA solution (0.03mg/mL in 2 mM borate buffer, pH=8.5) with molar ratio as 1:132.[139] The tubes were slowly rotated for 3 hours at room temperature. To remove extra PEG molecules, the solution was dialyzed (20 kDa dialysis bag, Spectra/Pro Biotech, 131342T) overnight at 4 °C. To modify the AuNP surface with antibody, 45 nm AuNP colloidal solution was added to PEG-antibody conjugate solution with molar ratio of 1:150 and reacted at room temperature for 3 hours. Then 100 μL Thiol-PEG-Carboxyl (4 mg/mL, in 2 mM borate buffer, pH = 8.0) was added into 1 mL AuNP solution to backfill the AuNP surface. For the AuNP-PEG sample, Thiol-PEG-Carboxyl solution (2 mg/mL, in 2 mM borate buffer, pH=8.0) was added into bare AuNP solution with the molar ratio 1:150. Particles were then washed with borate buffer 3 times (1300 g, 30 minutes, with 0.5% tween-20) and then re-suspended in cell medium for further experiments. To confirm the antibody conjugation efficiency, we measured protein concentration in the supernatant after centrifugation by the Pierce-modified Lowry assay after antibody conjugation to AuNPs. The standard curve was obtained by measuring standard BSA dilutions. After considering that the signal ratio between mouse IgG and BSA is 1.2 from the user manual in the Pierce-modified Lowry assay, a standard curve of IgG was obtained. The numbers of

antibodies/AuNP was calculated by subtracting the free antibody number from the initial total antibody quantity and divided by the AuNP concentration.

Dynamic light scattering (DLS) (Malvern instruments, Nano ZS) and UV-vis spectrometer (BioTek Synergy 2) were used to characterize the nanoparticle conjugation. The AuNP concentration was determined with the Beer-Lambert law (Equation 2.3-2.4). Size of the particle (D) was determined by transmission electron microscope (TEM) (JEOL 1400+, 100 keV). The AuNP solution was carefully dropped on a copper mesh (PELCO 160, PELLA Inc.) and air-dried for 2 hours before TEM imaging.

3.2.4 Western blotting

Western blotting experiments were performed following the procedure reported before.[140] Male mice (C57BL/6) were sacrificed by decapitation under anesthesia as approved by IACUC at University of Texas at Dallas. The DRG neuron tissues were collected and flash frozen on dry ice. The lysis solution (50 mM Tris-HCl buffer, 150 mM NaCl, 1 mM Ethylenediaminetetraacetic acid (EDTA), 1% Triton X-100, pH=8.0, with protease and phosphatase inhibitors) was used to homogenize frozen DRG tissues. The sample was then centrifuged at 14000 rpm for 15 minutes at 4 °C. Protein was then separated into 10% SDS-PAGE gel, and transferred onto 0.45 PVDF membrane (Millipore, IPVH00010) at 30V overnight at 4 °C. The concentration of protein was checked with BCA assay to confirm the protein quantity was the same for different samples. To reduce the non-specific binding, the membrane was blocked with 5% non-fat milk powder (NFDM, Bio-rad, 1706404) dissolved in 1X Tris-HCl buffer containing 1% Tween-20 for 3 hours. Subsequently, membranes were washed with 1X Tris buffered saline with 0.1% Tween-20 (TTBS,

pH=7.5, VWR) 3 times for 5 minutes each. Then primary antibody (MAB3949, 5 μg/mL) was used to incubate overnight at 4 °C. The membrane was then washed with 1X TTBS 3 times for 5 minutes each and incubated with secondary antibody at room temperature for 1 hour. Antibody for Glyceraldehyde 3-phosphate dehydrogenase (GADPH) was used to stain GADPH to check that the same number of cells were added for both samples. The membrane was then washed with 1X TTBS 6 times for 5 minutes each. The band signal was then generated with immobilon western chemiluminescent HRP substrate (Millipore, WBKLS0500) and detected by Bio-Rad ChemiDoc Touch (Hercules, CA).

3.2.5 Ca^{2+} measurement with plate reader

HEK393 cells with Ca^{2+} indicator were cultured in 75 mL cell flask with cell medium (1% Pen Strep, 10% FBS in DMEM) in 37°C and 5% CO_2. The day before the experiments, cells were seeded on a collagen coated 96 well plate (Costar, 3603). Cell culture medium was replaced by 100 μL artificial cerebral spinal fluid (ACSF; 125 mM NaCl, 5 mM KCl, 10 mM D-glucose, 10 mM HEPES, 3.1 mM $CaCl_2$, 1.3 mM $MgCl_2$, pH=7.4) for each well at 30 minutes before Ca^{2+} measurements. The signal was then monitored in a plate reader (Biotek Synergy H4), with light excitation of 436 nm, and the cyan (ECFP) and yellow (Citrine) signals were collected at 485 ± 10 nm and 527 ± 12 nm with 9 s interval. After reading baseline for 3 minutes, 50 μL of agonist in ACSF was mixed into each well, and the signal was then collected for another 4 minutes. The fluorescence resonance energy transfer (FRET) ratio change ΔR/R was calculated with the following equation:

$$\frac{\Delta R}{R} = \frac{Fluorescence\ 527}{Baseline\ 527} \Big/ \frac{Fluorescence\ 485}{Baseline\ 485} - 1 \quad (3.1)$$

The maximum FRET ratio change (Max. ΔR/R) indicates the PAR2 activity. SSTR2 activity was measured following the same procedure as PAR2.

3.2.6 Transendothelial electrical resistance measurement.

The hCMEC/D3 cells were incubated in EndoGRO-MV complete media with FGF-2 supplement (Millipore, SCME004) on a collagen-coated porous membrane in a transwell filter insert (Falcon, 353097, 6.4 mm membrane diameter). Cells were cultured for 6 to 7 days at 37 °C and 5% CO_2 to form a tight monolayer.

TEER measurements were performed to monitor the cellular monolayer formation as well as the BBB opening by MH. Briefly, Millicell ERS-2 Voltohmmeter (Millipore, MERS00002) was used to measure the electrical resistance across the cellular monolayer. The resistance of collagen-coated culture membrane (no cells) was used as baseline. The TEER value was obtained by subtracting baseline from the resistance of the endothelial monolayer.

3.2.7 Permeability measurement

Permeability measurement was performed to quantify the molecular transport across the cell monolayer barrier. The culture insert was placed in the serum free cell medium. Cells were incubated in 37 °C and 5% CO_2 for 30 minutes. FITC-dextran solution with different molecular weights (300 µL/well, 1 mg/mL, in cell medium) was added into the well. Culture medium from the bottom well was sampled at different times to obtain the concentration of FITC-dextran that

had crossed the cellular barrier. The permeability (P_{app}, cm/s) was calculated with the following equation:

$$P_{app} = \frac{dQ}{dt}\frac{1}{AC} \tag{3.2}$$

Here Q is the quantity (mg) of molecules that have diffused through the cell monolayer, t is time duration (s), A is the membrane area (cm^2), and C is the initial concentration of FITC-dextran (mg/mL).

3.2.8 Immunocytochemistry staining

Cells were first seeded on a glass bottom Petri dish (MatTek, P35G-0-10-C) one day before the experiment. To check the AuNP targeting site on live cells, the AuNP samples (0.5 nM) were then incubated with cells for 15 mins at 4 °C. The cells were rinsed by ACSF 3 times. Then 100% methanol was used to fix the cell. The secondary antibody (Alexa 488 or Alexa 647 conjugated donkey anti-mouse IgG, 0.2 μg/mL) was then incubated with cells for 1 hours under room temperature. Free secondary antibody was removed by washing with PBS. Then cells were washed carefully with PBS buffer. Cell nuclei were stained with Hoechst 33342 (5 μg/mL) for 7 minutes. Cells were finally washed with PBS 3 times and imaged under a confocal microscope (Olympus FV3000RS). We also conducted ICC experiments on prefixed cells. Briefly, 100% methanol was used to fix the cell first. After 5 minutes and washing with PBS (1X, pH=7.4), cells were incubated with blocking buffer (2% BSA, 5% donkey serum, 0.05% Tween-20) for 2 hours at room temperature. The primary antibodies or AuNP samples were then incubated with cells (MAB3949 (10 μg/ml), BV16 (5 μg/mL), AuNP samples (0.5 nM)) overnight at 4 °C. The secondary antibody staining steps and Hoechst staining steps are same as the procedure described before. The green

channel (FITC filter) shows TN-XXL in HEK293 cell transferred with TN-XXL. The red channel (Alexa 647 filter) shows that secondary antibodies (conjugated with Alexa 647) bind to MAB3949.

3.2.9 Molecular hyperthermia inactivation *in situ*.

Cells were first incubated in 40 μL antibody-modified AuNP in cell culture medium for 30 minutes. To remove free particles, cells were then carefully washed with bath solutions (ACSF for HEK293 cells, PBS for hCMEC/D3 cells). Then laser pulses (Quantel Q-smart Nd:YAG laser, FWHM = 6 ns, 532 nm, diameter of laser beam is 10 mm (Intensity = $1/e^2$)) were used to irradiate directly to each well. The laser energy was monitored with a laser energy meter (FieldMaxII, Coherent USA). After laser irradiation, cells were incubated in the working solution (ACSF for HEK 293 cells, cell medium for hCMEC/D3 cells) for further experiments. To check whether MAB3949 affects PAR2 activity, we incubate HEK293 cells with MAB3949 (0.02-67 nM in ACSF, 100 μL/well) 30 minutes before the Ca^{2+} assay.

3.2.10 Nanobubble signal measurement

AuNP solution was flowed through a glass capillary tube (VitroTube, 82400-050). The pump laser (532 nm, FWHM=6 ns, frequency=50 Hz) and the probe laser (MKS R-30989, 633 nm, continuous wave) were focused and co-localized at the center of the capillary tube. The probe laser signal was recorded by a photodetector (Menlo systems, FPD510). The probe laser energy was adjusted by an optical filter (Thorlab, NDC-25C-2M). The data and nanobubble probability was processed by MATLAB 2016a. The Boltzmann fitting of the probability was calculated in Origin 9.1 software.

3.2.11 Propidium iodide staining

HEK 293 cells were seeded on a circular glass bottom dish for 24 hours before the experiment. The cells were first incubated with AuNP-MAB3949 (0.32 nM) or cell culture medium for 30 minutes. Extra AuNPs were washed away by ACSF. The positive control group was obtained by killing cells with 100% methanol (10 min incubation). Cells of the MH group and laser only group are irradiated with the laser (100 mJ/cm^2, 10 pulses). After laser irradiation, cells are incubated in ACSF for 30 minutes followed by staining with PI for 10 minutes (10 μg/mL in ACSF). Cells are then washed by ACSF. The cells are then fixed with 100% methanol for 10 minutes (including positive control). Hoechst 33324 was used to stain the cell nucleus for counting purposes. Cells were finally washed with PBS 3 times and imaged under a confocal microscope (Olympus FV3000RS).

3.2.12 Ca^{2+} imaging with 2-photon imaging system.

HEK293 cells were seeded on a circular glass slide in a 24 well plate 2 days before the experiment. On the day of the experiment, glass slides were transferred to petri dishes. AuNP-MAB3949 (0.2 nM, 70μL) was added carefully on top of the slide to cover the cells for 30 minutes under 4 °C. Then extra particles were removed from cells and ACSF was used to wash away free particles. We used a black marker to mark the outside of the petri dish and the laser irradiation partially compromises the marker, a convenient method to indicate the laser treated cells. Half of the petri dish was covered with cardboard to block the laser beam (6 mm in diameter) while leaving the other half exposing to the laser. The laser fluence is 100 mJ/cm^2 and 10 pulses were used. A multichannel perfusion system (DWV, 64-1940) was used to load ACSF and drugs (1 μM 2AT in

ACSF). To image the fluorescent signal on the 2-photon system (Olympus MPE-RS twin), the laser excitation wavelength was set at 820 nm. The cyan (ECFP) and yellow (Citrine) emission was set at 485 nm and 527 nm respectively. ACSF was perfused to cells for the first 52s to obtain the baseline followed by perfusing 2AT for 16 seconds. ImageJ was used to analyze the images.[141] The regions of interest (ROI) were drawn near the edge of laser irradiation. ΔR/R was calculated using Equation (3.1).

3.2.13 WST-1 cell proliferation measurement.

Cells were cultured in a 96 well plate with 50,000 cells per well. Cells of the experimental groups were incubated with 35 μL AuNP-MAB3949 (in cell medium) for 5 to 30 minutes as indicated in the figures, while the control group was incubated with the same amount of cell medium. Extra AuNPs were washed away with ACSF. Then cells were irradiated with the laser (marked as 0 hour time point). ACSF was replaced with 0.1 mL cell culture medium and the cells were then incubated at 37 °C and 5% CO_2. At various time points (30 mintues to 8.5 hours) after laser irradiation, 10 μL WST-1 stocking solution was added to each well. The cells were further incubated at 37 °C and 5% CO_2 for 2.5 hrs. The absorbance was read by a plate reader at 450 nm. The signals were normalized with signals from control samples, *i.e.* cells without laser treatment or AuNP incubation.

3.2.14 Simulation of AuNP plasmonic heating and protein inactivation.

Absorption cross section area (C_{abs}) was calculated by Mie theory and the Discrete dipole approximation (DDA) method. Then the temperature profile was obtained by simulating the heating process of AuNPs by a one nanosecond laser pulse (45 nm AuNP: fluence F = 100 mJ/cm^2,

full width at half maximum or FWHM τ = 6 ns; 3 nm AuNP: F = 280 mJ/cm^2, τ = 1 ns,) using COMSOL 5.3. We assume a homogeneous heating source inside the particle and the volumetric heat generation of the laser pulse with Gaussian shape is defined by Equation 3.3

$$Q_v = \frac{C_{abs}F}{V_{NP}} \frac{2.355}{\tau\sqrt{2\pi}} e^{-\frac{5.546(t-t_0)^2}{2\tau^2}} \quad (3.3)$$

where V_{NP} is AuNP volume, t is time and t_0 = 7.64 ns which is the center of the pulse. Q_v has unit of W/m^3. The thermal interface conductance of the AuNP surface was set as 105 MW/(m^2·K.[142]

3.2.15 Molecular dynamics simulation of AuNP heating:

Molecular dynamics (MD) simulation was performed using the LAMMPS software package. The interactions between gold atoms are described by an embedded atom method (EAM) potential,[143] and the CHARMM TIP3P water model was utilized in the simulation.[144] The interaction between water and gold atoms was considered by prescribing a Lennard-Jones (LJ) 12-6 interaction between oxygen and gold atoms. A cutoff radius of 10 Å was used in the LJ potential to reduce the computational cost. Table B3 reports the parameters for the non-bonded interactions used in the MD simulation. The water domain was set as a cubic box with side length 15 nm. The AuNP was placed in the center of the water domain with a diameter of 3 nm. The water molecules between the box domain and the outside of a spherical domain of 6.5 nm radius were maintained at a constant temperature of 300 K to serve as a heat sink. The laser pulse was treated as a heating source of the gold atoms. The absorption cross-section of the 3 nm AuNP was calculated by Mie theory.[145] During the laser heating, an isoenthalpic-isobaric ensemble (NPH) was prescribed to maintain the overall pressure of the remaining water region at 1 atm.

3.2.16 Statistical information.

Except where otherwise noted, values are reported as mean ± standard deviation (s.d.). Statistical significance analysis was calculated using the two-tailed student t test in MATLAB R2016a. A statistically significant value was denoted with two asterisks (**) for $p < 0.005$.

3.3 Results and discussion

3.3.1 AuNP-antibody conjugation and characterization.

First, we designed and characterized an antibody modified AuNP to target PAR2. PAR2 is an important G-protein coupled receptor implicated in pain.[132, 133] During inflammation or cancer, protease-activated receptors (PAR) are activated by proteolytic cleavage of the extracellular amino terminus and lead to diverse pathologies including pain sensitization.[146] Proteolytic cleavage of the N terminus of PAR2 results in exposure of a tethered ligand that activates the receptor to induce signaling (Figure 3.2A). One consequence of the PAR2 activation in the periphery nervous system is sensitization of neurons responsible for transmitting noxious information to the central nervous system (CNS). Importantly, nociceptive neurons express PAR2, and PAR2 activation on these neurons leads to enhanced signaling *via* a variety of channels including the capsaicin and noxious heat receptor, TRPV1. For instance, PAR2 is responsible for protease sensitization of TRPV1 *in vivo*, leading to thermal hyperalgesia.[147, 148] Thus, targeting and photo-inactivating PAR2 will allow us to control pain signaling (Figure 3.2A). As a routinely used cell line in the PAR2 research community,[149] human embryonic kidney 293 (HEK293) cells were used in this study to investigate PAR2 activity. PAR2 activation leads to intracellular Ca^{2+} concentration increase through the inositol 1,4,5-trisphosphate (IP3) signaling pathway.[150] Here, the FRET sensor (TN-XXL)

monitors Ca^{2+} during PAR2 activation by a specific PAR2 agonist (Figure 3.2B).[138, 151] We selected gold nanospheres with a diameter of 45 nm as nanoheaters due to their relatively high absorption cross section and because they facilitate protein denaturation farther than 10 nm away from themselves.[131, 152]

The prepared AuNP was characterized by transmission electron microscope (TEM) and dynamic light scattering (DLS) to confirm its size and lack of aggregation (Figure B1B and C). Conjugation of poly(ethylene glycol) 2-mercaptoethyl ether acetic acid (Thiol-PEG-Carboxyl) onto AuNP increased the hydrodynamic diameter by 15 nm, in agreement with previous reports.[84] Both PAR2 target antibody (MAB3949) and control antibody (Ctrl Ab) coating further increased the hydrodynamic size by 11-12 nm. UV-Vis measurements showed that the AuNP absorbance peak shifted slightly from 531 nm to 532 nm after conjugating with Thiol-PEG-Carboxyl, and then again to 536 nm after anti-PAR2 antibody (MAB3949) conjugation (Figure B1D). A Western blot experiment was then performed to confirm MAB3949 antibody specificity to PAR2. PAR2 was observed by MAB3949 staining in the dorsal root ganglion (DRG) sample from wild type mouse (PAR2 +/+) at around 50 kDa, with a negative staining for PAR2 knockout mouse (PAR2 -/-, Figure B1E). PAR2 expression on HEK293 cells was also tested and confirmed by immunocytochemistry (ICC) experiments with methanol-prefixed cells (Figure B1F). Furthermore, we show that MAB3949 antibody binds to PAR2 after conjugation onto the AuNP surface by ICC staining on HEK293 cells (Figure 3.2C). Specifically, cells incubated with AuNP-MAB3949 show a clear binding on the cell membrane, while control antibody modified AuNP (AuNP-Ctrl Ab) doesn't bind with the cell membrane. It is worth noting that the cells incubated with AuNP-MAB3949 have relatively stronger signal than the case with MAB3949 in methanol-

prefixed cells. This is because multiple antibodies (57±28 antibodies/AuNP, Figure B2) conjugated on the AuNP amplify the secondary antibody binding and the resulting fluorescent intensity.

3.3.2 Photoinactivation of PAR2 by molecular hyperthermia *in situ*.

Next, we demonstrated that PAR2 can be inactivated by MH on live HEK293 cells. We first tested and confirmed that the engineered HEK293 cell with Ca^{2+} indicator[137] is a robust model to study PAR2 activity. The addition of PAR2 agonist 2-aminothiazol-4-yl-LIGRL-NH_2 (2AT, 330 nM) leads to a robust increase in the citrine channel and decrease in the ECFP channel (Figure B2B). A dose-response curve was then obtained from analyzing the FRET signal (Figure B3C-D). It is worth noting that the FRET signal (ΔR/R) was triggered within 10s after 2AT addition at all concentrations. However, the time duration to reach the maximum ΔR/R reduces with increasing 2AT concentration. Later, we consider the maximum FRET ratio change to compare PAR2 activity.

Then, we tested the effect of MH on PAR2 activity. Three experimental groups were used: MH including PAR2 targeting AuNP (AuNP-MAB3949), control antibody modified AuNP (AuNP-Ctrl Ab), and cells alone with no AuNP treatment (Ctrl). The AuNP was incubated with cells at 4°C to prevent cell uptake. Our results suggest that laser irradiation alone (Ctrl group, 532 nm, 100 mJ/cm^2, and 10 pulses) does not cause a significant difference in either PAR2 activity or cell proliferation (Figure B4A), and the antibody alone (MAB3949) does not change PAR2 activity (Figure B4B). Comparing AuNP-MAB3949 and AuNP-Ctrl Ab under the same laser exposure (532 nm, 100 mJ/cm^2, 10 pulses), a significant drop (>80 %) in PAR2 activity was observed for

the AuNP-MAB3949 group at concentrations above 0.32 nM (Figure 3.2D&E) while there is no significant change for the AuNP-Ctrl Ab group (except at higher AuNP concentration 0.5 nM). Without laser irradiation, neither the AuNP-MAB3949 group nor the AuNP-Ctrl Ab group showed an obvious drop in PAR2 activity (Figure 3.2D&E). Further investigation shows a gradual drop in PAR2 activity as the pulse number and intensity were increased (Figure 3.2F). Also, increasing the incubation time of AuNP to 30 mins does not dramatically change the PAR2 inactivation (Figure B5A). At conditions that lead to a significant PAR2 activity drop in the AuNP-MAB3949 group, we found no significant differences in the cell proliferation between AuNP-Ctrl Ab and AuNP-MAB3949 groups regardless of laser fluence (Figure B5B). This suggests a specific molecular level photo-inactivation by MH. Also, we measured the bulk medium temperature after laser irradiation and confirmed that there is no obvious temperature rise, indicating that the temperature change is limited to the nanoparticle and its immediate surroundings (Figure B5D). Next, propidium iodide (PI) staining was performed to test for possible cellular membrane damage and necrosis (Figure B6). The MH group does not show significant PI signal increase compared with the control groups. This result demonstrates that the MH does not cause membrane damage or necrosis. Finally, we investigated the PAR2 function recovery and cell proliferation at different time points. The PAR2 activity drops to 20% at 1.5 hours after MH treatment, and gradually increase to 80% at 8.5 hours (Figure 3.2G). The reversible PAR2 activity does not directly imply that photo-inactivation process is reversible. The cell is recycling the protein and possibly synthesizing new proteins during this time. As a result, even if the protein inactivation is irreversible, we can still observe protein function recovery after several hours.

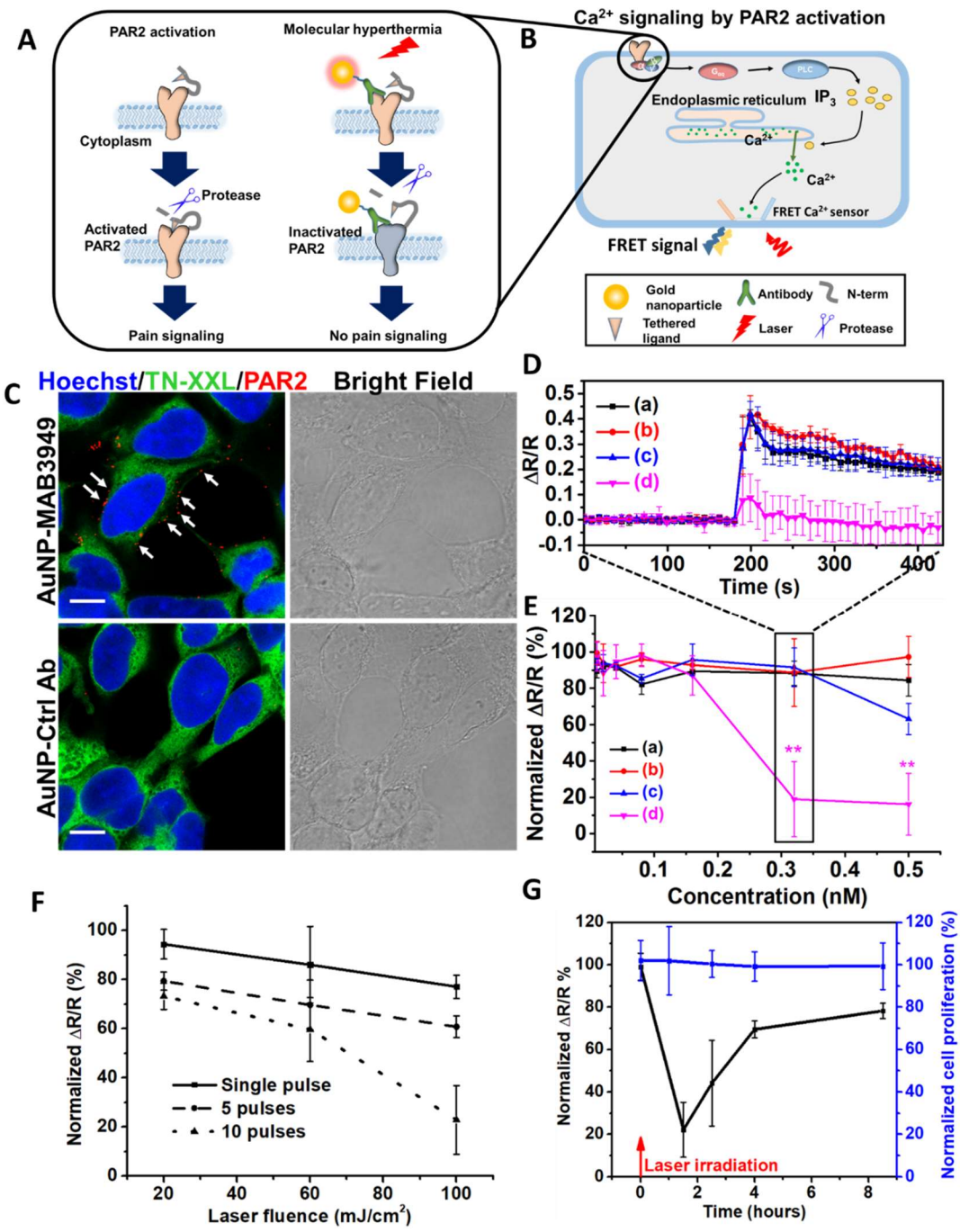

Figure 3.2. Photo-inactivation of PAR2 by molecular hyperthermia. A) Schematic of PAR2 inactivation by molecular hyperthermia. B) Schematic illustrating the Ca^{2+} signaling due to PAR2 activation. $G_{\alpha q}$ is heterotrimeric G protein subunit, PLC is phospholipase C, IP_3 is inositol trisphosphate. C) Fluorescent immunocytochemistry imaging of HEK293 cells. Nucleus is in blue

(Hoechst 33342), FRET Ca^{2+} sensor protein TN-XXL is in green, and PAR2-targeting antibody modified gold nanoparticle (AuNP-MAB3949) is in red (stained by Alexa 647 conjugated secondary antibody, indicated by white arrows), Control antibody modified gold nanoparticles (AuNP-Ctrl Ab) as a control show minimum signal (scale bar: 10 μm), AuNP concentration [AuNP] = 0.5 nM. D) The FRET ratio (ΔR/R) signal for different groups: (a) AuNP-Ctrl Ab, no laser; (b) AuNP-MAB3949, no laser; (c) AuNP-Ctrl Ab, with laser; (d) AuNP-MAB3949, with laser. [AuNP] = 0.32 nM. Laser conditions: 532 nm wavelength, fluence at 100 mJ/cm^2 and 10 pulses. The incubation time for AuNPs is 5 minutes. E) Dose response of PAR2 activity under different particle concentrations for different groups. The groups are color-coded as in Figure 2D. F) Dose-response curve for PAR2 activity under different laser fluence and pulse numbers. [AuNP] = 0.32 nM and AuNP incubation time is 5 minutes. G) PAR2 function recovery and cell proliferation after molecular hyperthermia treatment. The experimental conditions are the same as (d) group in Figure 2D. Laser were irradiated at 0 hour time point (indicated by red arrow). The normalized ΔR/R and cell proliferation indicate normalization with the control group (without AuNP incubation or laser treatment).

3.3.3 PAR2 inactivation in laser-targeted cells.

Furthermore, we demonstrated that MH can switch off protein activity in laser-targeted cells. By incubating cells with AuNP-MAB3949 and exposing only half of the cells to laser pulses, we compared the cellular PAR2 response with and without laser irradiation in the same petri-dish (Figure 3.3A). By perfusing 2AT and imaging under 2-photon microscopy (Figure 3.3B-C), the cell response was imaged at real time. The results suggest that the region without laser irradiation had an obvious Ca^{2+} release after 2AT loading while the region with laser irradiation had a much attenuated Ca^{2+} release (Figure 3.3D). The 10s delay of Ca^{2+} release after 2AT loading is probably due to the drug diffusion from the loading pipette to cells. This result suggests MH allows laser targeting of selected cells to photo-inactivate PAR2 activity.

3.3.4 Molecular selectivity of PAR2 inactivation by MH.

Finally, we tested the molecular specificity of PAR2 inactivation. We used HEK293 cells transferred with somatostatin receptor 2 (SSTR2), another GPCR protein that can be activated by

somatostatin (SST) (Figure 3.3E). We then inactivated PAR2 by MH and measured SSTR2 and PAR2 activities. The results show that the SSTR2 activity remains the same as the control groups while the PAR2 activity reduces by 50% (Figure 3.3F and Figure B7). This demonstrates that MH can selectively switch off the activity of targeted cell receptors while not affecting other cell membrane receptors. We note that the molecular specificity is not due to laser focusing on specific receptors since this is well below the diffraction limit and not physically possible. Instead, the nanoparticles target specific receptors and the laser excites the targeted nanoparticles to inactivate the receptor, while leaving other non-targeted receptors intact.

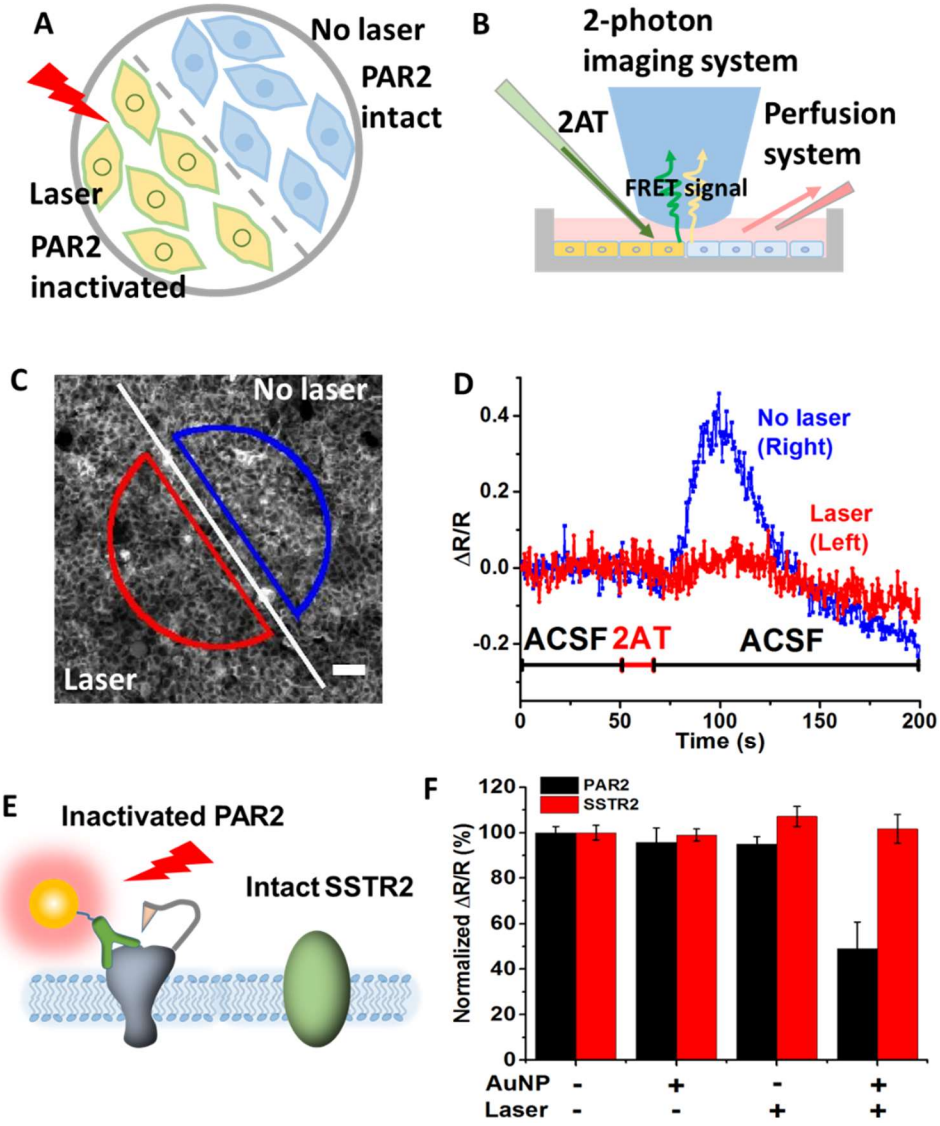

Figure 3.3. High spatial resolution and molecular specificity for PAR2 photo-inactivation by molecular hyperthermia. A) Experimental design: after targeting PAR2 with AuNP-MAB3949, half of the cells were blocked from laser irradiation. B) Experimental setup including 2-photon imaging of cytoplasmic Ca^{2+} release. C) Fluorescence images of cells after laser irradiation (scale bar: 50 μm). The line indicates the border of laser irradiation, with the bottom left side receiving laser irradiation (ROI in red) and the top right side without laser irradiation (ROI in blue). D) Ca^{2+} signals for different ROIs. The red line is the FRET ratio from the cells in the red semicircle (with laser) and the blue line indicates the FRET ratio from the blue semicircle (no laser). ACSF refers to artificial cerebral spinal fluid. E) Schematic to illustrate the photo-inactivation of PAR2 without compromising somatostatin receptor 2 (SSTR2) activity. F) PAR2 and SSTR2 activity after

molecular hyperthermia treatment. [AuNP] = 0.32 nM and AuNP incubation time is 5 minutes. Laser conditions: 532 nm wavelength, fluence at 100 mJ/cm^2 and 10 pulses.

3.3.5 Targeting of junctional adhesion molecule-A (JAM-A) by surface modified AuNPs

JAM-A is one of the tight junction proteins that are located between brain endothelial cells,[134] and is an important component of the blood-brain barrier (BBB). Here we test whether targeting and photo-inactivation of JAM-A leads to BBB opening (Figure 3.4A). To target JAM-A, we first modified AuNPs with BV16 (antibody to human JAM-A)[134] and observed similar changes in hydrodynamic size and absorbance peak shift (Figure B8) as with PAR2 antibody conjugation. JAM-A expression was confirmed between cells by immunocytochemistry staining (Figure B9). The immunocytochemistry staining of the AuNP-BV16 group showed a clear signal between cell boundaries while the AuNP-PEG group did not show any obvious signal, confirming antibody binding activity after conjugation to AuNP (Figure 3.4B).

3.3.6 Molecular hyperthermia inactivation of JAM-A.

Next, we investigated MH to photo-inactivate JAM-A and potentially manipulate BBB. First, we showed that the AuNP accumulation and laser irradiation does not affect cell proliferation (Figure 3.4C). To characterize the changes in the BBB, the transendothelial electrical resistance (TEER) was measured (Figure 3.4D-E). With MH, the TEER value dropped to 60% in 30 minutes (AuNP-BV16 group) while no significant drop was observed for AuNP-PEG groups and control groups (without AuNP incubation). Also, with absence of laser irradiation, we did not observe any significant drop in TEER values for all three groups. After 6 hours, the TEER value for the MH group recovers to the original level comparable with the control groups. This is important since it

indicates that MH treatment leads to a reversible BBB opening. The endothelial barrier function was also assessed by measuring the permeability of macromolecules (Figure 3.4F). The results show that the permeability of FITC-labeled dextran increased more than 25 times (molecule weight from 4 kDa to 70 kDa) (Figure 3.4G).

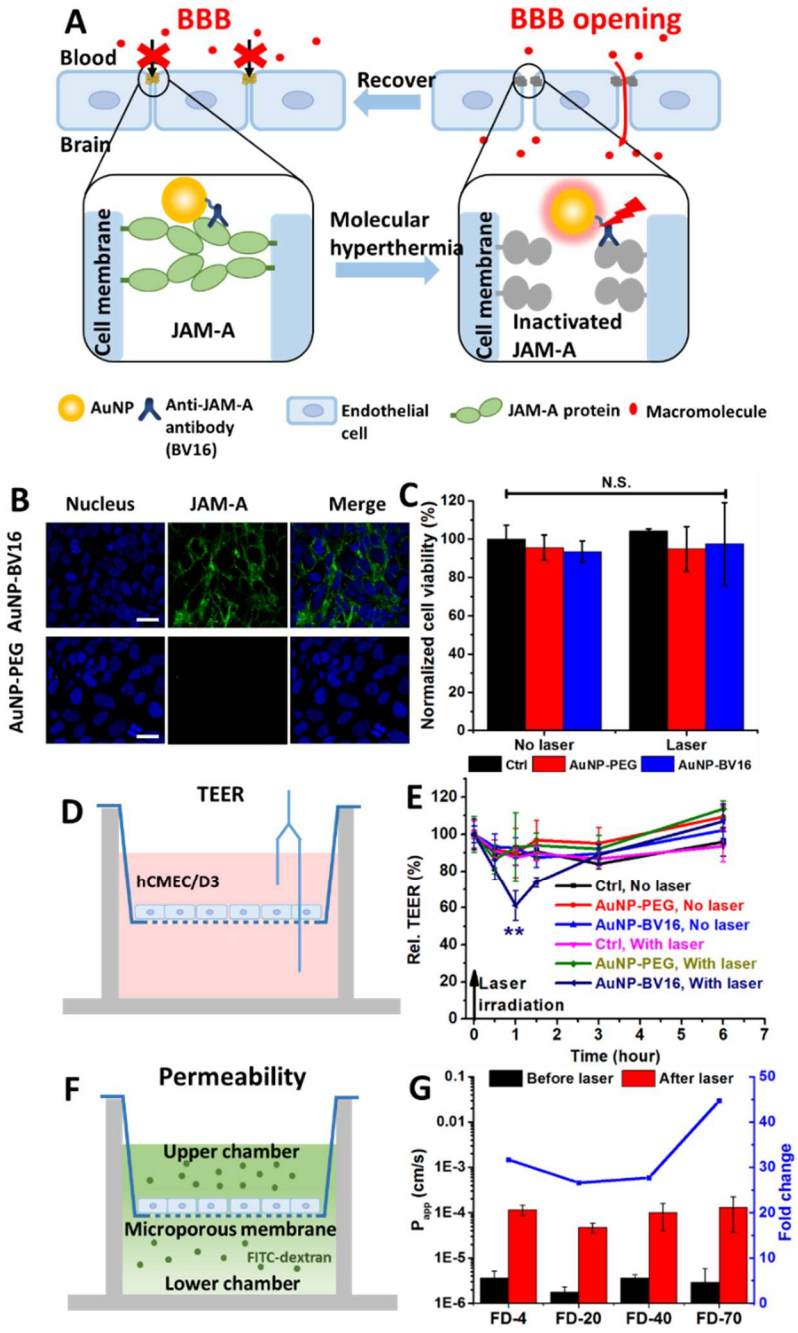

Figure 3.4. Photo-inactivation of a tight junction protein (JAM-A) by molecular hyperthermia to manipulate the blood-brain barrier (BBB). (A) Schematic illustrating the JAM-A photo-inactivation by molecular hyperthermia. (B) Fluorescent immunocytochemistry staining for brain endothelial cells (hCMEC/D3) targeted by AuNP-BV16. Nucleus is in blue and JAM-A is in green (Alexa 488) (scale bar: 20 μm). (C) Cell proliferation measurements with and without laser irradiation and AuNP incubation. Ctrl indicates control group (no AuNP). (D)

Schematic illustrating the transendothelial electrical resistance (TEER) measurement. (E) TEER measurements before and after molecular hyperthermia. (F) Schematic of permeability measurement. (G) Permeability measurements of different sized macromolecules diffusing cross the cellular barrier. FD-4 indicates 4 kDa FITC-labeled dextran.

3.3.7 Comparison of laser fluence for MH and vapor nanobubble generation.

The heating of plasmonic nanoparticles by a pulsed laser can lead to vapor nanobubble formation around the nanoparticle. To determine whether there is vapor nanobubble formation under MH, we measured the AuNP under a pump-probe system that detects the presence of vapor nanobubble scattering. The laser fluence (100 mJ/cm^2) that induces PAR2 inactivation is much lower than the nanobubble generation threshold for 45 nm AuNP (295 mJ/cm^2 for 5% probability and 415 mJ/cm^2 for 50% probability, Figure 3.5A). The nanobubble threshold (835 mJ/cm^2) for 30 nm AuNP is higher than that for 45 nm AuNP. The measured nanobubble threshold agrees with previous study.[153] For comparison, we also included our previous results of photo-inactivation of an enzyme (α-chymotrypsin, α-Cht) by MH induced by 30 nm AuNP (Figure 3.5A).[131] The α-Cht was linked directly to 30 nm AuNP by a PEG linker, and the activity of α-Cht can be monitored directly through an enzyme colorimetric activity assay. Similar to PAR2 inactivation, α-Cht inactivation is dependent on laser fluence. The laser fluences required to induce protein inactivation are lower than the nanobubble generation threshold for 30 nm AuNP (Figure 3.5A). Further comparison shows a large difference in the laser fluence for 50% protein inactivation and nanobubble generation probability (Figure 3.5B). Therefore, we have confirmed that the MH does not lead to nanobubble generation.

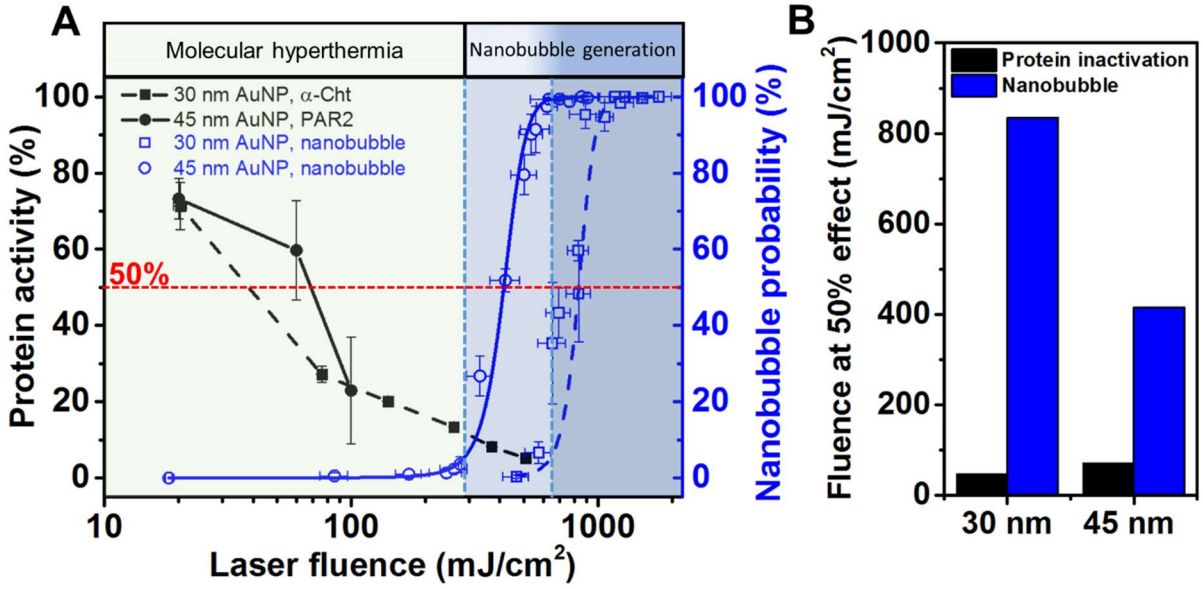

Figure 3.5. Protein inactivation by molecular hyperthermia (MH) does not lead to nanobubble generation. (A) Protein inactivation and nanobubble generation probability as a function of laser fluence. Photo-inactivation of α-chymotrypsin (α-Cht) by 30 nm AuNP (in solution) is adapted with permission from ref [131]. Copyright 2017 John Wiley and Sons. The blue dash and solid lines are Boltzmann fitting for nanobubble probability measurements for 30 and 45 nm AuNP respectively. The blue shaded zone indicates >5% bubble generation probability. (B) Laser fluence at 50% protein inactivation and nanobubble probability.

3.3.8 Estimation of AuNP and surrounding medium heating.

To understand the local temperature change during MH, we simulated the laser plasmonic heating process of AuNP and its surrounding medium. The optical properties of 45 nm AuNP was obtained by Mie theory and the simulation accuracy was confirmed by comparing with experimental measurement (Figure B10A).[22] A nanosecond laser pulse (Full width half maximum, FWHM=6 ns) is applied to the AuNP (Figure B10B). Finite element modeling (FEM) of the 3D temperature profile (at 8 ns, Figure B11A) shows that the particle temperature increases dramatically and the immediate surrounding medium is heated. The heating process by the

nanosecond laser pulse is fast and lasts around 40 ns (Figure B11B). Although the temperature increases of AuNP and surrounding medium is dramatic, the heating area is confined to tens of nanometers from the AuNP surface (Figure B11C). Next, we compared the FEM with molecular dynamics (MD) simulation for a smaller 3 nm AuNP. A small AuNP is modeled here due to the computational limitation of MD (Figure B11D). The gold temperature given by MD is much higher than the FEM result while the water temperature at the interface is lower than the FEM result (Figure B11E&F). This indicates that there may be some size-dependent properties that are not considered in the FEM simulation. Further studies are required to elucidate the temperature changes during MH combining computational and experimental approaches.

3.3.9 Protein manipulation by plasmonic nanoparticles and short laser pulses

In this study, we show that molecule hyperthermia (MH) allows optical switch-off of protein activity in live cells with two distinct examples (PAR2 and JAM-A). First, PAR2 is a G-protein coupled receptor (GPCR) and is implicated in disease conditions such as allergic asthma, cancer, arthritis, and chronic pain.[133, 154] PAR2 can be activated in response to various exogenous and endogenous proteases, usually elevated in inflammation or cancer. Proteolytic cleavage of the N terminus of PAR2 results in exposure of a tethered ligand that activates the receptor to induce signaling. In the periphery nervous system, PAR2 has become an important target to understand and treat diseases such as chronic pain. Second, JAM-A is part of the tight junction protein complex, which is a key component of the blood-brain barrier (BBB). BBB is an important mechanism to protect brain functions from toxins and pathogens in blood circulation. However, it also presents a major challenge and leads to insufficient drug delivery to treat brain diseases.

Optical switch-off of JAM-A by MH causes temporary disruption of BBB and offers a promising way to enhance drug delivery to the brain for a variety of brain diseases including gliomas.

In contrast to photothermal heating that leads to global tissue heating including cancer hyperthermia, optical control neuron firing and optical control of cell behavior with thermally sensitive ion channels, molecular hyperthermia utilizes the thermal confinement enabled by ultrashort nanosecond lasers. Specifically, the nanoscale confined heating of MH operates in a fundamentally different time and spatial scale (10^{-9}s, 10^{-9} m, Figure 1) when compared with global heating (1-100 s, 10^{-3} – 10^{-2} m). Excitation of plasmonic nanoparticles with even shorter laser pulses (picosecond or femtosecond) leads to fundamentally different mechanisms from photothermal effects, and has been explored for optoporation of cells and the release DNA/RNA from AuNP surface.[155, 156]

Nanosecond laser excitation can lead to nanobubble generation at higher laser fluence than MH (Figure 5). Several recent studies have reported using nanosecond laser excitation of membrane-targeted AuNP for optoporation. For example, Xiong *et al.* utilized 2040 mJ/cm^2 (70 nm AuNP, 7 ns laser) to generate nanobubble and efficiently trigger optoporation.[157] Yao *et al.* reported the cell-membrane permeabilization at 400~600 mJ/cm^2 laser fluence (30 nm AuNP, 10^3 NPs/cell, 4 ns laser) for adhesive cells.[158] Comparison of the laser fluence from Yao *et al*. with Figure 5 shows that the laser fluence is close to nanobubble generation threshold and much higher than MH. Therefore, we attribute the protein inactivation by MH to the nanoscale heating while the membrane optoporation by AuNP and nanosecond laser excitation is possibly a result of vapor nanobubble generation.

There are several unanswered questions in this area. First, what is the temperature of the nanoparticle and surrounding water during plasmonic heating of gold nanoparticles? It is not trivial to obtain temperature values of both gold nanoparticles and water directly from experiment. The numerical model in this study used thermal properties of bulk materials and thermal interface conductance measured by femtosecond excitation. The thermal interface conductance on the nanoscale is still an emerging area with many unknowns. The nanoscale thermal properties, including the thermal conductivity of water, are reported to have a recognizable difference from their bulk values.[159] It remains a challenge to develop new methods to reliably predict and validate temperature changes of nanoparticles during short laser excitations (*e.g.* nanosecond pulses). Second, what is the fate of AuNP? There have been some reports on nanosecond pulse induced particle reshaping and fragmentation.[153] It is known that nanosecond laser pulses can lead to nanoparticle reshaping towards a more spherical geometry (for example 20-30 mJ/cm^2 for 40 nm AuNP). The fluence we use in this paper is higher than this value and we anticipate some particle reshaping and even fragmentation. Further investigation will be necessary if it is desirable to avoid particle fragmentation. For example, it may be possible to reduce the chance of particle fragmentation by further stretching the pulse duration to reduce the local temperature and extend the nanoscale heating duration.[160] Third, how does the protein structure react to such intense heating? Previous studies suggest not only changes in the secondary structures of proteins but also in the primary structure.[44-46] However, the mechanism of this protein inactivation phenomenon remains unclear although there have been some molecular dynamics simulations in this area.[161] The fate of the protein under MH needs further investigation. Lastly, how does the protein expression level affect the MH? The exact number of PAR2 and JAM-A expressed on the cell

surface remains to be quantified. An important next step would be to determine the receptor density on the cell membrane and number of AuNP targeted on the membrane. Towards this, MH may be a useful tool for precisely probing and manipulating protein activity at a single-cell level.[162,163] Another question is how the cell reacts to MH in real time. It may be an interesting topic to investigate cellular responses such as intracellular pathways[164, 165] in real time after MH.

3.3.10 Broad applicability of MH

There has been significant interest in the use of plasmonic nanoparticles to control cell behavior.[59, 60, 125] However, most of the techniques require thermally sensitive ion channels such as expressing TRPV-1 in cells, thus limiting their applications. Here MH utilizes the intrinsic properties of nanoscale heating to inactive neighboring proteins, thus allowing broad applications as demonstrated here. Furthermore, MH doesn't require genetic modification and thus removes a barrier as a more general method to optically switch off protein function and control cell behaviors. Furthermore, MH utilizes plasmonic nanoparticles that can be engineered to strongly absorb in the near-infrared window for *in vivo* applications such as using gold nanorods[166-168] or nanoshells.[92] This is a significant advantage compared with other approaches such as CALI and synthetic photoswitches where few photosensitizers and photoswitches work in the near-infrared window.

3.3.11 Intracellular proteins as targets

The two proteins in this work are both located on cell surfaces for ease of targeting. GPCRs are a class of the most important transmembrane proteins that transfer extracellular messages to intracellular signaling. More than 40% of all modern drugs and almost 25% of the top 200 best-selling drugs target GPCRs.[169] While the importance of membrane proteins can't be overstated,

there are potential methods to deliver nanoparticles to target intracellular proteins. For example, one study suggests that hydrophobic surface modification of silicon nanoparticle conjugates enhances intracellular protein delivery to target intracellular protein machinery.[170] In addition, it is possible to use other targeting methods besides antibodies as was used in this report. In particular, antibodies may have limited applicability for intracellular targets due to their large size, complex structures and disulfide bonds.[171] Some promising methods utilize relatively smaller molecules such as aptamers[172] and nanobodies[173] to provide more flexibility for intracellular protein targeting. Also, the majority of therapeutics utilize small molecules due to their small size and amphiphilic properties. Thus, an alternative is to use a small molecule as a target ligand instead of using antibodies to achieve intracellular MH.[174]

3.4 Conclusions

In this study, we demonstrate that molecular hyperthermia (MH) allows us to optically switch off protein activity in live cells without genetic modification. MH is based on the nanoscale plasmonic heating of AuNPs to inactivate targeted proteins of interest. To demonstrate the broad applicability of MH, we show that MH can inactivate protease activated receptor-2 (PAR2), a G-protein coupled receptor implicated in pain, and junctional adhesion molecule A (JAM-A), one of the tight junction proteins in the blood-brain barrier. In both cases, the photo-inactivation of the target protein did not compromise cell proliferation. Furthermore, the laser fluence used for MH is not sufficient to generate vapor nanobubble around AuNPs. MH is a promising method with broad applicability to switch off protein activity without genetic modification and will find many applications in biomedical sciences.

CHAPTER 4

COMPUTATIONAL INVESTIGATION OF PROTEIN PHOTOINACTIVATION BY MOLECULAR HYPERTHERMIA

This chapter has been submitted to Journal of Biomechanical Engineering: Kang, P.;† Xie, C.;† Fall, O.; Randrianalisoa, J.; Qin, Z., Computational investigation of protein photoinactivation by molecular hyperthermia. J. Biomech. Eng. 2020, in submission.

4.1 Introduction

Using light to selectively and remotely control biological functions of living systems is a long-pursed objective in biomedical science.[175] Various approaches have been developed during the last decade, such as optogenetics[176] and synthetic photoswitches.[53, 117] Optogenetics utilizes photosensitive molecules to genetically modify the protein of interest and enables light manipulation of targeted cells. This revolutionary technique helps us understand how specific cell type contributes to complex neural circuits and brain functions. While optogenetics is undoubtedly powerful, the requirement of genetic modification still limits its clinical and translational value for human. Another emerging approach to control protein activity with light is by synthetic photoswitches. However, there are limited numbers of photoswitches (mostly based on azobenzene) available, thus narrow options of wavelength window. To overcome these drawbacks, nanoparticles provide promising opportunities in this area.[50, 155, 177, 178] One good candidate is the plasmonic nanoparticle that strongly interacts with light.[179] Upon light irradiation, plasmonic nanoparticles convert electromagnetic wave energy into thermal energy and heat up surrounding medium, known as plasmonic heating.[30, 136] Due to plasmonic heating, plasmonic nanoparticles have been used to optically control tissue and cellular behaviors, including photothermal therapy of tumor treatment[31], neuron firing,[60, 180, 181] heat shock protein expression[68] and optoporation.[35, 129]

The plasmonic heating process can be engineered on different time and length scales by controlling the light energy input.[99, 182] This is because the heat diffusion is highly related to time. When the energy input has a long duration and allows heat dissipation away from the particle, the plasmonic heating can lead to a global temperature rise in a large scale (Figure 4.1). This far-field

plasmonic heating effect is used in various biomedical applications, such as thermal therapy or hyperthermia. To achieve a tissue heating for cancer treatment, long duration or continuous light irradiation, i.e. seconds to minutes, is required.[183] On the other hand, near-field plasmonic heating can be achieved by applying an intense energy input with a duration shorter than diffusion or relaxation time of the irradiated volume. In this scenario, the heat does not have enough time to dissipate away, and hence causes a highly localized heating, known as thermal confinement. The dissipated heat is insufficient to cause a global heating. Depending on the laser pulse duration, the localized heating area can be in the nanoscale (Figure 4.1). The nanoscale plasmonic heating provides new approaches to trigger cellular or even subcellular thermal responses with ultrashort laser pulses.[41, 42, 44, 99]

Recently, by taking advantage of nanoscale plasmonic heating, we developed a method called molecular hyperthermia (MH) to photoinactivate protein activity.[131, 184] MH utilizes ultrashort laser pulses (nanosecond) to excite a plasmonic nanoparticle (AuNP) as a nanoheater to thermally inactivate proteins adjacent to the nanoparticle. MH selectively inactivates enzymes targeted by AuNP and leaves untargeted enzymes intact, demonstrating the spatial selectivity of MH.[131, 160] We further showed that MH can be used to inactivate cell membrane proteins in live cells without compromising cell viability.[184] MH is a promising method to selectively and remotely manipulate protein activity and cellular behavior. However, MH is a complicated process, and involves not only heat transfer but also temperature-dependent chemical reactions (thermal inactivation of proteins). So far, most models of nanoparticle plasmonic heating focus only on heat transfer process.[42, 77, 185] To better understand the MH, a numerical model would allow us to quantitatively describe protein inactivation induced by ultrashort laser plasmonic heating.

In this work, we developed a numerical model that can quantitatively describe the near-field heating and protein inactivation during MH. With this model, we further investigated the important parameters for MH, such as laser pulse shape, temperature-dependence of material properties, and particle shape. This work provides a better understanding of the protein inactivation response to the near-field plasmonic heating, and design guidelines for biomedical applications of MH.

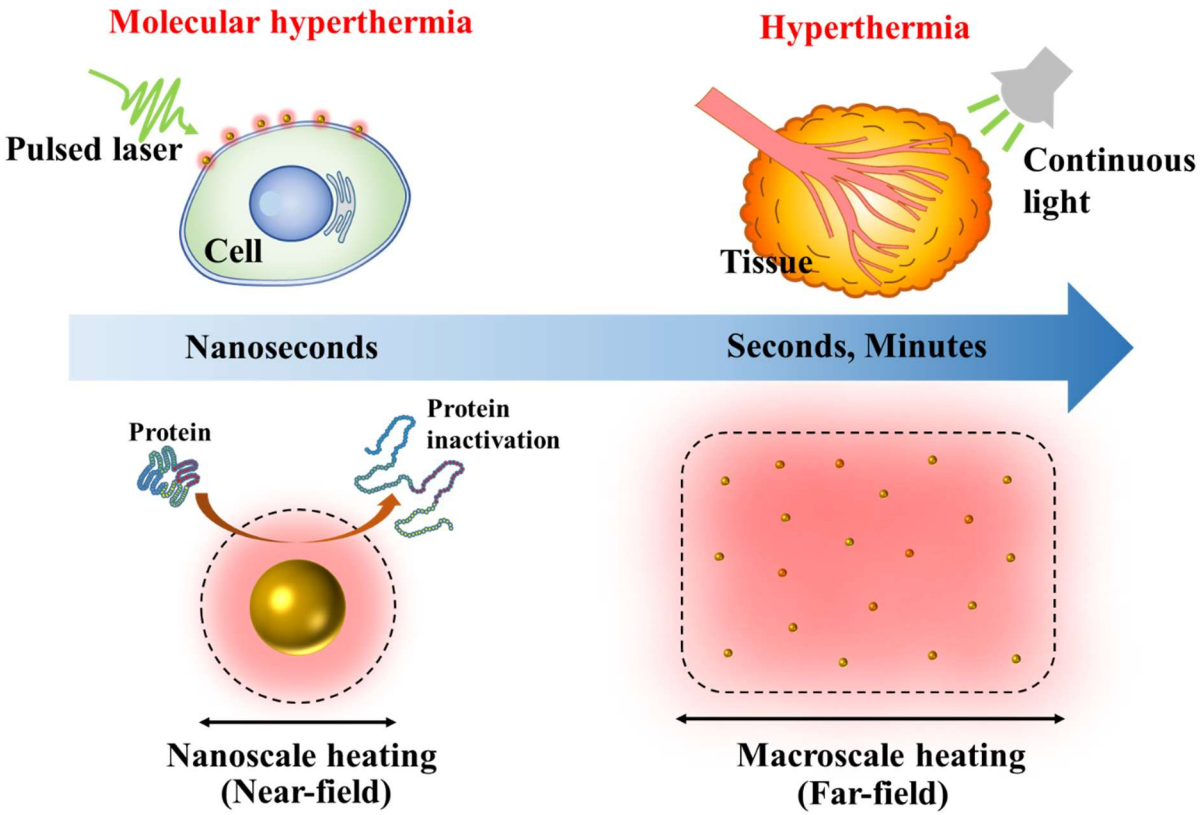

Figure 4.1. Comparison between molecular hyperthermia and hyperthermia. Molecular hyperthermia utilizes short laser pulse (nanoseconds) to generate nanoscale heating (near-field) and inactivate proteins without killing cells. On the other hand, hyperthermia uses macroscale heating (far-field) of plasmonic nanoparticles induced by continuous irradiation (seconds to minutes) to kill tumor tissue.

4.2 Method

4.2.1 Analytical solution for single particle heating

The analytical solution of spherical nanoparticle heat transfer is used as a benchmark for numerical solution. The model is a spherical nanoparticle as a heat source immersed in water. The heat generation is homogeneous inside the nanoparticle and two-temperature effect is negligible in this study. The reason is that the electron-electron interaction time (femtoseconds) and electron-phonon thermalization time (picoseconds) are very short compared with laser pulse duration (nanoseconds).[29] In the analytical solution, we neglect the interfacial thermal resistance, and we discuss its effect in numerical solution. The single particle heat conduction model in spherical system was analytically solved by Laplace transformation.[186] The governing equations, boundary and initial conditions were listed in Table 4.1:

Table 4.1. Heat transfer governing equations, boundary and initial conditions.

$\frac{1}{\alpha_{Au}}\frac{\partial T_{Au}}{\partial t}=\frac{1}{r^2}\frac{\partial}{\partial r}\left(r^2\frac{\partial T_{Au}}{\partial r}\right)+\frac{Q_v}{k_{Au}}$	(4.1)
$\frac{1}{\alpha_{water}}\frac{\partial T_{water}}{\partial t}=\frac{1}{r^2}\frac{\partial}{\partial r}\left(r^2\frac{\partial T_{water}}{\partial r}\right)$	(4.2)
$-k_{Au}\left.\frac{\partial T_{Au}}{\partial r}\right\|_{r=R_{NP}}=-k_{water}\left.\frac{\partial T_{water}}{\partial r}\right\|_{r=R_{NP}}$	(4.3)
$T_{Au}\|_{r=R_{NP}}=T_{water}\|_{r=R_{NP}}$	(4.4)
$\left.\frac{\partial T}{\partial r}\right\|_{r=0}=0$	(4.5)
$T\|_{r=\infty}=T_{ref}=300\ K$	(4.6)
$T\|_{t=0}=T_{ref}=300\ K$	(4.7)

Table 4.1. continued

$Q_v = \frac{C_{abs}F}{V_{NP}t_0}[u(t) - u(t-2\mu)]$	(4.8)

The analytical solution for this heat transfer model is listed in Table 4.2. The analytical solution was calculated in Matlab 2016b software.

Table 4.2. Analytical solution of single nanoparticle heated by rectangular pulse.

Heating process	$T_{Au}(r,t)\|_{t<2\mu} = T_{ref} + \frac{{R_{NP}}^2}{k_{Au}}\frac{C_{abs}F}{V_{NP}2\mu}\left\{\frac{1}{3}\frac{k_{Au}}{k_{water}} + \frac{1}{6}\left(1 - \frac{r^2}{{R_{NP}}^2}\right) - \frac{2R_{NP}b}{r\pi}\int_0^{\infty}\frac{\exp\left(-{y^2t}/{\gamma_1}\right)}{y^2}\frac{(\sin y - y\cos y)\sin({ry}/{R_{NP}})}{[(c\sin y - y\cos y)^2 + b^2y^2sin^2y]}dy\right\}$	(4.9)
	$T_{Au}(r=0,t)\|_{t<2\mu} = T_{ref} + \frac{{R_{NP}}^2}{k_{Au}}\frac{C_{abs}F}{V_{NP}2\mu}\left\{\frac{1}{3}\frac{k_{Au}}{k_{water}} + \frac{1}{6} - \frac{2b}{\pi} * \int_0^{\infty}\frac{\exp\left(-{y^2t}/{\gamma_1}\right)}{y^2}\frac{(\sin y - y\cos y)}{[(c\sin y - y\cos y)^2 + b^2y^2sin^2y]}dy\right\}$	(4.10)

Table 4.2. continued

	$T_{water}(r,t)\|_{t<2\mu}$ $= T_{ref} + \frac{{R_{NP}}^3}{rk_{Au}}\frac{C_{abs}F}{V_{NP}2\mu}$ $*\left\{\begin{array}{c}\frac{1}{3}\frac{k_{Au}}{k_{water}} - \frac{2}{\pi}\int_0^{\infty}(\frac{\exp\left(-{y^2t}/{\gamma_1}\right)}{y^3} \\ *\frac{(\sin y - y\cos y)[by\sin y\cos\sigma y - (c\sin y - y\cos y)\sin\sigma y]}{[(c\sin y - y\cos y)^2 + b^2y^2sin^2y]}) \\ dy\end{array}\right\}$	(4.11)
Cooling process	$T_{Au}(r,t)\|_{t\geq 2\mu} = T_{ref} + \frac{2{R_{NP}}^3 b}{r\pi k_{Au}}\frac{C_{abs}F}{V_{NP}2\mu}$ $*\int_0^{\infty}\frac{\exp\left[-{y^2(t-2\mu)}/{\gamma_1}\right] - \exp\left({y^2t}/{\gamma_1}\right)}{y^2}$ $*\frac{(\sin y - y\cos y)\sin({ry}/{R_{NP}})}{[(c\sin y - y\cos y)^2 + b^2y^2sin^2y]}dy$	(4.12)
	$T_{Au}(r=0,t)\|_{t\geq 2\mu}$ $= T_{ref} + \frac{2{R_{NP}}^2 b}{\pi k_{Au}}\frac{C_{abs}F}{V_{NP}2\mu}$ $*\int_0^{\infty}\frac{\exp\left[-{y^2(t-2\mu)}/{\gamma_1}\right] - \exp\left({y^2t}/{\gamma_1}\right)}{y^2}$ $*\frac{(\sin y - y\cos y)}{[(c\sin y - y\cos y)^2 + b^2y^2sin^2y]}dy$	(4.13)

Table 4.2. continued

	$T_{water}(r,t)\|_{t\geq 2\mu}$ $= T_{ref} + \frac{{R_{NP}}^3}{r k_{Au}} \frac{C_{abs}F}{V_{NP} 2\mu}$ $* \left\{ \frac{1}{3}\frac{k_{Au}}{k_{water}} - \frac{2}{\pi} * \int_0^{\infty} \frac{\exp\left[-y^2(t-2\mu)/\gamma_1\right] - \exp\left(y^2 t/\gamma_1\right)}{y^3} * \frac{(\sin y - y\cos y)[by \sin y \cos \sigma y - (c \sin y - y \cos y)\sin \sigma y]}{[(c \sin y - y\cos y)^2 + b^2 y^2 sin^2 y]} dy \right\}$	(4.14)
	$b = \frac{k_{water}}{k_{gold}} \sqrt{\frac{\alpha_{Au}}{\alpha_{water}}}, c = 1 - \frac{k_{water}}{k_{gold}}, \gamma_1 = \frac{{R_{NP}}^2}{k_{gold}}, \sigma = \left(\frac{r}{R_{NP}} - 1\right)\sqrt{\frac{k_{gold}}{k_{water}}}$	(4.15)

4.2.2 Finite element simulation

All finite element simulations were conducted in COMSOL 5.3 software. The governing equations, boundary and initial conditions are same as Table 4.1. The thermal interfacial resistance was described as the following equation:

$$-k_{Au}\frac{\partial T_{Au}}{\partial r}\bigg|_{r=R_{NP}} = -k_{water}\frac{\partial T_{water}}{\partial r}\bigg|_{r=R_{NP}} = \frac{1}{R}\,(T_{Au} - T_{water})|_{r=R_{NP}} \tag{4.16}$$

The volumetric heat generation by Gaussian pulse was defined as:

$$Q_v = \frac{C_{abs}F}{V_{NP}}\frac{3}{\mu\sqrt{2\pi}} e^{-\frac{5.546(t-\mu)^2}{1.232\mu^2}} \tag{4.17}$$

4.2.3 Protein inactivation calculated by Arrhenius model

We assume protein inactivation is a two-state, first-order kinetic model with native (N) and inactivated (I) state:

$$N \xrightarrow{k(T)} I \tag{4.18}$$

The temperature-dependence of reaction rate can be described by Arrhenius model:

$$k(T) = A_0 e^{-\frac{E_a}{RT}} \tag{4.19}$$

And the inactivation of protein can be estimated by the following equation:

$$s(r) = e^{-\int k(T)dt} \tag{4.20}$$

In this study, we selected α-chymotrypsin as our model protein since our previous experiments demonstrated the feasibility of α-chymotrypsin photoinactivation by MH.[131] The prefactor (A_0) of protein inactivation is 9.75×10^{38} s^{-1} and activation energy is 244.05 kJ mol^{-1} for α-chymotrypsin.[99]

4.2.4 Temperature-dependence of material properties

The material properties used in numerical and analytical solution are shown in Table 4.3.

Table 4.3. Temperature-dependence of material properties

Parameters	Expression	Temperature-dependent value (ref. 187)	Constant (ref. 187)
Specific heat of gold	C_{Au} [J kg^{-1} K^{-1}]	$399352.2\cdot T^{-2}+114.8987+0.032288\cdot T$	129

Table 4.3. continued

Specific heat of water	C_{water} [J kg^{-1} K^{-1}]	$12010.147-80.407\cdot T+0.310\cdot T^2-5.382\times10^{-4}\cdot T^3+3.625\times10^{-7}\cdot T^4$	4200
Thermal conductivity of gold	k_{Au} [W m^{-1} K^{-1})]	$330.6431-0.02537\cdot T-8.19\times10^{-5}\cdot T^2+6.79\times10^{-8}\cdot T^3-2.15\times10^{-11}\cdot T^4$	317
Thermal conductivity of water	k_{water} [W m^{-1} K^{-1})]	$-0.869+0.009\cdot T-1.583\times10^{-5}\cdot T^2+7.975\times10^{-9}\cdot T^3$	0.6
Gold density	ρ_{Au} [kg m^{-3}]	$19501.44+1.401\cdot T-0.003\cdot T^2+3.718\times10^{-7}\cdot T^3$	19300
Water density	ρ_{water} [kg m^{-3}]	$838.466-0.69338\cdot T-2.04\times10^{-4}\cdot T^2+4.30\times^{-8}\cdot T^3$	998

4.3 Results

4.3.1 Numerical model validation

Firstly, we confirmed the accuracy of the numerical model by comparing the numerical solution with the analytical solution. Figure 4.1A-B illustrates the geometry and laser profile for the model. An AuNP with diameter of 30 nm (D_{NP} = 30 nm) is in the center of a spherical water domain. The size of water domain is 300 nm (D_{water} = 300, Figure 4.2A). The temperature of the water domain boundary is set to 300 K (first-type boundary condition). For analytical solution, the AuNP is immersed in an infinite domain of water, which initial temperature is 300K. The single

rectangular pulsed laser (10 ns, laser intensity is 25.4 GW/m^2) is used to heat the AuNP (Figure 4.2B). Temperature profiles at three different positions from numerical simulation are compared with analytical solution (Figure 4.2C). For both cases, the temperature rises quickly and returns to initial temperature (300 K) after 40 ns. This result demonstrates that the simulation time (50 ns) is sufficient for single particle to cool down. We also compared the numerical and analytical solution of temperature distribution at three different time points (Figure 4.2D). Because the thermal conductivity of gold is significantly larger than water, the temperature distribution in AuNP is nearly uniform. The temperature difference between numerical solution and analytical solution is negligible. This suggests that the water domain is large enough, and the first-type boundary condition is satisfactory for this numerical simulation. The MH induced protein inactivation is calculated by the Arrhenius model. We assume that the protein distribution is homogeneous around the AuNPs. The protein inactivation profile was calculated along the radial direction after single pulse irradiation at 50 ns (Figure 4.2E). The inactivation of proteins is localized around the AuNP and the border of inactivation zone is quite sharp. We define the impact zone as the distance from particle surface to where 50% of protein stay intact (illustrated by pink color in Figure 4.2E). Both numerical and analytical solutions give the same impact zone (~10.5 nm, Figure 4.2F). These results confirm the accuracy of the numerical method.

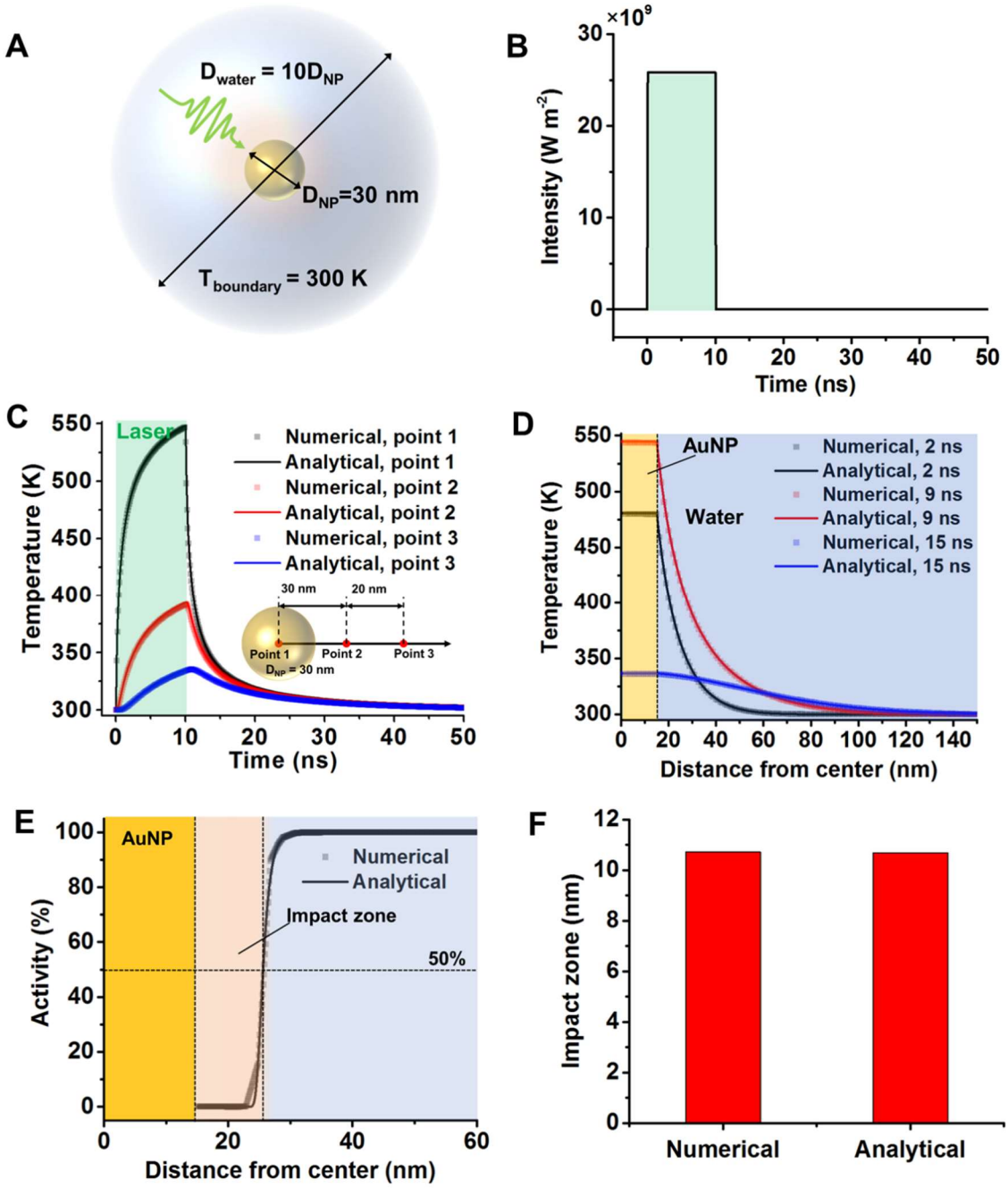

Figure 4.2. Numerical model validation. (A) The model geometry of numerical simulation. D_{NP} is diameter of AuNP. D_{water} is diameter of water domain and is set to be 10 D_{NP}. (B) Rectangular laser intensity profile in both numerical and analytical solutions. (C) Temperature profile of three different positions (illustrated by insert picture) by numerical and analytical solutions. (D) Temperature distribution of three different time points by numerical and analytical solutions. (E)

Protein inactivation profile in the radial direction after laser irradiation. (F) Impact zone predicted by the numerical method and analytical method.

4.3.2 Effects of pulse shape and duration

Secondly, we investigated the effect of pulse shape and pulse duration on MH. Here, we compared two pulse shapes, *i.e.* rectangular and Gaussian (bell). Also, we compared different durations of the Gaussian pulses. All laser pulses share the same fluence (254 J/m^2, illustrated by shaded areas, Figure 4.3A). All Gaussian pulses start at 0 ns time point, and their peak position varies from 5 ns to 20 ns depending on the pulse durations. Figure 4.3B shows that the temperature response of AuNP varies according to pulse shapes and durations. The peak temperature of AuNP decreases when the pulse duration is stretched. For the rectangular shape pulse, the peak temperature of AuNP appears at the end of the pulse (10 ns). The protein activity distribution was then calculated based on the temperature profile (Figure 4.3C). Although all the pulse energy inputs are same, pulses with longer duration inactivate less proteins than pulses with shorter duration. This is due to the nonlinear temperature-dependence of protein inactivation in the Arrhenius model. Pulses with shorter duration generates more intense heat response and accelerates protein inactivation. Interestingly, the impact zone of rectangular pulse is same as the Gaussian pulse which peak position is at 10 ns (μ = 10 ns, Figure 4.3D).

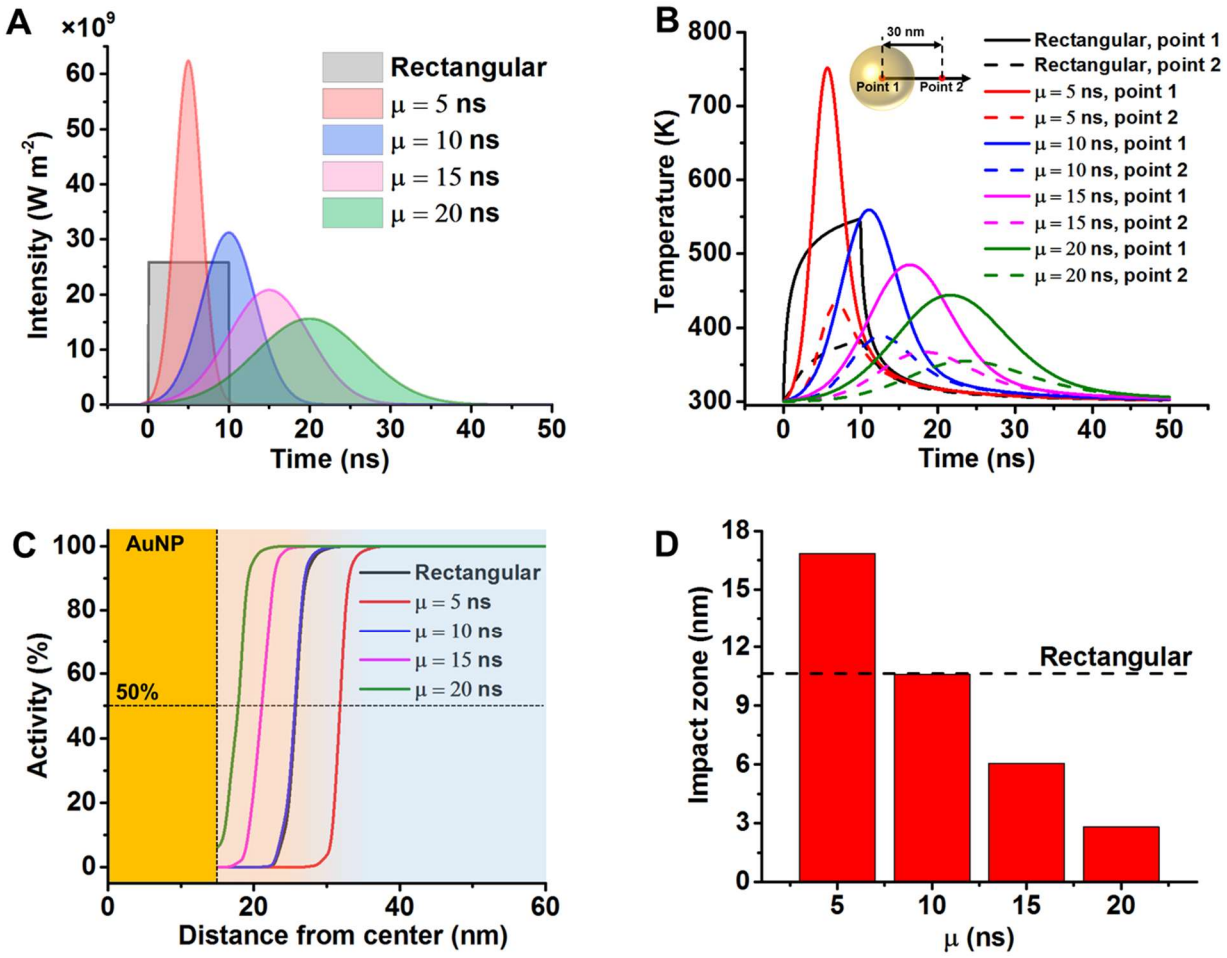

Figure 4.3. Effect of laser pulse shape and duration on molecular hyperthermia. (A) The laser profiles with different shapes (Gaussian versus rectangular) and different pulse durations. μ is the center of Gaussian pulse. All laser pulses share the same laser fluence (254 J/m^2). (B) Temperature profile of gold nanoparticle for different pulses. (C) Protein activity distribution after different laser pulse. (D) Effect of pulse duration on the impact zone. The dash line indicates impact zone of 10 ns rectangular pulse.

4.3.3 Effect of temperature-dependent material properties

Thirdly, we studied the effect of temperature-dependent material properties (k, C_p and ρ in water and AuNP) on the near-field heating and protein inactivation. Figure 4.4A shows that no obvious difference was observed for temperature-dependent density and specific heat. However,

the temperature-dependent thermal conductivity significantly decreases the temperature profiles in both gold and water. Consequently, the impact zone decreases 1.4 nm when compared with the case with constant properties (Figure 4.4B). If we consider the temperature-dependences for all material properties (labeled as [k, ρ, C_p] (T)), the result is the same as the temperature-dependent thermal conductivity (labeled as k(T)). These results demonstrate that the temperature-dependent thermal conductivity has a significant effect on MH.

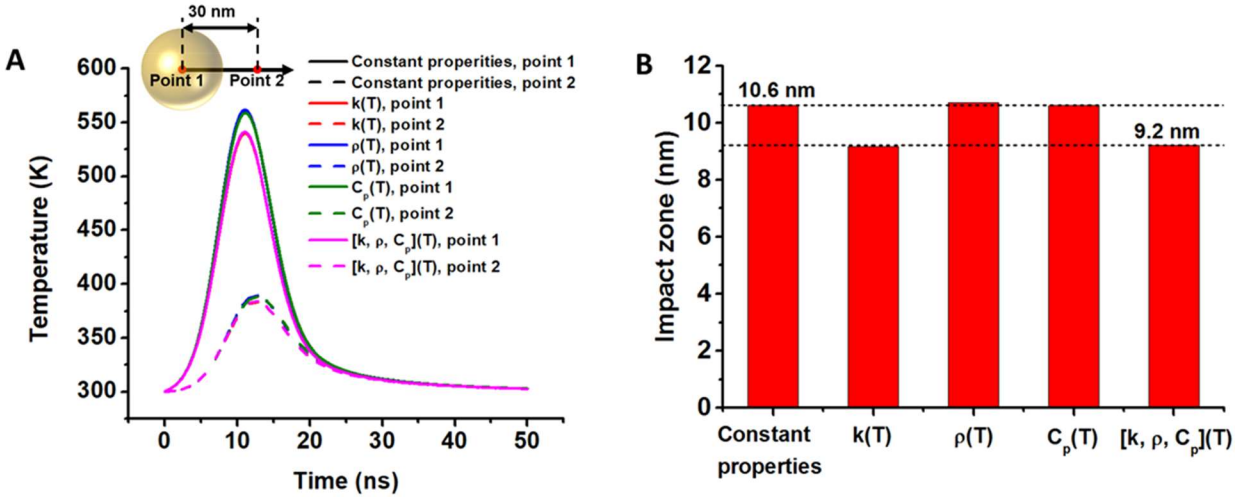

Figure 4.4. Effect of temperature-dependent material properties. (A) Comparison of temperature profile in different points for constant and temperature-dependent material properties. (B) Comparison of impact zones for constant and temperature-dependent material properties.

4.3.4 Effect of thermal interfacial resistance

Next, we studied the effect of thermal interfacial resistance (or Kapitza resistance, R_K) at gold-water interface on MH. R_K originates from the mismatch of phonon transport at the gold-water interface, which can be significantly tuned by surface chemical modifications (Figure 4.5A). In MH, the surface of AuNP is modified with polyethylene glycol (PEG) and antibodies. Thus, it is important to estimate the effect of R_K on MH in a wide range. In this study, a large range of R_K

(1×10^{-10} K m^2 W^{-1} to 1×10^{-7} K m^2 W^{-1}) was investigated to cover data reported previously (Table 4.4). Figure 4.5B shows that R_k increases the temperature in the AuNP significantly. In contrary, water temperature doesn't change with R_K significantly. The water temperature has a slight drop only when R_K is larger than 1×10^{-8} Km^2/W (Figure 4.5B). There is a small drop in water temperature due to the heat flux decrease through the gold-water interface (Figure 4.5C). Consequently, the impact zone is smaller when R_K exceeds 1×10^{-8} K m^2 W^{-1}(Figure 4.5D). However, when comparing our results with the R_K values reported by previous studies (marked by blue shade), the thermal interfacial resistance has a negligible effect on MH.

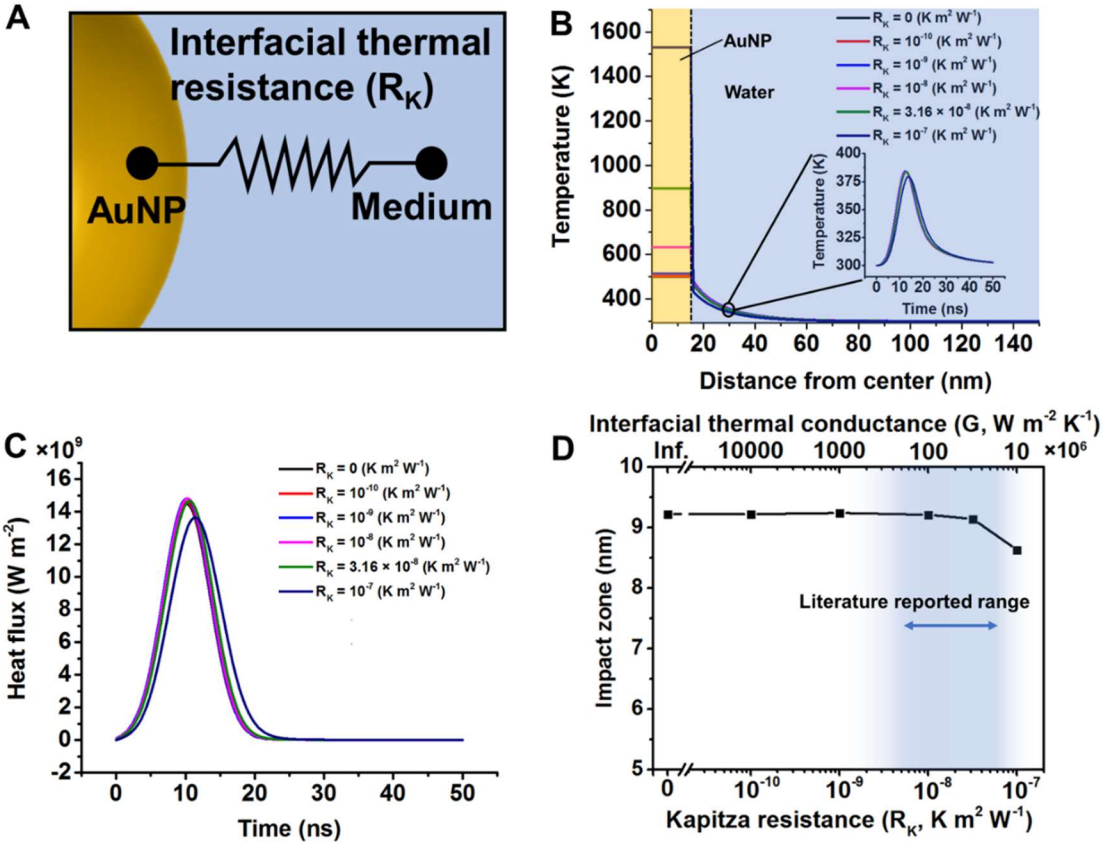

Figure 4.5. Effect of thermal interfacial resistance between gold and water. (A) Schematic of the interfacial resistance between AuNP and water. (B) Temperature profile for different Kapitza resistances at t = 9 ns. Insert figures shows the temperature profile of water at 30 nm from the

nanoparticle center. (C) Heat flux at the gold-water interface for different Kapitza resistance. (D) Impact zone for different Kapitza resistances. The interfacial thermal conductance (G) is the reciprocal of Kapitza resistance.

Table 4.4. Summary of interfacial thermal resistance of nanostructures

Material	Nano-structure	Solvent	Interfacial modification	Kapitza resistance (R_K, $\times 10^{-8}$ K m^{-2} W^{-1})	Methods	Ref.
Pt	Nanoparticle	Water	No	1.61	DMM	188
		Toluene	Citrate	0.77	TA	
AuPt	Nanoparticle, 10 nm	Toluene	Alkanethiol	20		
	Nanoparticle, 3-5 nm	Water/alcohol	Tiopronin	0.50~1.11		189
		Water/alcohol	Thioalkylated ethylene glycol	0.29~0.63		
Au-core/Au Pt-shell	Nanoparticle, 22nm	Water/alcohol	CTAB	0.36~0.56		
Al	Flat surface	Water	PEG-silane	0.48~0.67	TDTR	190
	Flat surface	Water	OTS	1.54~1.82		
Au	Nanoparticle	Toluene	No	8.33	DMM	188
		Water	Citrate	0.83~1.11	SAXS	142
	Flat surface	Water	C_{18}	1.82~2.22	TDTR	190
			$C_{11}OH$	0.83~1.25		
	Nanorod	Water	CTAB	0.22~0.77	TA	191
			PEG-COOH	~0 (underestimated)		
	Nanoparticle	Toluene	No	1~2	LJ model	192
		Water		0.59~0.67		
	Flat surface	No	Dodecyltriethoxysilane	2.78	TDTR	193
			11-mercapto-undecyltrimethoxysilane	1.54		
			11-amino-undecyltriethoxysilane	2.12		

Table 4.4. continued

			11-bromo-undecyltrimethoxysilane	2.56		
			Dodecyl-dimethyl-monochlorosilane	2.94		
	Nanorod	Methanol	CTAB	2.5~3.13	TA	194
		Ethanol		2.63~3.85		
		Toluene		2.86~4		
		Hexane		3.45~4.76		
	Flat surface	Water	n-undecanethiol (n=11~18)	1.43~1.67	TDTR	195
			Methyl 3-mercaptopropionate	0.65~0.8		
			11-(1H-pyrrol-1-yl) undecane-1-thiol	0.65~0.8		
			11-Mercapto-1-undecanol	0.45~0.63		
			11-Mercapto-undecanoic acid	0.45~0.63		
	Nanorod	Water	CTAB	1.2	TA	196
			PEG	0.44		
	Flat surface	Hexylamine	SAMs	0.48~1.82	EMD	197
Carbon	Nanotube	D_2O	Polystyrene sulphonate surfactant	8.33	TA	198

4.3.5 Effects of nanoparticle shape: nanosphere versus nanorods

Lastly, we investigated the effect of nanoparticle shape on MH. Gold nanorod (AuNR) is another type of nanoparticles that commonly used in biomedical related area. Biological tissue

significantly absorbs and scatters visible light, and is more transparent to near infrared light. AuNRs response to light in near-infrared range and offer better light penetration depth for biological tissue. To estimate the AuNR performance for MH, AuNRs with different aspect ratio are studied here (Figure 4.6A). We keep two factors the same for all particles: particle volume (V_{NP}) and volumetric heating rate (Q_v). These conditions ensure the same amount of heat is generated among nanoparticles with different shapes. The results suggest that gold nanosphere (AuNS) has the highest temperature increase and nanoparticle temperature decreases with the aspect ratio (Figure 4.6B&D-E). Compared with AuNS, AuNR has higher surface area and therefore enhances the heat dissipation to the surrounding medium, resulting in a lower nanoparticle temperature.

We further investigated the protein inactivation for different shapes of gold nanoparticles (Figure 4.6C&F-G). The impact zone in the axial direction (z-direction) decreases with higher aspect ratio. It is interesting that the impact zone in the radial direction (r-direction) firstly increases for nanorod with aspect ratio of 2 compared with spherical particle, but then decreases with aspect ratio from 2 to 6 (Figure 4.6F). The impact zone in the r-direction reaches maximum value when aspect ratio is around 1.75. We further compared the impact volume for particle with different shapes, which is defined as the volume where proteins are inactivated by the near-field heating. The impact volume decreases with increasing aspect ratio for AuNRs as a result of higher surface-to-volume ratio and heat dissipation rate than spherical nanoparticle (Figure 4.6G). It is worth noting that we only considered constant volumetric heating generation in these comparisons. AuNRs have two plasmonic peak, corresponding to localized surface plasmon resonance (LSPR) from longitudinal and transverse modes. By adjusting the aspect ratio of AuNRs from 2 to 6, the

longitudinal peak can be tuned from 600 nm to more than 1000 nm. Also, the longitudinal peak absorption is significantly higher than transverse peak (Figure C1). Thus, by applying laser at longitudinal peak, AuNR would generate more heat than AuNS.

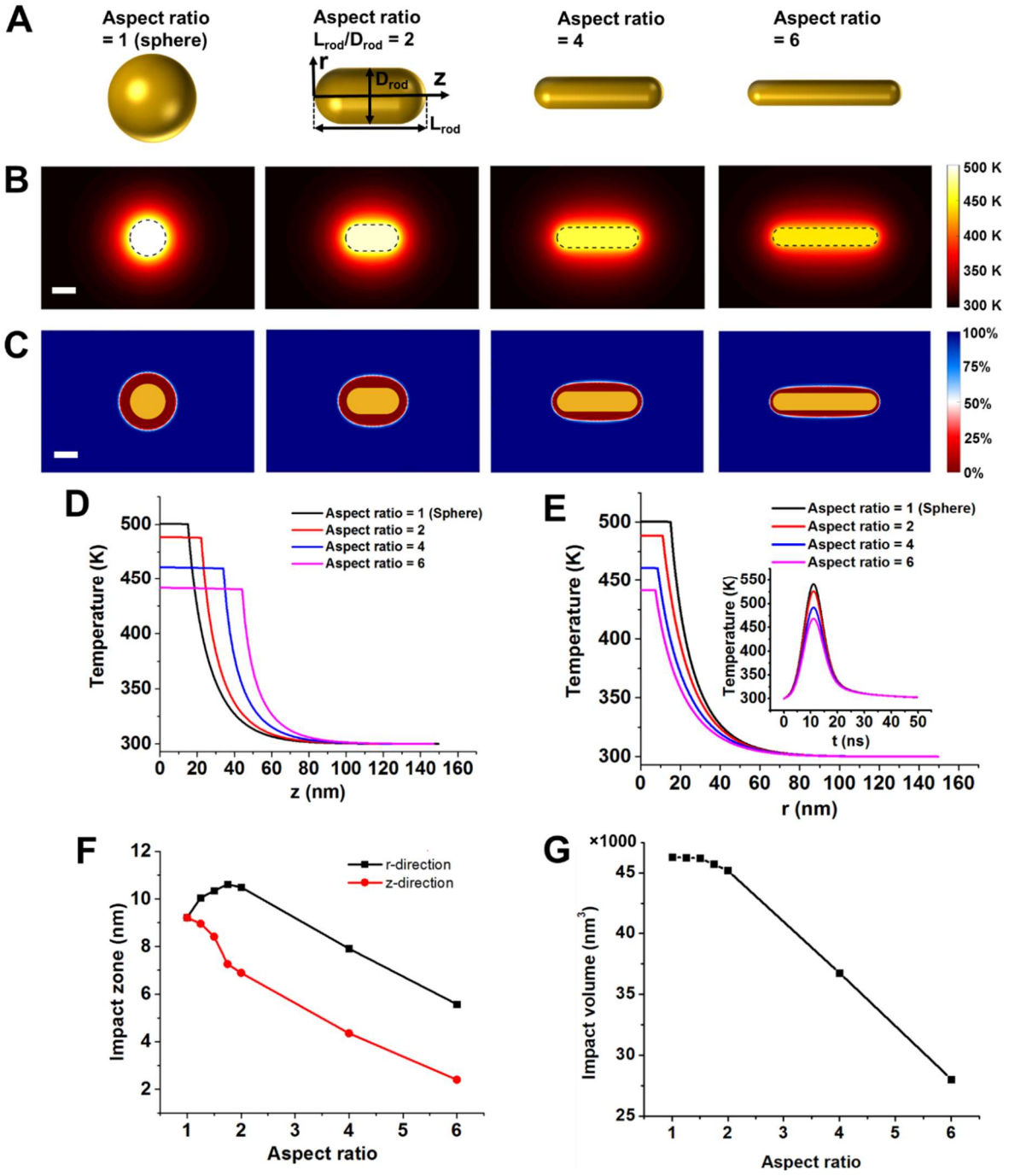

Figure 4.6. Effect of particle shape on molecular hyperthermia. (A) Different shapes of gold nanoparticles. Aspect ratio is defined as the ratio between length and radius of rod. All particles have the same volume. (B) Temperature distribution around gold nanoparticles with different aspect ratios. (C) Protein activity distribution around gold nanoparticle. 100% indicates all proteins are intact and 0% indicates all proteins are inactivated, the boundary of impact zone (50%) is

shown in white color. (D) Temperature distribution in the axial direction for gold nanoparticles with different shapes. (E) Temperature distribution in the radial direction for gold nanoparticles with different shapes. Insert is gold temperature profile as a function of time. (F) Impact zone changes with aspect ratio in the axial and radial directions. (G) Impact volume for gold nanosphere and nanorods with different aspect ratios.

4.4 Discussion

In this study, we built a computational model to study the protein inactivation behavior during MH. We studied important factors that affect the protein inactivation in MH including laser shape, duration, temperature-dependent material properties, thermal interfacial resistance, and nanoparticle shape. The results provide a guideline in designing and applying MH for various biomedical applications. There are several interesting aspects that have emerged from our studies.

4.4.1 Material properties in the nanoscale

The material properties utilized here are all obtained from bulk materials. However, the physical properties of material may vary in the nanoscale. For example, the melting temperature of AuNP drops significantly compared with bulk gold when the particle size is smaller than 10 nm [199]. Since we use 30 nm AuNP in our study, the melting point of particles in our study can be considered the same as bulk gold (1337K). Also, we limited our laser energy to ensure the nanoparticle temperature below gold melting point. Therefore, we didn't consider the phase change effects in this study. However, AuNP could undergo phase change process at high laser fluence and possibly reshaping and fragmentation. Besides melting temperature, the thermal conductivity is also reported to be highly dependent on material size when it comes to nanoscale. Chen et al. estimated the thermal conductivity for 3 nm AuNP to be 24.14 W/(m·K), an order magnitude lower than bulk gold.[200] In our previous study, we compared finite element model and

molecular dynamics model to investigate the material properties of both gold and water in nanoscale.[131] We found an obvious mismatch between two models when we use bulk material properties in FEM. This indicates that the size-dependence of material properties needs to be considered in computational methods. However, a lot remains unknown in this area and further experimental and numerical studies are required to elucidate the heat transfer process in the nanoscale.

4.4.2 Protein inactivation in wide temperature range

In this study, we adopted a conventional Arrhenius model for protein inactivation process in which both prefactor and inactivation energy are independent of temperature. This hypothesis is valid for low temperature range. However in a wider temperature range, the activation energy and prefactor both vary with temperature as demonstrated by our previous study.[160] Also, the protein inactivation process is assumed to a first-order, irreversible process in this study. The thermal inactivation of protein is a much more complicated process and is highly dependent on the protein structure.[201]

4.5 Conclusions

In this study, we numerically investigate protein photoinactivation during MH by combining the heat transfer model with the chemical reaction model. Impact zone is defined to quantify the protein inactivation efficiency. Firstly, we studied the effect of pulse shape and duration and found that stretching the laser pulse duration reduces impact zone with the same laser energy**.** Secondly, we demonstrated that temperature-dependent material density and specific heat have negligible effect on MH, while temperature-dependent thermal conductivity decreases the

impact zone. Thirdly, thermal interface resistance has a limited impact on MH below 1×10^{-8} K m^2 W^{-1}. Lastly, the nanosphere has larger impact volume than nanorods with the same heat generation. In summary, this work provides a theoretical interpretation of protein photoinactivation by MH and offers a clear guideline to design MH for biomedical applications.

CHAPTER 5

CONCLUSION AND FUTURE RESEARCH DIRECTIONS

5.1 Conclusion

In this dissertation, we firstly introduced fundamentals and applications of LSPR. Specifically, we focused on the plasmonic heating in different scales. By carefully checking the thermophysical interactions between light and nanoparticle, we demonstrated the feasibility of generating a nanoscale heating by tuning the laser energy and duration. By systematically reviewing previous works of optical manipulation methods enabled by nanostructures, we demonstrated the feasibility to precisely control biological activity in living systems using light and plasmonic heating. Secondly, we demonstrated an enzyme protein (α-chymotrypsin) can be selectively inactivated by plasmonic heating of AuNP under the irradiation of nanosecond laser. Importantly, the nanosecond laser irradiation leads to a nanoscale heating around the AuNP without causing macroscopic effects, *i.e.* collective heating. This indicates a promising method to control protein behavior in living system, known as molecular hyperthermia (MH). Next, we demonstrated for the first time to switch off protein activity in live cells with MH. We showed that protease-activated receptor 2 (PAR2) and a tight junction protein can be inactivated by MH with good precision. Importantly, MH is a transient and safe protein inactivation method does not cause significant cellular damage. Lastly, to better understand the mechanism of MH, we performed a numerical investigation to systematically study the effects of different parameters in MH, including laser pulse shape and duration, temperature-dependent material properties, interfacial thermal resistance, particle size and shape. This work provides a theoretical interpretation of

protein photoinactivation by MH and offers a clear guideline to design MH for biomedical applications. In summary, MH uses the plasmonic heating of AuNPs in the nanoscale to thermally inactivate proteins of interest. MH is demonstrated to be an effective way to inactivate protein with great precision, and can be a potential therapeutic method for disease treatment without genetic modification.

5.2 Future research directions

For the future development of MH, there are several important fundamental questions need be answered:

(1) How to measure temperature in the nanoscale and in a real-time manner?

The fundamental of this study is based on nanoscale heating generated by plasmonic nanoparticle. We confirmed the nanoscale heating generation with various evidences, including photoacoustic, particle fragmentation and protein inactivation (Chapter 2&3). And we used numerical model to quantitatively estimate the nanoscale heating (Chapter 4). However, to directly measure the temperature in the nanoscale and in real time is always preferred. Unfortunately, there are few reliable experimental tools that can meet this requirement so far. Here, we briefly review some efforts have been done towards this goal. Plech et al. utilized time resolved small angle x-ray scattering (SAXS) to investigate the lattice expansion of AuNP with a femtosecond laser irradiation. With this method, they measured the temperature of AuNP change on an ultra-fast time scale (0.1 ps resolution).[202] They also used wide angle x-ray scattering (WAXS) to check the water expansion signal. Takami et al. measured the temperature of AuNP by monitoring black body emission spectrum.[203] They found that the particle can reach a temperature of about 2500 K.

Instead of using optical methods, nanometre-scale thermometry can also be used to check the temperature around an excited plasmonic nanoparticle. For example, Kucsko et al. used nitrogen-vacancy centers in diamond nanocrystals to directly measure the local thermal environment on length scale as short as 200 nm.[204] For the future development of MH, it is necessary to measure the temperature directly in the nanoscale and in real time.

(2) What is the fate of AuNPs under laser irradiation?

We have observed that the plasmonic nanoparticle can be fragmented after high energy laser irradiation (Figure A5). This raises the following question: does particle fragmentation contribute to protein inactivation during MH? To answer this question, it is necessary to understand the physics of particle fragmentation under the short and ultra-short laser pulse irradiation.

Previous works have been done and demonstrated multiple mechanisms are responsible to laser-induced the particle fragmentation. As stated in Chapter 1, particle fragmentation originated from plasmonic heating. Therefore, it is highly dependent on laser duration and energy. Fragmentation induced by femtosecond laser pulse is triggered mainly by electron-ejection and ionization of the nanoparticle. The ionized nanoparticles could be teared up by Coulomb force under high energy laser pulse, known as Coulomb explosion. On the other hand, nanosecond laser heats particles without charging them, and induces fragmentation by thermal effect such as material melting and thermal evaporation. However, it is still unclear what causes the particle fragmentation of AuNPs under picosecond laser irradiation. It is likely to be a mixed mechanism of both thermal effects and the Coulomb explosion. In 2020, Ziefuss et al. studied the caloric and kinetic related behavior of AuNP fragmentation under picosecond laser.[205] They found that the particle fragmentation happens within 30 ns after laser irradiation, and an arrested growth of the

fragmented particles was observed in a longer time range. However, they cannot determine whether the fragmentation was caused by thermal effects or Coulomb explosion. Knowing the mechanism of particle fragmentation will helps us to design the plasmonic nanoparticles with better laser stability. This will not only benefit applications of MH, but also have a broad impact on investigations in plasmonic nanomaterials.

(3) What is the fate of proteins during MH: fragmentation or unfolding?

The protein inactivation by MH leads to particle aggregation and indicates the protein unfolding (Chapter 2). With a higher laser energy, protein fragmentation was reported (Chapter 1). [46] It is important to understand protein structure change during MH in both a caloric manner and a kinetic manner. The protein fragmentation in liquid under an extreme circumstance is still an unknown area due to the lack of effective experimental methods. The plasmonic heating of AuNPs with high laser energy can generate localized heating and induces high pressure generation. Thus, we can use MH as a novel tool to check the protein structure change under extreme conditions.

(4) Is there any contributions from LSPR effects other than heating?

Beside of plasmonic heating, there are several effects induced by LSPR (Chapter 1). Hot electron transfer is considered to be responsible for various photo-enhanced chemical reactions. Essentially, the protein inactivation is a chemical reaction. This leads us to ask: how much does hot electron transfer contribute to MH? To differentiate plasmonic heating effect from other effects, several practical ways were proposed by Baffou et al, including varying the illumination power, the light beam diameter and polarization, etc.[206] In the future, we can apply these techniques to MH and quantify the contributions from different LSPR effects.

APPENDIX A

SUPPORTING INFORMATION FOR CHAPTER 2

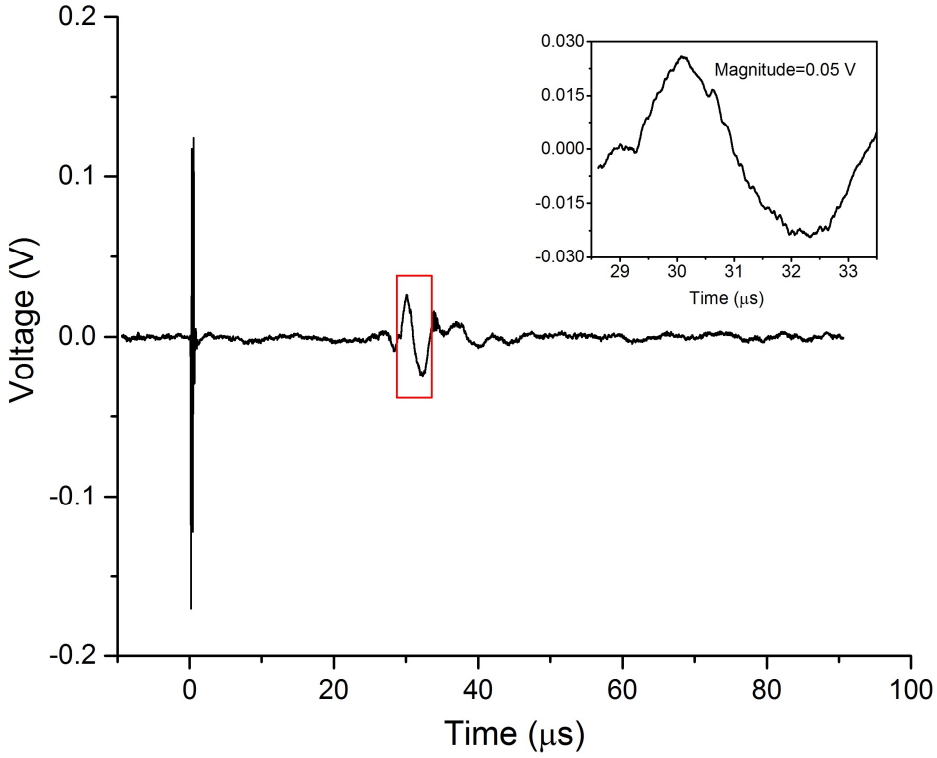

Figure A.1. Photoacoustic measurement of AuNP nanoscale heating induced thermoelastic expansion. The photoacoustic signal is at approximately 30 μs.

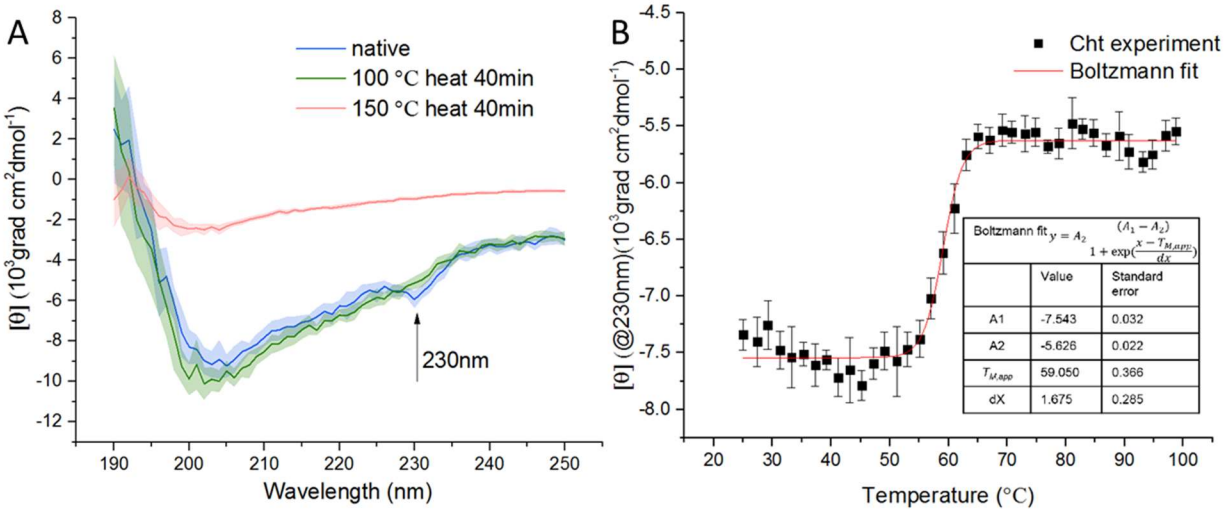

Figure A.2. Circular dichroism (CD) measurement of Cht thermal stability (A) CD spectrum for native and denatured Cht. The obvious CD intensity change at 230 nm corresponds to α-helix structure and was used to monitor the protein melting temperature. (B) Melting temperature of Cht was determined by a temperature scan. A Boltzmann fit was used to calculate the melting temperature.

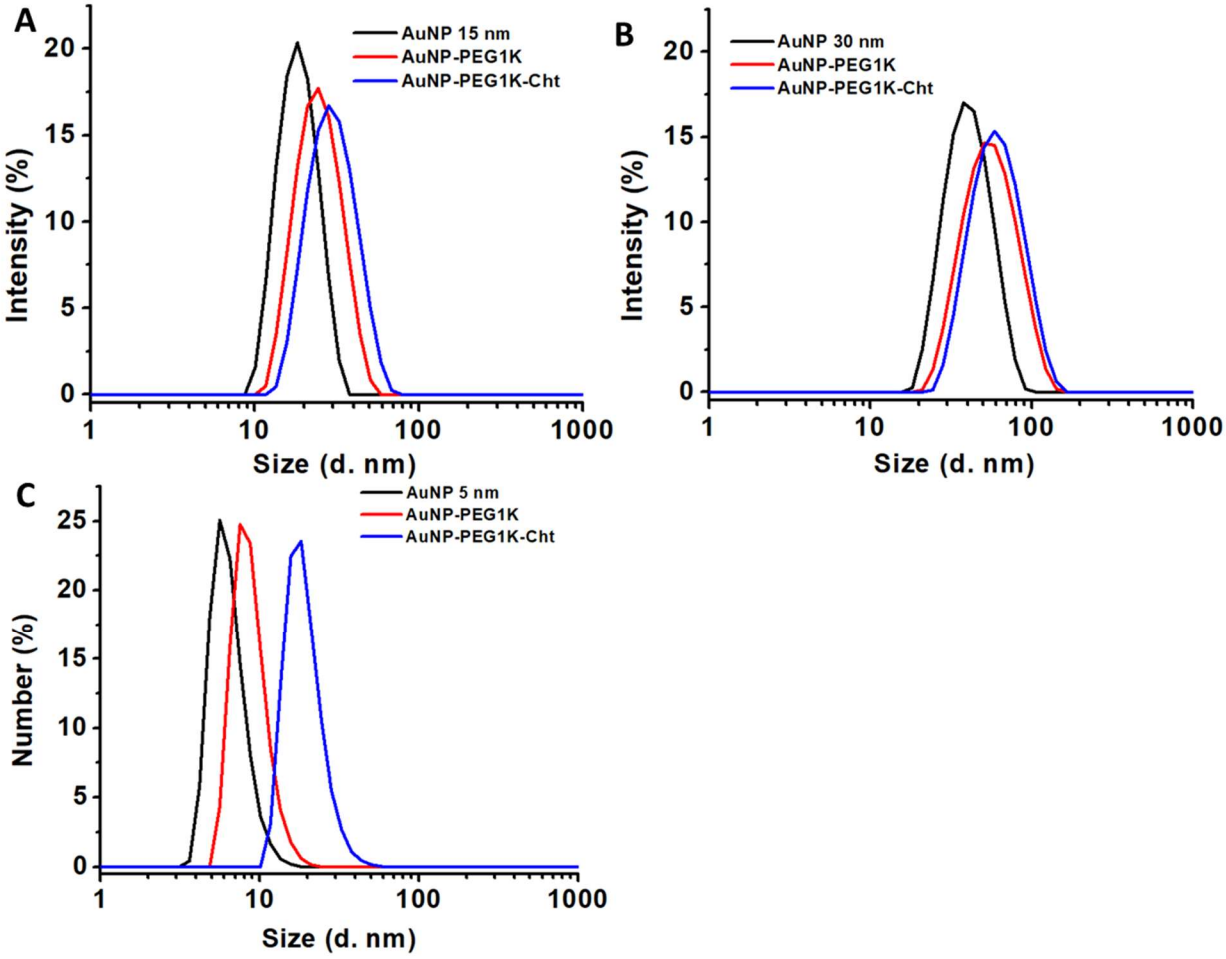

Figure A.3. AuNP characterization by dynamic light scattering (DLS). DLS measurement of 15 nm (A), 30 nm (B) and 5 nm (C). AuNP, including citrate, PEG and Cht coating. The increase in particle diameter after PEG coating was used to estimate the PEG length (4.0 nm for 5 nm AuNP, 3.9 nm for 15 nm AuNP and 5.8 nm for 30 nm AuNP).

Table A.1. The DLS measurement summary for different samples.

Sample	Z-average (nm)	PDI
AuNP 15 nm	17.61	0.053
AuNP-PEG1K 15 nm	25.44	0.096
AuNP-PEG1K-Cht 15 nm	28.16	0.165
AuNP 30 nm	37.29	0.112
AuNP-PEG1K 30 nm	48.83	0.165
AuNP-PEG1K-Cht 30 nm	55.02	0.143
AuNP 5 nm	6.44	0.176
AuNP-PEG1K 5 nm	14.53	0.252
AuNP-PEG1K-Cht 5 nm	19.32	0.343

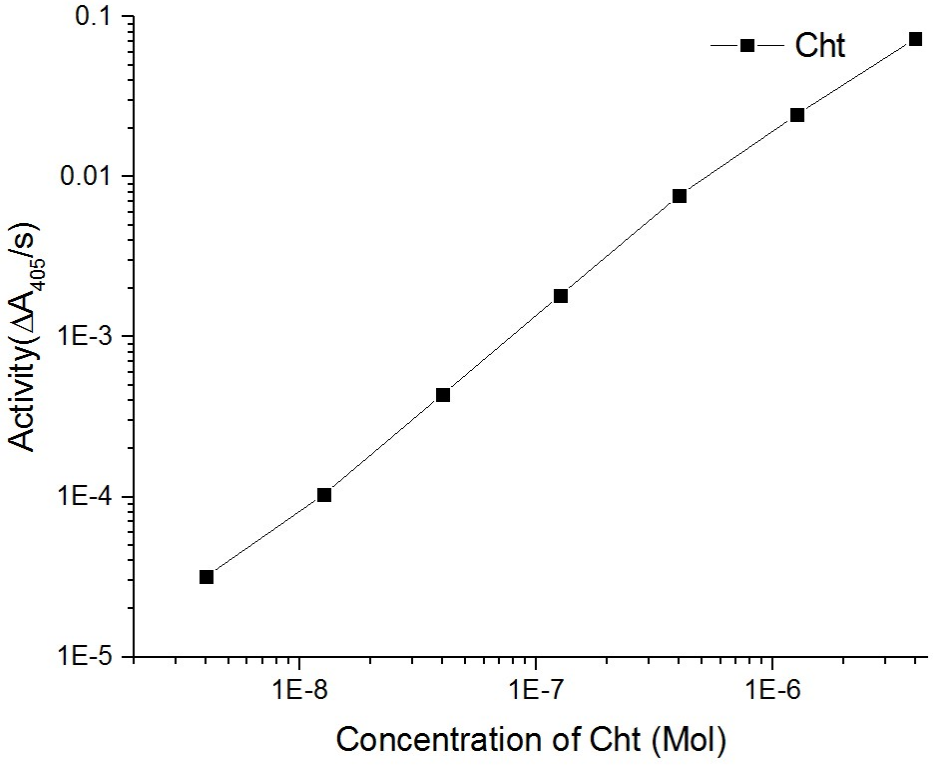

Figure A.4. Standard curve for the protein (Cht) activity. The data is measured at 25 °C for 2 min using the plate reader.

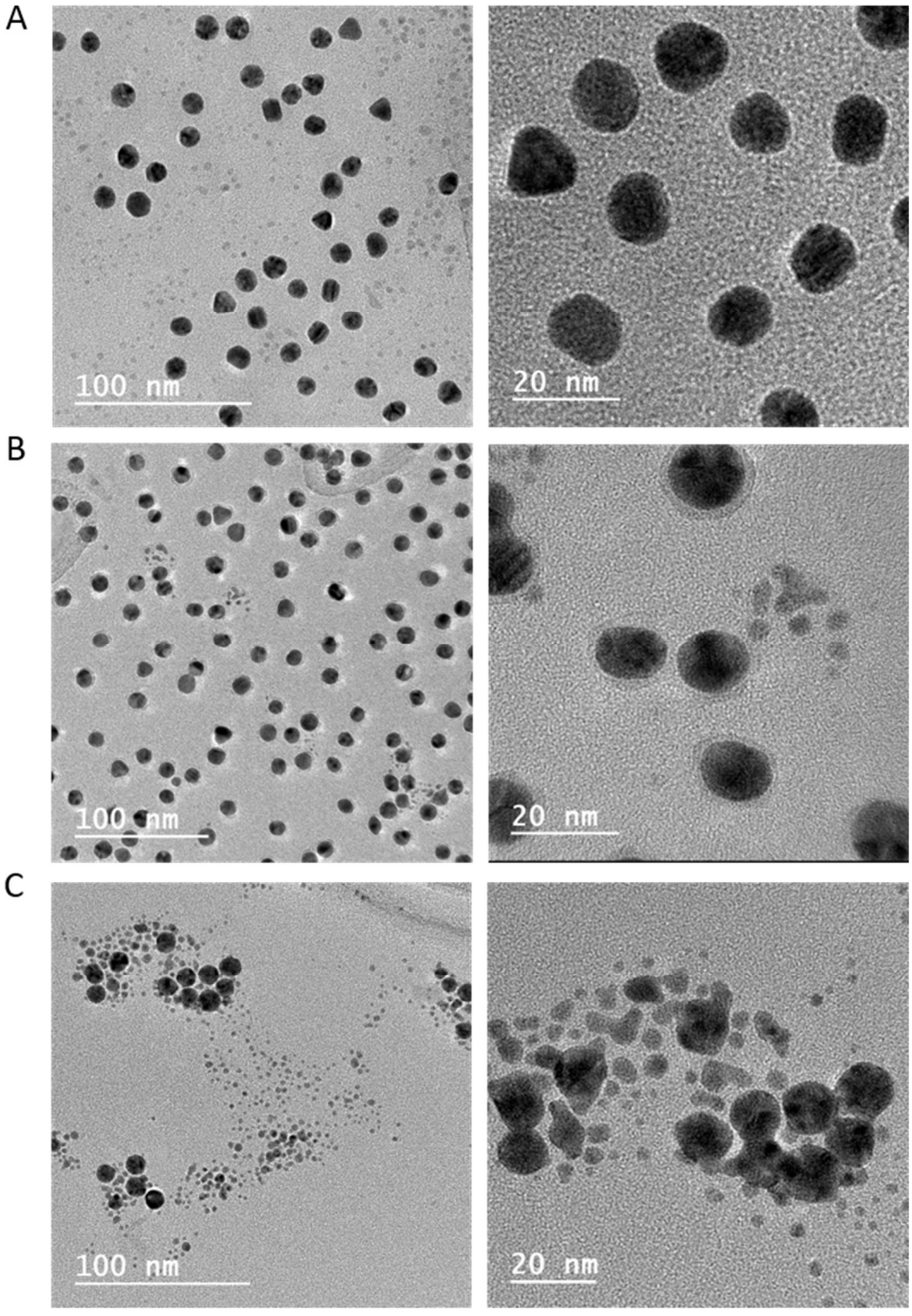

Figure A.5. TEM of AuNPs before and after laser treatment. (A) 15 nm AuNP before laser irradiation; (B) 15 nm AuNP after low power laser pulse irradiation (137 mJ/cm^2). A minor population of smaller particles were seen. (C) 15 nm AuNP after high power laser pulse irradiation (609 mJ/cm^2). Significantly more small particles (3 nm-5 nm) are generated.

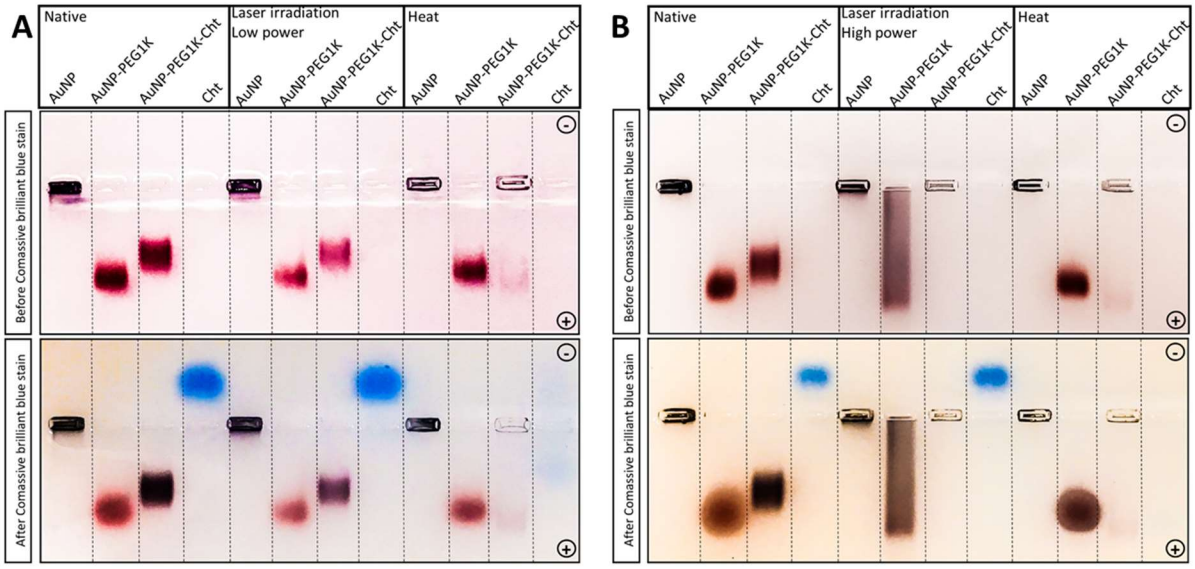

Figure A.6. Agarose gel electrophoresis of AuNP and Cht samples. (A) Electrophoresis for native, low laser pulse energy (136.1 mJ/cm^2) treated, and heat-treated (100 °C for 30 min) samples. Citrated-coated AuNP (labeled as AuNP) is aggregated in the well after adding the TBE buffer, while PEG-coated AuNP can run stably in the gel without aggregation. With additional Cht coating, AuNP-PEG-Cht conjugate runs slower. Due to the positive charge of Cht in the running buffer, the protein traveled towards the negative charge end that can be seen in negative direction after Coomassie brilliant blue staining. The laser treatment does not significant change the electrophoresis behavior of AuNP samples. However, the heating (100 °C for 30 min) leads to AuNP-PEG-Cht aggregation during to protein unfolding. (B) Electrophoresis for high power pulse energy (609.0 mJ/cm^2) shows significant AuNP fragmentation as shown the broader band in PEG-coated AuNP and significant aggregation for AuNP-PEG-Cht conjugate due to protein unfolding.

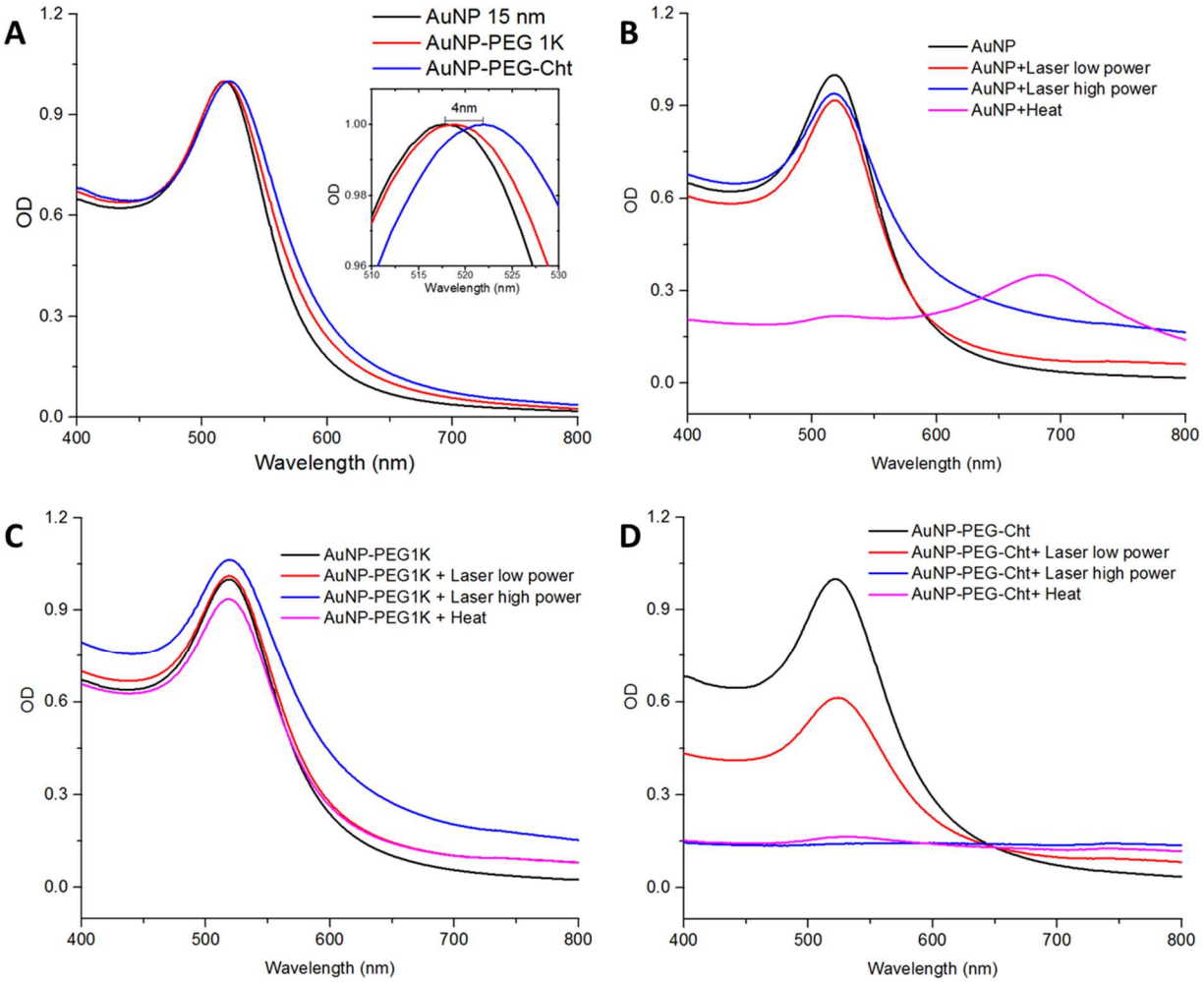

Figure A.7. UV-Vis spectrum for native, laser pulse treated, and heat-treated samples. (A) AuNP samples before laser or heat treatment. PEG coating increases the the peak position of the spectrum by 1 nm and the Cht coating increases the peak wavelength by 4 nm. (B) Citrated stabilized AuNP only show obvious aggregation after bulk heating (boiling for 30 min). (C) PEG coated AuNPs are sTable at all conditions attempted. (D) Cht conjugation leads to particle aggregation at high power pulse energy (609.0 mJ/cm^2) and bulk solution heating (100 °C for 30 min) due to Cht unfolding.

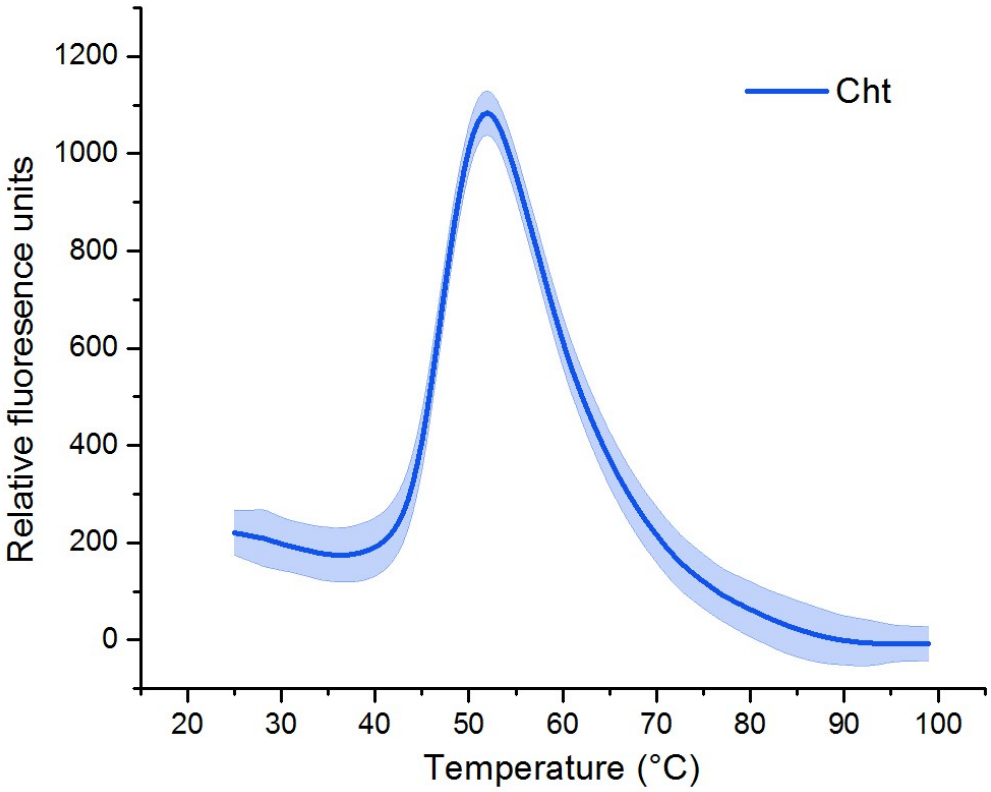

Figure A.8. ThermoFluor measurement of Cht unfolding and aggregation. The data shows that the midpoint temperature of the protein unfold transition (T_m) for Cht is around 47 °C.

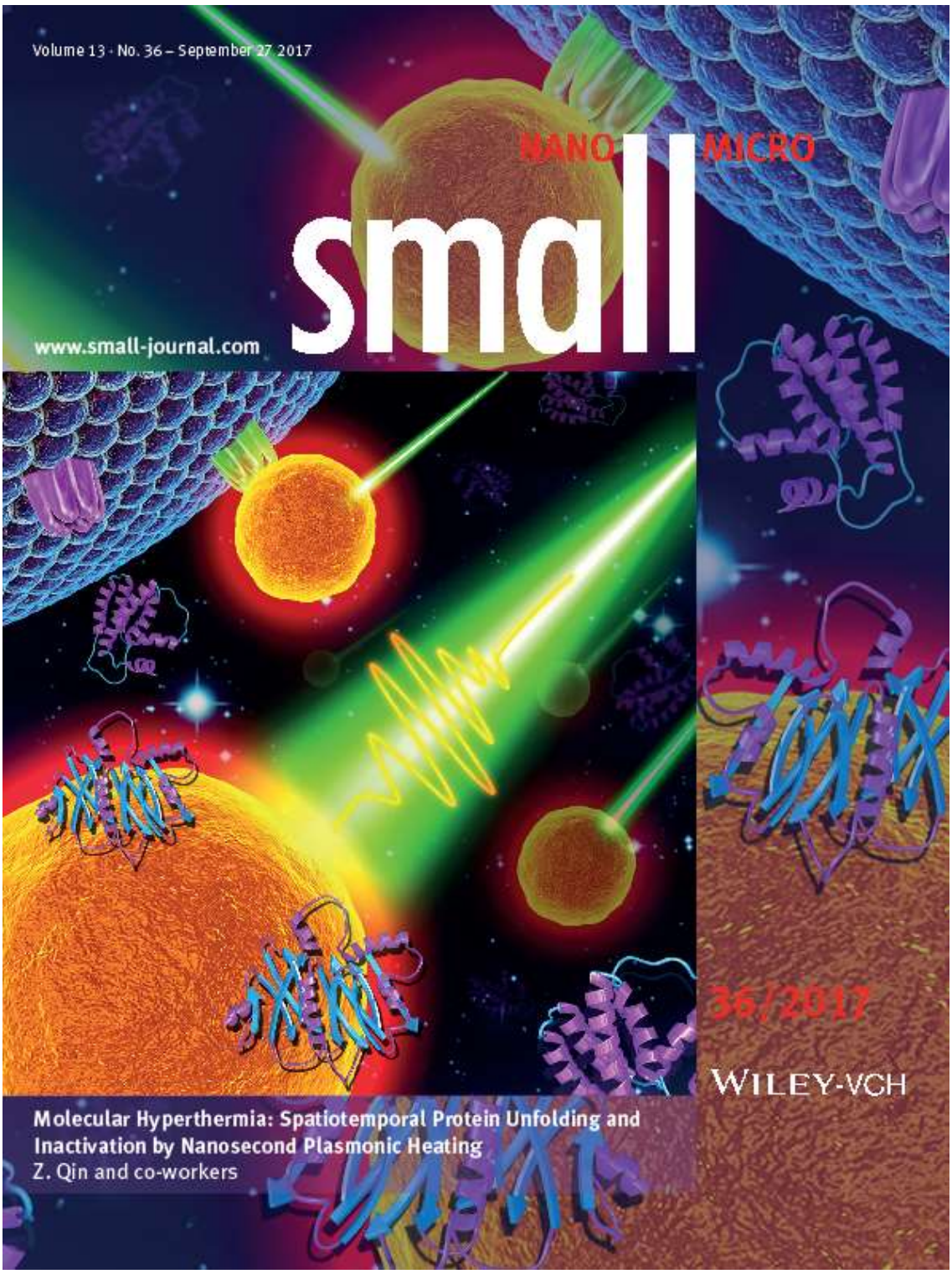

Figure A.9. Journal cover for publication in Chapter 2. [131]

APPENDIX B

SUPPORTING INFORMATION FOR CHAPTER 3

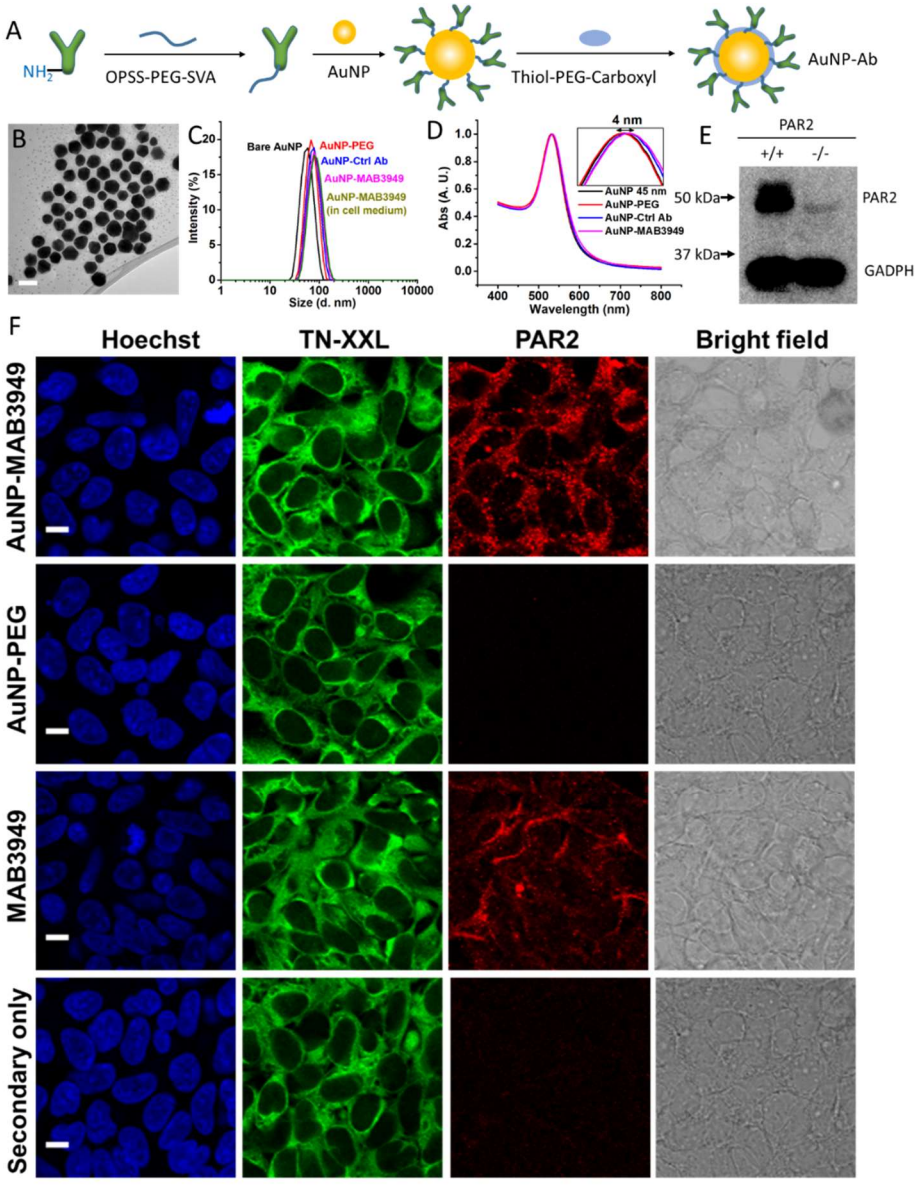

Figure B.1. Characterization of PAR2-targeting plasmonic gold nanoparticles (AuNP). (A) Schematic of the antibody functionalization on AuNP. (B) Transmission electron microscopy (TEM) imaging for 45 nm AuNPs (Scale bar: 50 nm). (C) Dynamic light scattering (DLS) measurements for bare AuNP, polyethylene glycol (PEG) coated AuNP (AuNP-PEG), control

antibody-coated AuNP (AuNP-Ctrl Ab), PAR2-targeting antibody-coated AuNP in borate buffer and in cell medium (AuNP-MAB3949). (D) UV-Vis spectroscopy measurements of AuNPs before and after PEG and MAB3949 modification. The insert shows that the antibody conjugation shifts the peak by 4 nm, from 532nm to 536 nm. (E) Western blot of dorsal root ganglion (DRG) samples from wild type mouse (PAR2 +/+) and PAR2 knockout mouse (PAR2 -/-), GADPH refers to Glyceraldehyde 3-phosphate dehydrogenase. (F) Fluorescent immunocytochemistry imaging of HEK293 cells (prefixed with methanol). Nucleus is in blue (Hoechst), FRET Ca^{2+} indicator (TN-XXL) is in green, and PAR2 is in red (Alexa 633). AuNP-MAB3949, AuNP-PEG, MAB3949 groups represent incubating PAR2 antibody-AuNP conjugate, AuNP-PEG conjugate, and free PAR2 antibody (MAB3949(with the cell after methanol fixing, respectively. The secondary only refers to incubating the cell with secondary antibody only without the primary PAR2 antibody. Scale bar: 10 μm.

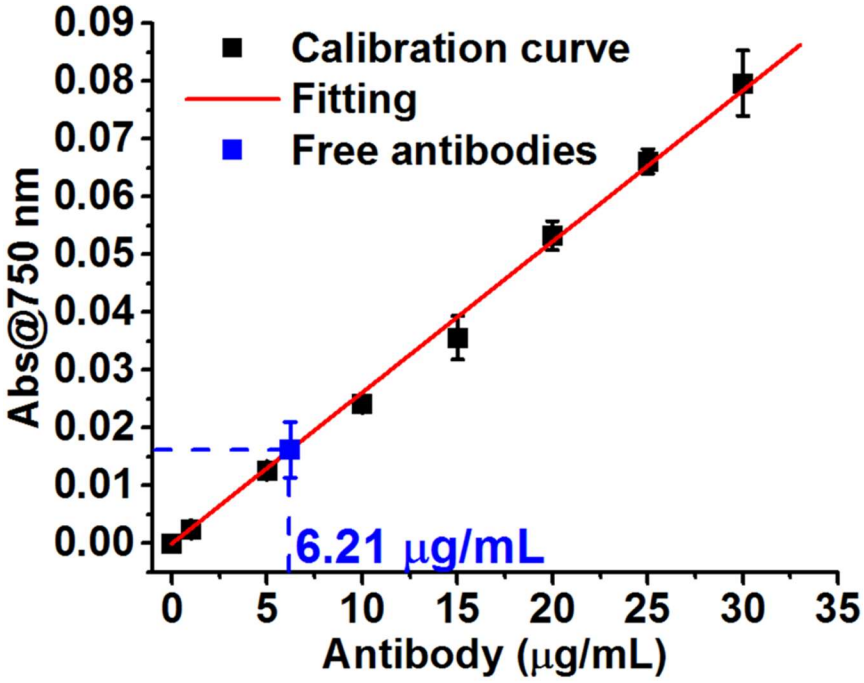

Figure B.2. The standard calibration curve to determine antibody concentration on the AuNP surface. Protein concentration on the AuNP surface was determined by measuring the free antibody in the supernatant after centrifugations (6.21 μg/mL).

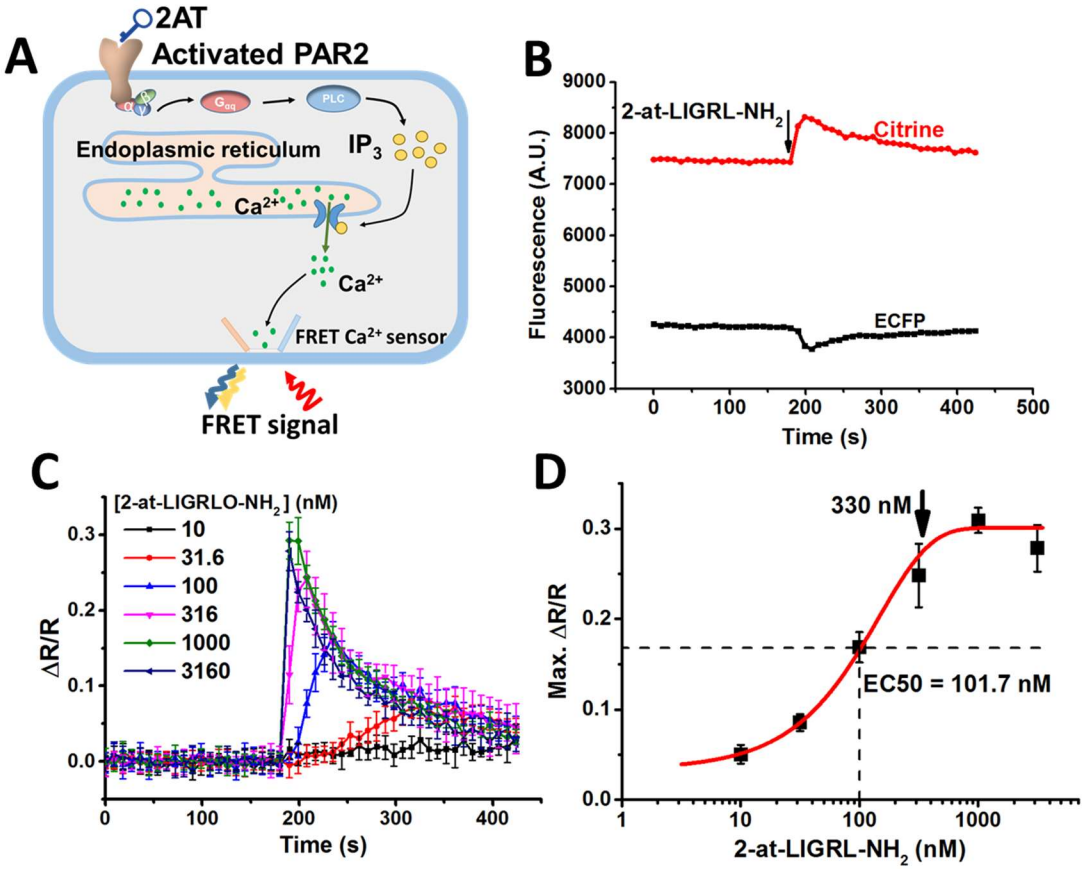

Figure B.3. Ca^{2+} signaling induced by PAR2 activation. (A) Schematic illustrating Ca^{2+} signaling due to PAR2 activation. PAR2 agonist 2-at-LIGRL-NH_2 (2AT) binding leads to robust Ca^{2+} signals that can be measured by a FRET-based Ca^{2+} sensor (TN-XXL). (B) FRET response of Ca^{2+} release due to PAR2 activation by 2AT (316 nM). (C) The FRET ratio (ΔR/R) signal for different concentrations of 2AT. (D) Dose-response curve of maximum ΔR/R for HEK293 cell in response to 2AT (EC50 = 101.5 ± 28.7 nM, n = 4). The black arrow indicates the concentration of 2AT used in this study.

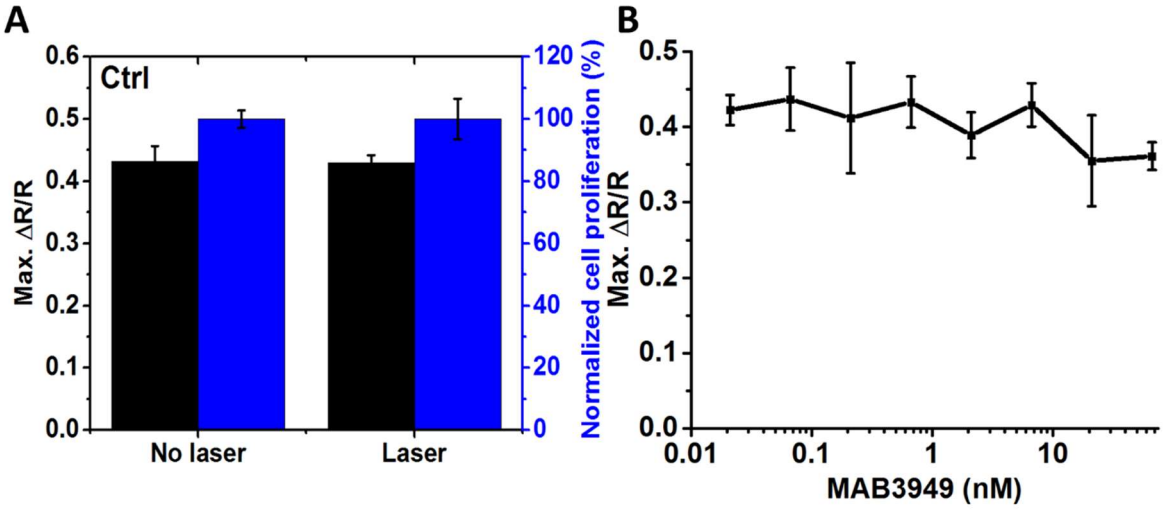

Figure B.4. Additional control experiments for molecular hyperthermia. (A) PAR2 activity and cell viability for the control group (cells without AuNP incubation) before and 30 minutes after laser irradiation (100 mJ/cm^2, 10 pulses). (B) PAR2 activity with MAB3949 incubation shows that MAB3949 alone does not affect PAR2 activity up to 66 nM.

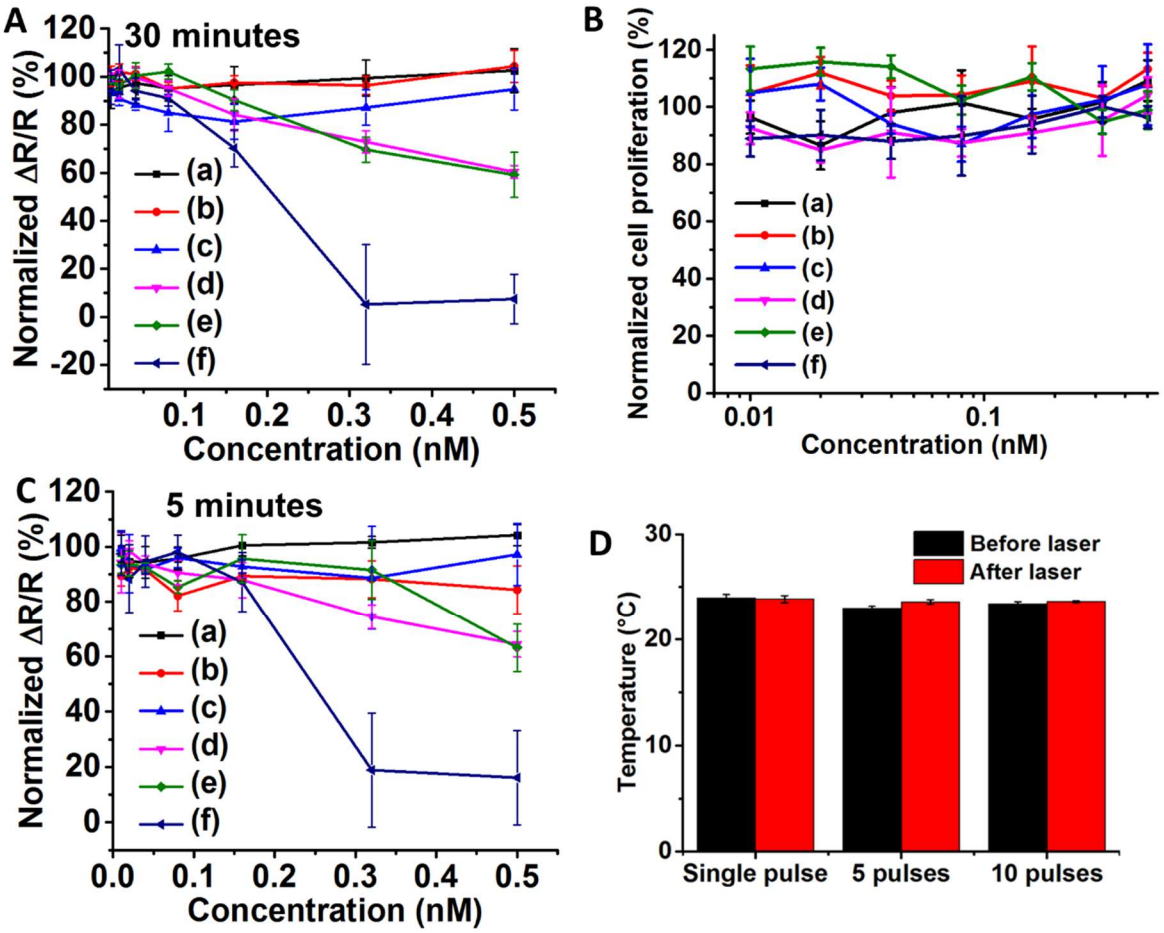

Figure B.5. **Additional data** for (A) Molecular hyperthermia of PAR2 under different particle concentrations. (B) Cell proliferation for different groups. (C) Replot of figure 2E by adding PEG coated AuNP. For all figures: (a) AuNP-PEG, no laser; (b) AuNP-control antibody (Ctrl Ab), no laser; (c) AuNP-MAB3949, no laser; (d) AuNP-PEG, with laser; (e) AuNP-Ctrl Ab, with laser; (f) AuNP-MAB3949, with laser. (D) Bulk medium temperature measurement before and after laser, [AuNP] = 0.5 nM.

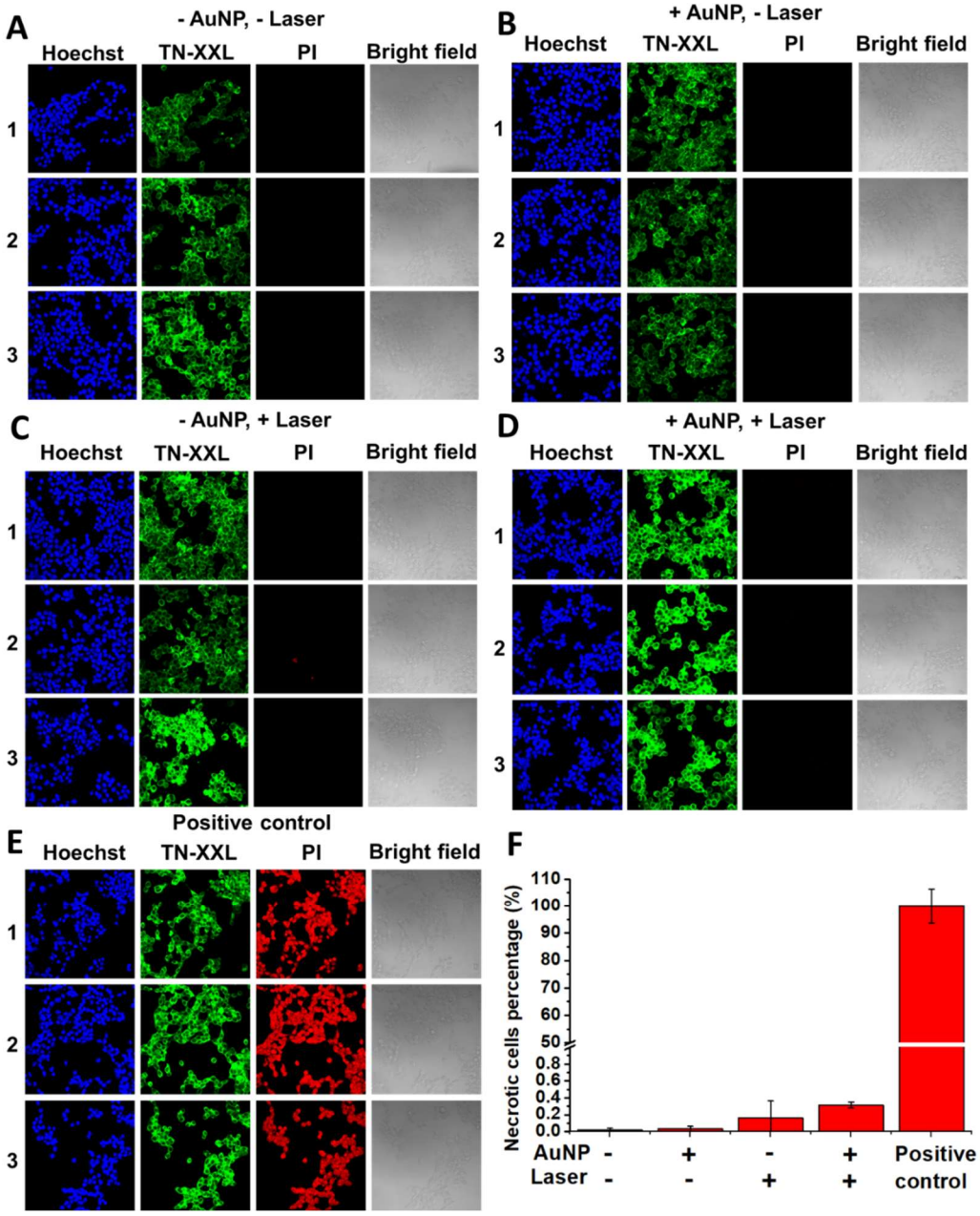

Figure B.6. Propidium iodide (PI) staining assay to examine cell membrane integrity and necrosis. (A) Negative control (no AuNP, no laser), (B) With AuNP incubation, no laser irradiation. (C) With laser irradiation (100 mJ/cm^2, 10 pulses), no AuNP incubation. (D) MH group ([AuNP-MAB3949]=0.32 nM, 100 mJ/cm^2, 10 pulses). (E) Positive control (prefixed cells with 100% methanol). (F) Quantification of necrotic cells percentage. The percentage was calculated by number ratio of PI-stained and Hoechst-stained cells.

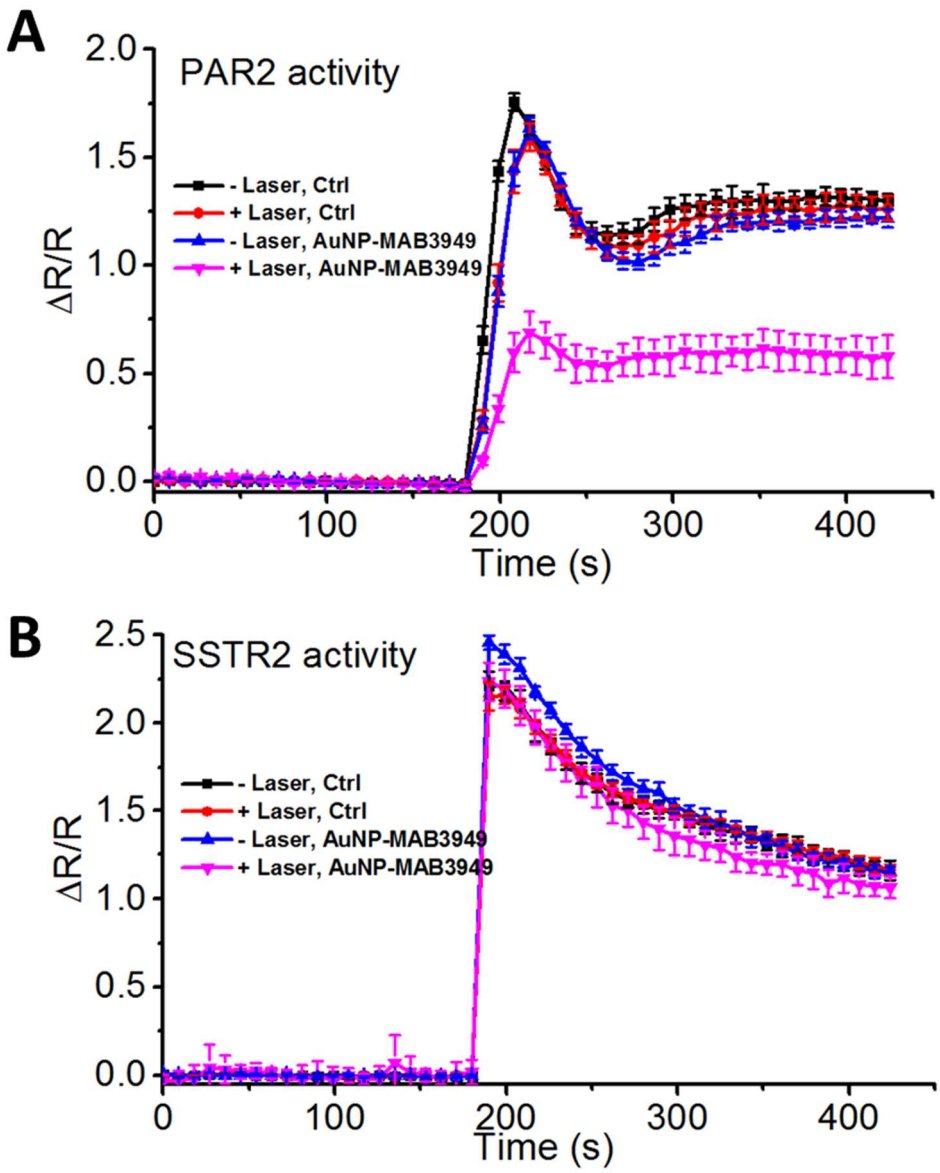

Figure B.7. Selective photo-inactivation of protease activated receptor 2 (PAR2) without compromising somatostatin receptor 2 (SSTR2) activity. (A) Ca^{2+} signal by PAR2 activation. (B) Ca^{2+} signal by SSTR2 activation.

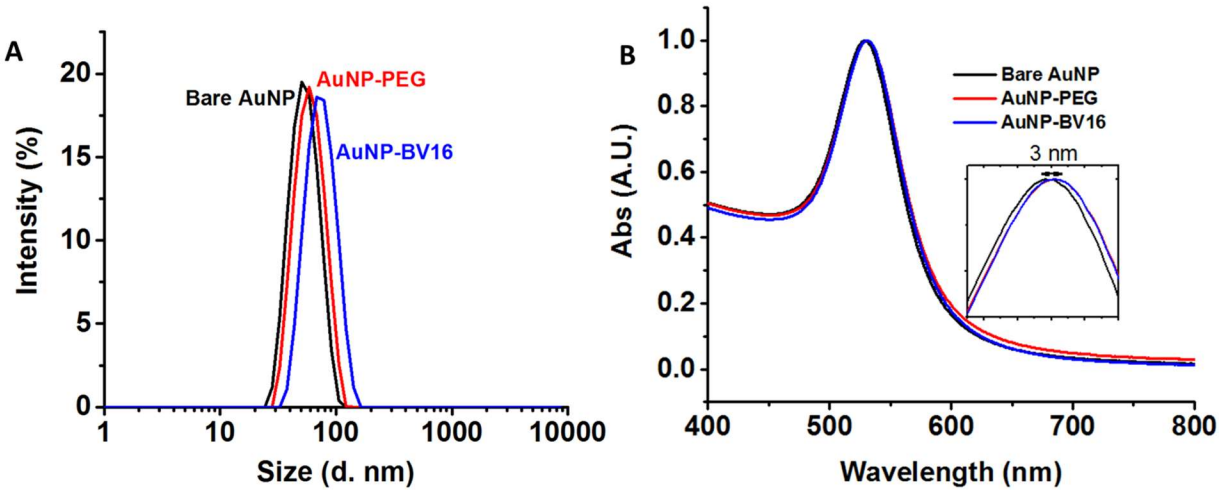

Figure B.8. Characterization of JAM-A antibody (BV16) coated AuNP. (A) DLS and (B) UV-Vis measurements. AuNP-PEG is included as a control group. The insert shows that the antibody conjugation shifted the peak by 3 nm.

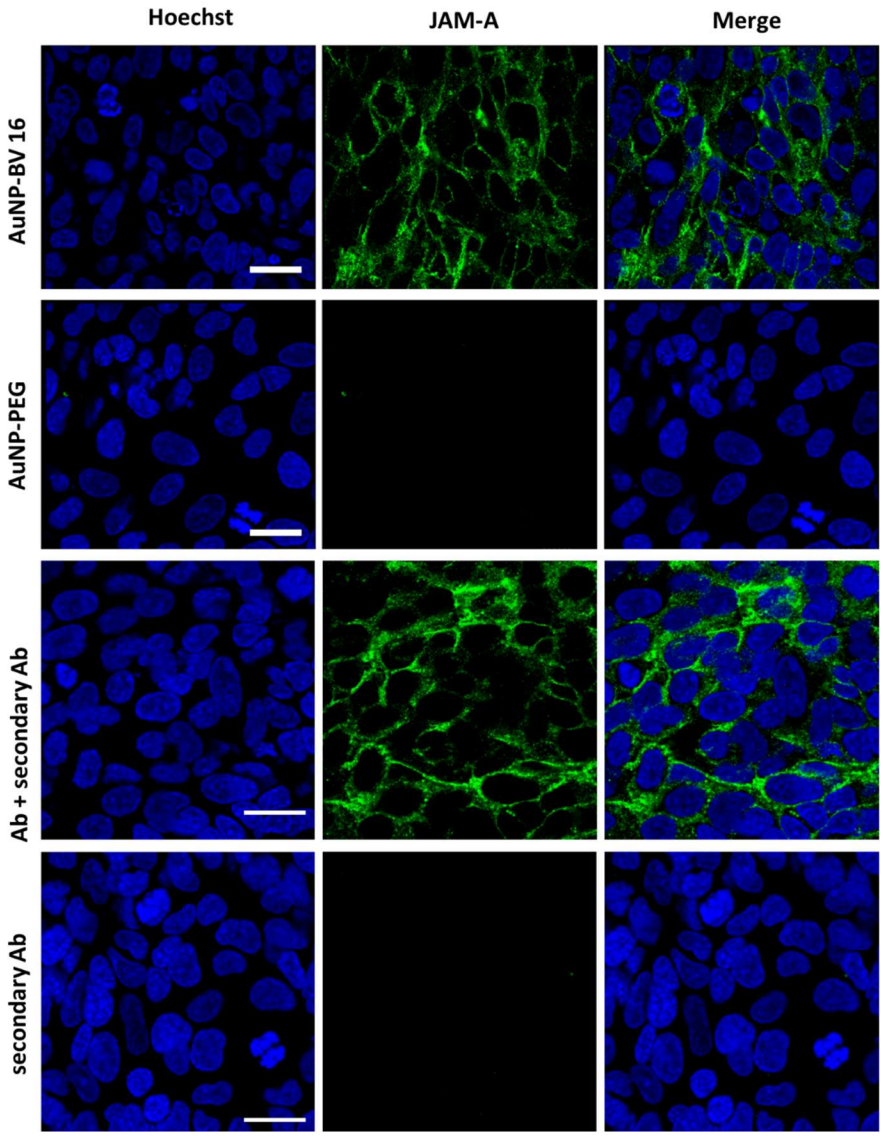

Figure B.9. Fluorescent immunocytochemistry staining of hCMEC/D3 cells. AuNP concentration is 0.5 nM, BV-16 concentration is 5 μg/mL and incubation time is 30 mins. Nucleus is in blue (Hoechst), JAM-A is in green (secondary antibody conjugate with Alexa 488) (scale bar: 20 μm).

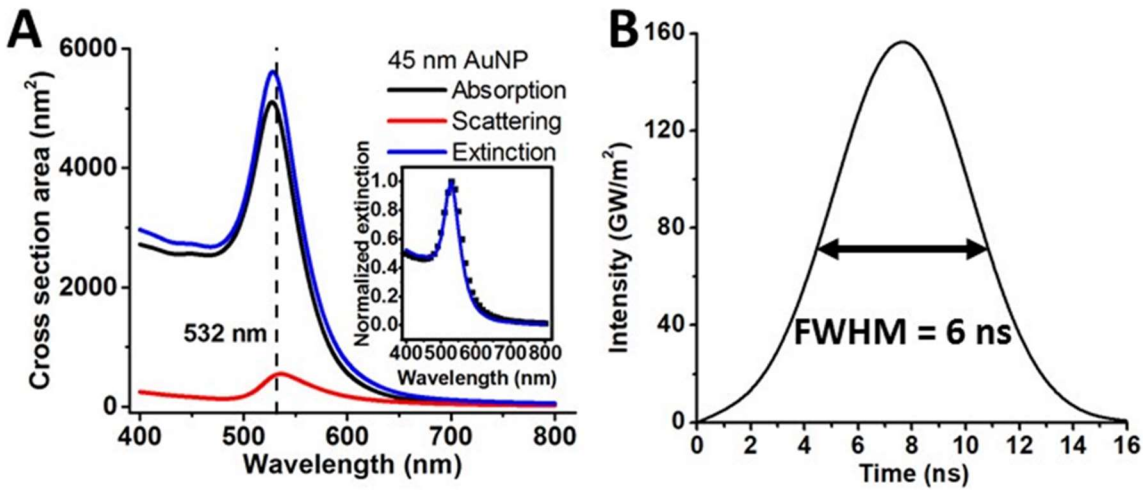

Figure B.10. Optical properties of 45 nm AuNPs and laser power profile. (A) Optical properties of 45 nm AuNPs simulated by Mie theory. The insert shows a comparison of normalized extinction coefficient from Mie theory (line) with experimental measurement (black square). (B) Nanosecond laser pulse profile (full width half maximum or FWHM = 6 ns).

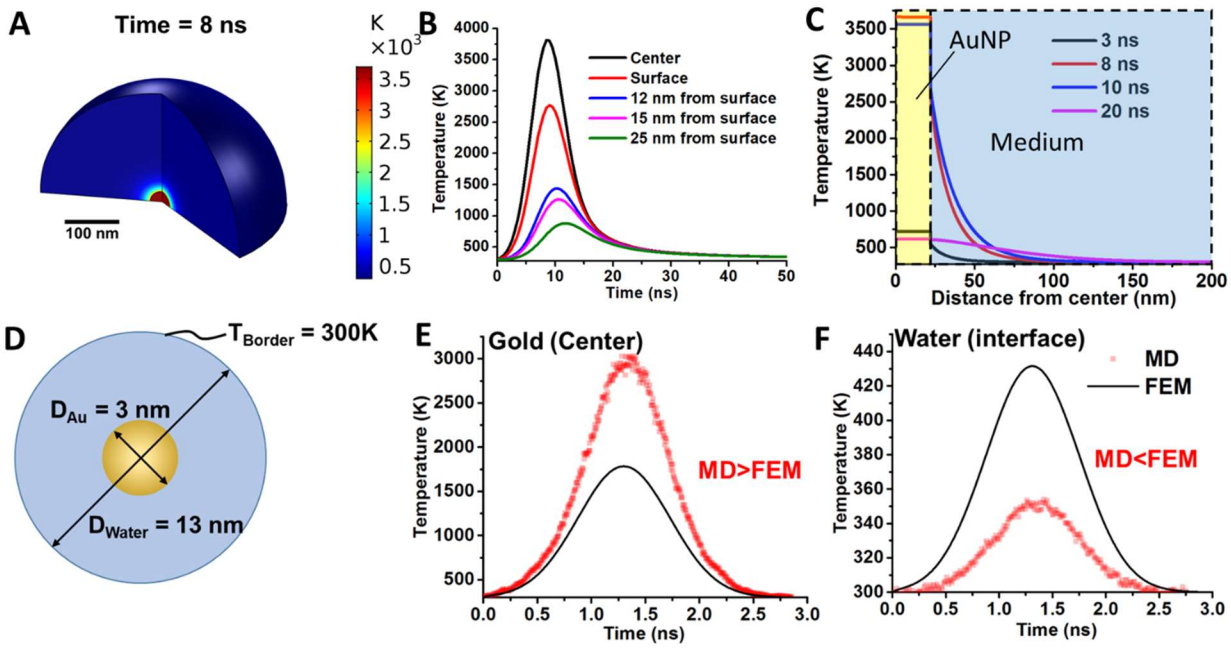

Figure B.11. Simulation of gold nanoparticle laser heating and comparison of finite element method (FEM) and molecular dynamics (MD) simulation. (A) 3D temperature distribution of AuNP and surrounding medium at 8 ns in response to a 100 mJ/cm^2 nanosecond laser pulse. (B) Temperature distribution of AuNP and surrounding medium at different time points. (C) Temperature profile of AuNP and surrounding medium as a function of time at different distances. (D) Model geometry for molecular dynamics (MD) and finite element method (FEM) simulation. (E) Temperature profile at the AuNP center for MD and FEM methods. (F) Temperature profile of water at the gold nanoparticle surface for MD and FEM methods.

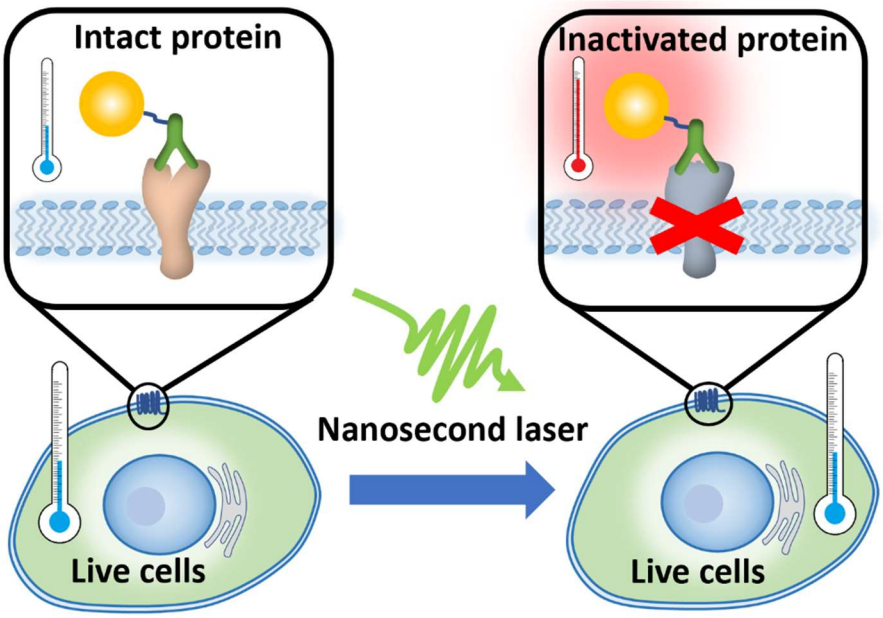

Figure B.12. Schematic illustration of molecular hyperthermia

Table B.1. Lennard-Jones (LJ) parameters for TIP3P and and non-bonded interactions.[144]

Parameters	Values
$\varepsilon_{AuO}(kJ/mol)$	0.588
$\sigma_{AuO}(\dot{A})$	3.383
$\varepsilon_{OO}(kJ/mol)$	0.646
$\sigma_{OO}(\dot{A})$	3.166
$\varepsilon_{OH}(kJ/mol)$	0.000
$\sigma_{OH}(\dot{A})$	2.473
$\varepsilon_{HH}(kJ/mol)$	0.000
$\sigma_{HH}(\dot{A})$	1.781

APPENDIX C

SUPPORTING INFORMATION FOR CHAPTER 4

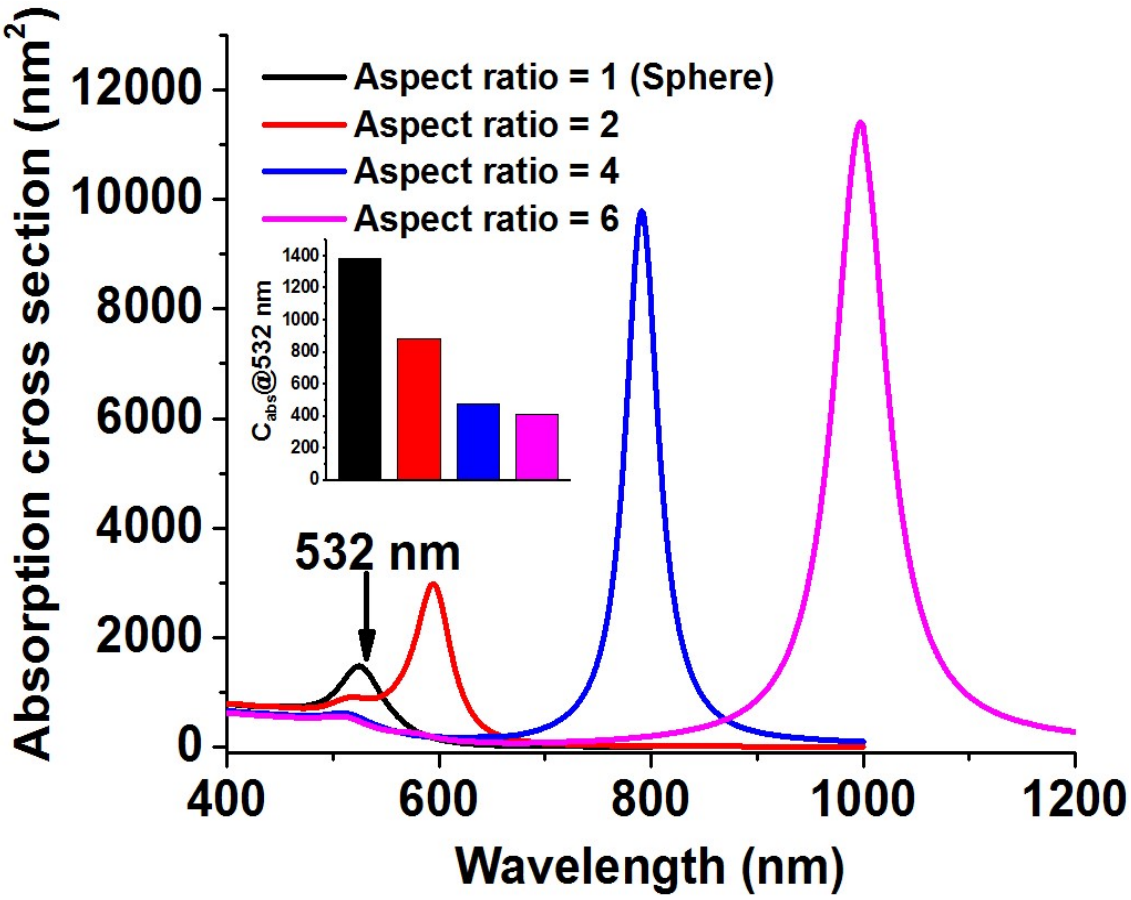

Figure C.1. Calculated absorption cross section (C_{abs}) for gold nanosphere and nanorods with different aspect ratio.

APPENDIX D

MATLAB FUNCTION

This Matlab function calculates the analytic solution in Table 4.2.

```
function
[T,radius,time]=goldenberg(R_NP,C_abs,R_dom,I,laser_dur,sim_dur,
dim_t,dim_r)
syms t r T1 T2
densw = 1000;
condw = 0.6;
condg = 317;
cpw = 4.2*10^3;
densg = 19.3*10^3;
cpg = 129;
thdifg = 1.27*10^-4;
thdifw = 1.47*10^-7;
% GNP size
R_NP = R_NP*10^-9;
V = 4/3 * pi * R_NP^3;
A = 4 * pi * R_NP^2;
R_dom = R_dom*10^-9;
% laser properties;
heatgenerate = I*C_abs*10^-18; %W/m^2*m^2
g = heatgenerate / V;
sim_dur = sim_dur*10^-9;
laser_dur = laser_dur*10^-9;
lp = thdifg*laser_dur/(R_NP^2);
% equation constant
a = R_NP^2 / thdifg;
b = (condw / condg) * sqrt(thdifg/thdifw);
c = 1 - condw / condg;
% for step
timestep = dim_t;
mesh = dim_r;
delt = sim_dur/timestep;
delx = R_dom/mesh;

for j=1:(timestep + 1);

    t=delt*(j-1);
```

```
    time(j)=t;

    tau(j) = thdifg*t/(R_NP^2);

    for i=1:(mesh+1);

        r= delx*(i-1);

        radius(i) = r;

        gamma(i) = r/R_NP;

        w(i) = (r/R_NP-1)*sqrt(thdifg/thdifw);

     if tau(j) < lp;

        if gamma(i) < 1;

            in1=@(y)(exp (-y.^2.*tau(j))./(y.^2)).*(sin(y)-
y.*cos(y)).*sin (gamma(i).*y)./((c.*sin(y)-
y.*cos(y)).^2+b^2.*y.^2.*(sin(y)).^2);

            inte1(i,j)=integral(in1,0,inf); %quadgk

            thet(i,j)=condg/3/condw+(1-gamma(i).^2)/6-
2*b./gamma(i)/pi.*inte1(i,j);
        else

            in2 = @(y)(exp (-y.^2*tau(j))./(y.^3)).*(sin(y)-
y.*cos(y)).*(b*y.*sin(y).*cos(w(i).*y)-(c.*sin(y)-
y.*cos(y)).*sin(w(i).*y))./((c.*sin(y)-
y.*cos(y)).^2+(b^2).*(y.^2).*(sin(y)).^2);

            inte2(i,j)=integral(in2,0,inf);

            thet(i,j) = (condg/3/condw-
2/pi*inte2(i,j))/gamma(i);
        end
      else
          if gamma(i) < 1;

            in1=@(y)(exp (-y.^2.*(tau(j)-laser_dur/a))-exp (-
y.^2*tau(j)))./(y.^2).*(sin(y)-y.*cos(y)).*sin
```

```
(gamma(i).*y)./((c.*sin(y)-
y.*cos(y)).^2+b^2.*y.^2.*(sin(y)).^2);

            inte1(i,j)=integral(in1,0,inf);

            thet(i,j)=2*b./gamma(i)/pi.*inte1(i,j);
          else
            in2 = @(y)(exp (-y.^2.*(tau(j)-laser_dur/a))-exp (-
y.^2*tau(j))))./(y.^3).*(sin(y)-
y.*cos(y)).*(b*y.*sin(y).*cos(w(i).*y)-(c.*sin(y)-
y.*cos(y)).*sin(w(i).*y))./((c.*sin(y)-
y.*cos(y)).^2+(b^2).*(y.^2).*(sin(y)).^2);

             inte2(i,j)=integral(in2,0,inf);

             thet(i,j) = 2/pi*inte2(i,j)/gamma(i);
          end
      end
    end
end
thet(1,:)=thet(2,:);
T = abs(thet * R_NP^2 *g / condg);
```

REFERENCES

(1)Jauffred, L.; Samadi, A.; Klingberg, H.; Bendix, P. M.; Oddershede, L. B., Plasmonic Heating of Nanostructures. *Chem Rev* **2019,** *119*, 8087-8130.

(2)Feynman, R. P., *There is Plenty of Room at the Bottom: An Invitation to Enter a New Field of Physics*. 3 ed.; Taylor & Francis Group: CRC Press: Boca Raton, 2012.

(3)Pelton, M.; Bryant, G., *Introduction to Metal-Nanoparticle Plasmonics*. John Wiley & Sons: Hoboken, New Jersey, 2013.

(4)Liu, X., Colloidal Plasmonic Nanoparticles for Ultrafast Optical Switching and Laser Pulse Generation. *Frontiers in Materials* **2018,** *5*.

(5)Wang, L.; Zhang, T.; Li, P.; Huang, W.; Tang, J.; Wang, P.; Liu, J.; Yuan, Q.; Bai, R.; Li, B.; Zhang, K.; Zhao, Y.; Chen, C., Use of Synchrotron Radiation-Analytical Techniques To Reveal Chemical Origin of Silver-Nanoparticle Cytotoxicity. *ACS Nano* **2015,** *9*, 6532-6547.

(6)Park, K.; Lee, D.; Rai, A.; Mukherjee, D.; Zachariah, M. R., Size-Resolved Kinetic Measurements of Aluminum Nanoparticle Oxidation with Single Particle Mass Spectrometry. *The Journal of Physical Chemistry B* **2005,** *109*, 7290-7299.

(7)Myroshnychenko, V.; Rodríguez-Fernández, J.; Pastoriza-Santos, I.; Funston, A. M.; Novo, C.; Mulvaney, P.; Liz-Marzán, L. M.; García de Abajo, F. J., Modelling the Optical Response of Gold Nanoparticles. *Chem. Soc. Rev.* **2008,** *37*, 1792-1805.

(8)Huang, X.; El-Sayed, M. A., Gold Nanoparticles: Optical Properties and Implementations in Cancer Diagnosis and Photothermal Therapy. *Journal of Advanced Research* **2010,** *1*, 13-28.

(9)Ma, X. C.; Dai, Y.; Yu, L.; Huang, B. B., Energy Transfer in Plasmonic Photocatalytic Composites. *Light Sci Appl* **2016,** *5*, e16017.

(10)Hashimoto, S.; Werner, D.; Uwada, T., Studies on the Interaction of Pulsed Lasers with Plasmonic Gold Nanoparticles toward Light Manipulation, Heat Management, and

Nanofabrication. *Journal of Photochemistry and Photobiology C: Photochemistry Reviews* **2012,** *13*, 28-54.

(11)Perrault, S. D.; Chan, W. C. W., Synthesis and Surface Modification of Highly Monodispersed, Spherical Gold Nanoparticles of 50−200 nm. *Journal of American Chemical Society* **2010,** *132*, 11824-11824.

(12)Fang, N.; Lee, H.; Sun, C.; Zhang, X., Diffraction-Limited Optical Imaging with a Silver Superlens. *Science* **2005,** *308*, 534-537.

(13)Koya, A. N.; Cunha, J.; Guo, T.-L.; Toma, A.; Garoli, D.; Wang, T.; Juodkazis, S.; Cojoc, D.; Proietti Zaccaria, R., Novel Plasmonic Nanocavities for Optical Trapping-Assisted Biosensing Applications. *Advanced Optical Materials* **2020,** *n/a*, 1901481.

(14)Zhang, W.; Martin, O. J. F., A Universal Law for Plasmon Resonance Shift in Biosensing. *ACS Photonics* **2015,** *2*, 144-150.

(15)Hoang, T. B.; Akselrod, G. M.; Mikkelsen, M. H., Ultrafast Room-Temperature Single Photon Emission from Quantum Dots Coupled to Plasmonic Nanocavities. *Nano Lett.* **2016,** *16*, 270-275.

(16)Kim, S.; Jin, J.; Kim, Y.-J.; Park, I.-Y.; Kim, Y.; Kim, S.-W., High-harmonic Generation by Resonant Plasmon Field Enhancement. *Nature* **2008,** *453*, 757-760.

(17)Fan, X.; Zheng, W.; Singh, D. J., Light Scattering and Surface Plasmons on Small Spherical Particles. *Light: Sci. Appl.* **2014,** *3*, e179-e179.

(18)Zhang, Y.; Yang, B.; Ghafoor, A.; Zhang, Y.; Zhang, Y.-F.; Wang, R.-P.; Yang, J.-L.; Luo, Y.; Dong, Z.-C.; Hou, J. G., Visually Constructing the Chemical Structure of a Single Molecule by Scanning Raman Picoscopy. *National Science Review* **2019,** *6*, 1169-1175.

(19)Furube, A.; Hashimoto, S., Insight into Plasmonic Hot-Electron Transfer and Plasmon Molecular Drive: New Dimensions in Energy Conversion and Nanofabrication. *NPG Asia Materials* **2017,** *9*, e454-e454.

(20)Dubi, Y.; Sivan, Y., “Hot” Electrons in Metallic Nanostructures—Non-Thermal Carriers or Heating? *Light: Sci. Appl.* **2019,** *8*, 89.

(21)Cortés, E.; Xie, W.; Cambiasso, J.; Jermyn, A. S.; Sundararaman, R.; Narang, P.; Schlücker, S.; Maier, S. A., Plasmonic Hot Electron Transport Drives Nano-Localized Chemistry. *Nature Communications* **2017,** *8*, 14880.

(22)Waxengger, J.; Trugler, A.; Hohenester, U., Plasmonics Simulations with the MNPBEM Toolbox: Consideration of Substrates and Layer Structures. *Comput. Phys. Comm.* **2015,** *193*, 138-150.

(23)Draine, B. T.; Flatau, P. J., Discrete-Dipole Approximation For Scattering Calculations. *Journal of the Optical Society of America A* **1994,** *11*, 1491-1499.

(24)Namiki, T., A new FDTD algorithm based on alternating-direction implicit method. *IEEE Transactions on Microwave Theory and Techniques* **1999,** *47*, 2003-2007.

(25)Sebba, D. S.; Watson, D. A.; Nolan, J. P., High Throughput Single Nanoparticle Spectroscopy. *ACS Nano* **2009,** *3*, 1477-1484.

(26)Taylor, R. W.; Mahmoodabadi, R. G.; Rauschenberger, V.; Giessl, A.; Schambony, A.; Sandoghdar, V., Interferometric Scattering Microscopy Reveals Microsecond Nanoscopic Protein Motion on a Live Cell Membrane. *Nat. Photonics* **2019,** *13*, 480-487.

(27)Link, S.; El-Sayed, M. A., Spectral Properties and Relaxation Dynamics of Surface Plasmon Electronic Oscillations in Gold and Silver Nanodots and Nanorods. *The Journal of Physical Chemistry B* **1999,** *103*, 8410-8426.

(28)Nguyen, S. C.; Zhang, Q.; Manthiram, K.; Ye, X.; Lomont, J. P.; Harris, C. B.; Weller, H.; Alivisatos, A. P., Study of Heat Transfer Dynamics from Gold Nanorods to the Environment via Time-Resolved Infrared Spectroscopy. *ACS Nano* **2016,** *10*, 2144-2151.

(29)Chen, J. K.; Beraun, J. E.; Tham, C. L., Investigation of Thermal Response Caused by Pulse Laser Heating. *Numerical Heat Transfer, Part A: Applications* **2003,** *44*, 705-722.

(30)Qin, Z.; Bischof, J. C., Thermophysical and Biological Responses of Gold Nanoparticle Laser Heating. *Chem. Soc. Rev.* **2012,** *41*, 1191-1217.

(31)Huang, X.; Jain, P. K.; El-Sayed, I. H.; El-Sayed, M. A., Plasmonic Photothermal Therapy (PPTT) Using Gold Nanoparticles. *Lasers Med Sci* **2008,** *23*, 217-28.

(32)Petrova, H.; Lin, C.-H.; Liejer, S. d.; Hu, M.; McLellan, J. M.; Siekkinen, A. R.; Wiley, B. J.; Marquez, M.; Xia, Y.; Sader, J. E.; Hartland, G. V., Time-resolved Spectroscopy of Silver Nanocubes: Observation and Assignment of Coherently Excited Vibrational Modes. *The Journal of Chemical Physics* **2007,** *126*, 094709.

(33)Werner, D.; Hashimoto, S., Improved Working Model for Interpreting the Excitation Wavelength- and Fluence-Dependent Response in Pulsed Laser-Induced Size Reduction of Aqueous Gold Nanoparticles. *J. Phys. Chem. C* **2011,** *115*, 5063-5072.

(34)Pang, G. A.; Laufer, J.; Niessner, R.; Haisch, C., Photoacoustic Signal Generation in Gold Nanospheres in Aqueous Solution: Signal Generation Enhancement and Particle Diameter Effects. *J. Phys. Chem. B* **2016,** *120*, 17646-27656.

(35)Wilson, A. M.; Mazzaferri, J.; Bergeron, E.; Patskovsky, S.; Marcoux-Valiquette, P.; Costantino, S.; Sapieha, P.; Meunier, M., *In Vivo* Laser-Mediated Retinal Ganglion Cell Optoporation Using KV1.1 Conjugated Gold Nanoparticles. *Nano Lett.* **2018,** *18*, 6981-6988.

(36)Ho, S. N.; Hunt, H. D.; Horton, R. M.; Pullen, J. K.; Pease, L. R., Site-directed mutagenesis by overlap extension using the polymerase chain reaction. *Gene* **1989,** *77*, 51-59.

(37)You, M.; Li, Z.; Feng, S.; Gao, B.; Yao, C.; Hu, J.; Xu, F., Ultrafast Photonic PCR Based on Photothermal Nanomaterials. *Trends Biotechnol.* **2020**.

(38)Son, J. H.; Cho, B.; Hong, S.; Lee, S. H.; Hoxha, O.; Haack, A. J.; Lee, L. P., Ultrafast Photonic PCR. *Light: Sci. Appl.* **2015,** *4*, e280-e280.

(39)Stehr, J.; Hrelescu, C.; Sperling, R. A.; Raschke, G.; Wunderlich, M.; Nichtl, A.; Heindl, D.; Kürzinger, K.; Parak, W. J.; Klar, T. A.; Feldmann, J., Gold NanoStoves for Microsecond DNA Melting Analysis. *Nano Lett.* **2008,** *8*, 619-623.

(40)Huo, S.; Gong, N.; Jiang, Y.; Chen, F.; Guo, H.; Gan, Y.; Wang, Z.; Herrmann, A.; Liang, X.-J., Gold-DNA Nanosunflowers for Efficient Gene Silencing with Controllable Transformation. *Science Advances* **2019,** *5*, eaaw6264.

(41)Huttmann, G.; Radt, B.; Serbin, J.; Birngruber, R., Inactivation of Proteins by Irradiation of Gold Nanoparticles with Nano- and Picosecond Laser Pulses. *Proc. SPIE* **2003,** *5142*, 88-95.

(42)Pitsillides, C. M.; Joe, E. K.; Wei, X.; Anderson, R. R.; Lin, C. P., Selective cell targeting with light-absorbing microparticles and nanoparticles. *Biophys. J.* **2003,** *84*, 4023-32.

(43)Steel, B. C.; McKenzie, D. R.; Bilek, M. M.; Nosworthy, N. J.; dos Remedios, C. G., Nanosecond Responses of Proteins to Ultra-high Temperature Pulses. *Biophys. J.* **2006,** *91*, L66-8.

(44)Takeda, Y.; Kondow, T.; Mafune, F., Degradation of Protein in Nanoplasma Generated Around Gold Nanoparticles in Solution by Laser Irradiation. *J. Phys. Chem. B.* **2006,** *110*, 2393-2397.

(45)Takeda, Y.; Mafuné, F.; Kondow, T., Selective Degradation of Proteins by Laser Irradiation onto Gold Nanoparticles in Solution. *J. Phys. Chem. C* **2009,** *113*, 5027-5030.

(46)Rahmanzadeh, R.; Rundnitzki, F.; Huttmann, G., Two Ways to Inactivate the Ki-67 Protein—Fragmentation by Nanoparticles, Crosslinking with Fluorescent Dyes. *J. Biophotonics.* **2019,** *12*, 12:e201800460.

(47)Urban, A. S.; Fedoruk, M.; Horton, M. R.; Rädler, J. O.; Stefani, F. D.; Feldmann, J., Controlled Nanometric Phase Transitions of Phospholipid Membranes by Plasmonic Heating of Single Gold Nanoparticles. *Nano Lett.* **2009,** *9*, 2903-2908.

(48)Kyrsting, A.; Bendix, P. M.; Stamou, D. G.; Oddershede, L. B., Heat Profiling of Three-Dimensionally Optically Trapped Gold Nanoparticles using Vesicle Cargo Release. *Nano Lett.* **2011,** *11*, 888-892.

(49)Yeheskely-Hayon, D.; Minai, L.; Golan, L.; Dann, E. J.; Yelin, D., Optically Induced Cell Fusion Using Bispecific Nanoparticles. *Small* **2013,** *9*, 3771-3777.

(50)Chen, S.; Weitemier, A. Z.; Zeng, X.; He, L.; Wang, X.; Tao, Y.; Huang, A. J. Y.; Hashimotodani, Y.; Kano, M.; Iwasaki, H.; Parajuli, L. K.; Okabe, S.; Teh, D. B. L.; All, A. H.; Tsutsui-Kimura, I.; Tanaka, K. F.; Liu, X.; McHugh, T. J., Near-Infrared Deep Brain Stimulation via Upconversion Nanoparticle-Mediated Optogenetics. *Science* **2018,** *359*, 679-684.

(51)Cheng, Y.; Chang, Y.; Feng, Y.; Liu, N.; Sun, X.; Feng, Y.; Li, X.; Zhang, H., Simulated Sunlight-Mediated Photodynamic Therapy for Melanoma Skin Cancer by Titanium-Dioxide-Nanoparticle–Gold-Nanocluster–Graphene Heterogeneous Nanocomposites. *Small* **2017,** *13*, 1603935.

(52)Tanabe, T.; Oyamada, M.; Fujita, K.; Dai, P.; Tanaka, H.; Takamatsu, T., Multiphoton Excitation–evoked Chromophore-assisted Laser Inactivation Using Green Fluorescent Protein. *Nat. Methods* **2005,** *2*, 503-505.

(53)Gomez-Santacana, X.; de Munnik, S. M.; Vijayachandran, P.; Da Costa Pereira, D.; Bebelman, J. P. M.; de Esch, I. J. P.; Vischer, H. F.; Wijtmans, M.; Leurs, R., Photoswitching the Efficacy of a Small-Molecule Ligand for a Peptidergic GPCR: from Antagonism to Agonism. *Angew. Chem., Int. Ed. Engl.* **2018,** *57*, 11608-11612.

(54)Lugo, K.; Miao, X.; Rieke, F.; Lin, L. Y., Remote Switching of Cellular Activity and Cell Signaling using Light in Conjunction with Quantum Dots. *Biomedical Optics Express* **2012,** *3*, 447-454.

(55)Xiong, H.; Li, X.; Kang, P.; Perish, J.; Neuhaus, F.; Ploski, J. E.; Kroener, S.; Ogunyankin, M. O.; Shin, J. E.; Zasadzinski, J. A.; Wang, H.; Slesinger, P. A.; Zumbuehl, A.; Qin, Z., Near-infrared Light Triggered-release in Deep Brain Regions Using Ultra-photosensitive Nanovesicles. *Angewandte Chemie International Edition n/a*.

(56)Green, D. E.; Longtin, J. P.; Sitharaman, B., The Effect of Nanoparticle-Enhanced Photoacoustic Stimulation on Multipotent Marrow Stromal Cells. *ACS Nano* **2009,** *3*, 2065-2072.

(57)O'Neal, D. P.; Hirsch, L. R.; Halas, N. J.; Payne, J. D.; West, J. L., Photo-thermal tumor ablation in mice using near infrared-absorbing nanoparticles. *Cancer letters* **2004,** *209*, 171-176.

(58)Hou, X.; Tao, Y.; Pang, Y.; Li, X.; Jiang, G.; Liu, Y., Nanoparticle-Based Photothermal and Photodynamic Immunotherapy for Tumor Treatment. *Int. J. Cancer* **2018,** *143*, 3050-3060.

(59)Nakatsuji, H.; Numata, T.; Morone, N.; Kaneko, S.; Mori, Y.; Imahori, H.; Murakami, T., Thermosensitive Ion Channel Activation in Single Neuronal Cells by Using Surface-Engineered Plasmonic Nanoparticles. *Angew. Chem., Int. Ed. Engl.* **2015,** *54*, 11725-111729.

(60)Carvalho-de-Souza, J. L.; Treger, J. S.; Dang, B.; Kent, S. B.; Pepperberg, D. R.; Bezanilla, F., Photosensitivity of Neurons Enabled by Cell-Targeted Gold Nanoparticles. *Neuron* **2015,** *86*, 207-217.

(61)Fenno, L.; Yizhar, O.; Deisseroth, K., The Development and Application of Optogenetics. *Annu. Rev. Neurosci.* **2011,** *34*, 389-412.

(62)Dolmans, D. E. J. G. J.; Fukumura, D.; Jain, R. K., Photodynamic therapy for cancer. *Nat. Rev. Cancer* **2003,** *3*, 380-387.

(63)Lucky, S. S.; Soo, K. C.; Zhang, Y., Nanoparticles in Photodynamic Therapy. *Chem. Rev. (Washington, DC, U. S.)* **2015,** *115*, 1990-2042.

(64)Jacobson, K.; Rajfur, Z.; Vitriol, E.; Hahn, K., Chromophore-Assisted Laser Inactivation in Cell Biology. *Trends Cell Biol.* **2008,** *18*, 443-450.

(65)Chen, Y.; Li, L.; Chen, W.; Chen, H.; Yin, J., Near-Infrared Small Molecular Fluorescent Dyes for Photothermal Therapy. *Chin. Chem. Lett.* **2019,** *30*, 1353-1360.

(66)Hashida, Y.; Tanaka, H.; Zhou, S.; Kawakami, S.; Yamashita, F.; Murakami, T.; Umeyama, T.; Imahori, H.; Hashida, M., Photothermal Ablation of Tumor Cells using a Single-walled Carbon Nanotube–peptide Composite. *J. Controlled Release* **2014,** *173*, 59-66.

(67)Gao, W.; Sun, Y.; Cai, M.; Zhao, Y.; Cao, W.; Liu, Z.; Cui, G.; Tang, B., Copper Sulfide Nanoparticles as a Photothermal Switch for TRPV1 Signaling to Attenuate Atherosclerosis. *Nat Commun* **2018,** *9*, 231.

(68)Robert, H. M. L.; Savatier, J.; Vial, S.; Verghese, J.; Wattellier, B.; Rigneault, H.; Monneret, S.; Polleux, J.; Baffou, G., Photothermal Control of Heat-Shock Protein Expression at the Single Cell Level. *Small* **2018,** *14*, e1801910.

(69)Kubelka, J., Time-resolved Methods in Biophysics. 9. Laser Temperature-jump Methods for Investigating Biomolecular Dynamics. *Photochem. Photobiol. Sci.* **2009,** *8*, 499-512.

(70)Daggett, V., Protein Folding-simulation. *Chem Rev* **2006,** *106*, 1898-916.

(71)Marks, K. M.; Braun, P. D.; Nolan, G. P., A general approach for chemical labeling and rapid, spatially controlled protein inactivation. *Proc. Natl. Acad. Sci. U. S. A.* **2004,** *101*, 9982-7.

(72)Berndt, A.; Lee, S. Y.; Wietek, J.; Ramakrishnan, C.; Steinberg, E. E.; Rashid, A. J.; Kim, H.; Park, S.; Santoro, A.; Frankland, P. W.; Iyer, S. M.; Pak, S.; Ahrlund-Richter, S.; Delp, S. L.; Malenka, R. C.; Josselyn, S. A.; Carlen, M.; Hegemann, P.; Deisseroth, K., Structural Foundations of Optogenetics: Determinants of Channelrhodopsin Ion Selectivity. *Proc. Natl. Acad. Sci. U. S. A.* **2016,** *113*, 822-9.

(73)Leduc, C.; Si, S.; Gautier, J.; Soto-Ribeiro, M.; Wehrle-Haller, B.; Gautreau, A.; Giannone, G.; Cognet, L.; Lounis, B., A Highly Specific Gold Nanoprobe for Live-cell Single-molecule Imaging. *Nano Lett.* **2013,** *13*, 1489-94.

(74)Cognet, L.; Tardin, C.; Boyer, D.; Choquet, D.; Tamarat, P.; Lounis, B., Single metallic nanoparticle imaging for protein detection in cells. *Proc. Natl. Acad. Sci. U. S. A.* **2003,** *100*, 11350-5.

(75)Nieves, D. J.; Li, Y.; Fernig, D. G.; Levy, R., Photothermal Raster Image Correlation Spectroscopy of Gold Nanoparticles in Solution and on Live Cells. *R Soc Open Sci* **2015,** *2*, 140454.

(76)Thompson, S. A.; Paterson, S.; Azab, M. M.; Wark, A. W.; de la Rica, R., Light-Triggered Inactivation of Enzymes with Photothermal Nanoheaters. *Small* **2017,** *13*, 1603195-1603200.

(77)Berto, P.; Mohamed, M. S. A.; Rigneault, H.; Baffou, G., Time-Harmonic Optical Heating of Plasmonic Nanoparticles. *Phys. Rev. B: Condens. Matter Mater. Phys.* **2014,** *90*, 035439.

(78)Govorov, A. O.; Richardson, H. H., Generating Heat with Metal Nanoparticles. *Nano Today* **2007,** *2*, 30.

(79)Kimling, J.; Maier, M.; Okenve, B.; Kotaidis, V.; Ballot, H.; Plech, A., Turkevich Method for Gold Nanoparticle Synthesis Revisited. *J. Phys. Chem. B* **2006,** *110*, 15700-15707.

(80)Frens, G., Controlled Nucleation for the Regulation of the Particle Size in Monodisperse Gold Suspensions. *Nature Physical Science* **1973,** *241*, 20-22.

(81)Ohta, S.; Glancy, D.; Chan, W. C., DNA-controlled Dynamic Colloidal Nanoparticle Systems for Mediating Cellular Interaction. *Science* **2016,** *351*, 841-5.

(82)Zagorovsky, K. DNA-mediated Gold Nanoparticle Assembly: a Universal Platform for Therapeutic and Diagnostic Applications. Thesis, University of Toronto, 2016.

(83)Rahme, K.; Chen, L.; Hobbs, R. G.; Morris, M. A.; O'Driscoll, C.; Holmes, J. D., PEGylated Gold Nanoparticles: Polymer Quantification as a Function of PEG Lengths and Nanoparticle Dimensions. *RSC Adv.* **2013,** *3*, 6085-6094.

(84)Perry, J. L.; Reuter, K. G.; Kai, M. P.; Herlihy, K. P.; Jones, S. W.; Luft, J. C.; Napier, M.; Bear, J. E.; DeSimone, J. M., PEGylated Print Nanoparticles: The Impact of PEG Density on Protein Binding, Macrophage Association, Biodistribution, and Pharmacokinetics. *Nano Lett.* **2012,** *12*, 5304-5310.

(85)Thobhani, S.; Attree, S.; Boyd, R.; Kumarswami, N.; Noble, J.; Szymanski, M.; Porter, R. A., Bioconjugation and Characterisation of Gold Colloid-labelled Proteins. *J. Immunol. Methods* **2010,** *356*, 60-9.

(86)Kaspar, P.; Moller, G.; Wahlefeld, A., New photometric assay for chymotrypsin in stool. *Clin Chem* **1984,** *30*, 1753-7.

(87)Self, C. H., Enzyme amplification--a general method applied to provide an immunoassisted assay for placental alkaline phosphatase. *J. Immunol. Methods* **1985,** *76*, 389-93.

(88)Chen, Z.; Li, N.; Chen, L.; Lee, J.; Gassensmith, J. J., Dual Functionalized Bacteriophage Qbeta as a Photocaged Drug Carrier. *Small* **2016,** *12*, 4563-71.

(89)Manzenrieder, F.; Luxenhofer, R.; Retzlaff, M.; Jordan, R.; Finn, M. G., Stabilization of Virus-like Particles with Poly(2-oxazoline)s. *Angew Chem Int Ed Engl* **2011,** *50*, 2601-5.

(90)Chen, Z.; Li, N.; Li, S.; Dharmarwardana, M.; Schlimme, A.; Gassensmith, J. J., Viral Chemistry: the Chemical Functionalization of Viral Architectures to Create New Technology. *Wiley Interdiscip Rev Nanomed Nanobiotechnol* **2016,** *8*, 512-34.

(91)Niesen, F. H.; Berglund, H.; Vedadi, M., The Use of Differential Scanning Fluorimetry to Detect Ligand Interactions that Promote Protein Stability. *Nat. Protoc.* **2007,** *2*, 2212-21.

(92)Hirsch, L. R.; Stafford, R. J.; Bankson, J. A.; Sershen, S. R.; Rivera, B.; Price, R. E.; Hazle, J. D.; Halas, N. J.; West, J. L., Nanoshell-Mediated Near-Infrared Thermal Therapy of Tumors Under Magnetic Resonance Guidance. *Proc. Natl. Acad. Sci. U. S. A.* **2003,** *100*, 13549-13554.

(93)Siems, A.; Weber, S. A. L.; Boneberg, J.; Plech, A., Thermodynamics of Nanosecond Nanobubble Formation at Laser-Excited Metal Nanoparticles. *New J. Phys.* **2011,** *13*, 043018.

(94)Carlson, M. T.; Green, A. J.; Richardson, H. H., Superheating water by CW Excitation of Gold Nanodots. *Nano Lett.* **2012,** *12*, 1534-7.

(95)Lukianova-Hleb, E.; Hu, Y.; Latterini, L.; Tarpani, L.; Lee, S.; Drezek, R. A.; Hafner, J. H.; Lapotko, D. O., Plasmonic Nanobubbles as Transient Vapor Nanobubbles Generated around Plasmonic Nanoparticles. *ACS Nano* **2010,** *4*, 2109-2123.

(96)Rodriguez-Oliveros, R.; Sanchez-Gil, J. A., Gold Nanostars as Thermoplasmonic Nanoparticles for Optical Heating. *Opt Express* **2012,** *20*, 621-6.

(97)Yan, C.; Pattani, V.; Tunnell, J. W.; Ren, P., Temperature-induced Unfolding of Epidermal Growth Factor (EGF): Insight from Molecular Dynamics Simulation. *J Mol Graph Model* **2010,** *29*, 2-12.

(98)Chung, H. S.; Khalil, M.; Smith, A. W.; Ganim, Z.; Tokmakoff, A., Conformational changes during the nanosecond-to-millisecond unfolding of ubiquitin. *Proc. Natl. Acad. Sci. U. S. A.* **2005,** *102*, 612-7.

(99)Huttmann, G.; Birngruber, R., On the Possibility of High-Precision Photothermal Microeffects and the Measurement of Fast Thermal Denaturation of Proteins. *IEEE J. Sel. Top. Quant.* **1999,** *5*, 954–962.

(100)Ibrahimkutty, S.; Kim, J.; Cammarata, M.; Ewald, F.; Choi, J.; Ihee, H.; Plech, A., Ultrafast Structural Dynamics of the Photocleavage of Protein Hybrid Nanoparticles. *ACS Nano* **2011,** *5*, 3788-3794.

(101)Erickson, H. P., Size and Shape of Protein Molecules at the Nanometer Level Determined by Sedimentation, Gel Filtration, and Electron Microscopy. *Biol Proced Online* **2009,** *11*, 32-51.

(102)Mafuné, F.; Kohno, J. y.; Takeda, Y.; Kondow, T., Nanoscale Soldering of Metal Nanoparticles for Construction of Higher-Order Structures. *J. Am. Chem. Soc.* **2003,** *125*, 1686.

(103)Matulis, D.; Kranz, J. K.; Salemme, F. R.; Todd, M. J., Thermodynamic Stability of Carbonic Anhydrase: Measurements of Binding Affinity and Stoichiometry Using ThermoFluor. *Biochemistry* **2005,** *44*, 5258-66.

(104)Dominguez-Medina, S.; Kisley, L.; Tauzin, L. J.; Hoggard, A.; Shuang, B.; Indrasekara, A. S. D. S.; Chen, S.; Wang, L.; Derry, P. J.; Liopo, A.; Zubarev, E. R.; Landes, C. F.; Link, S., Adsorption and Unfolding of a Single Protein Triggers Nanoparticle Aggregation. *ACS Nano* **2016,** *10*, 2103-2112.

(105)Mertens, H. D.; Svergun, D. I., Structural Characterization of Proteins and Complexes using Small-angle X-ray Solution Scattering. *J. Struct. Biol.* **2010,** *172*, 128-41.

(106)Cammarata, M.; Levantino, M.; Schotte, F.; Anfinrud, P. A.; Ewald, F.; Choi, J.; Cupane, A.; Wulff, M.; Ihee, H., Tracking the Structural Dynamics of Proteins in Solution using Time-Resolved Wide-angle X-ray Scattering. *Nat. Methods* **2008,** *5*, 881-6.

(107)Arnlund, D.; Johansson, L. C.; Wickstrand, C.; Barty, A.; Williams, G. J.; Malmerberg, E.; Davidsson, J.; Milathianaki, D.; DePonte, D. P.; Shoeman, R. L.; Wang, D.; James, D.; Katona, G.; Westenhoff, S.; White, T. A.; Aquila, A.; Bari, S.; Berntsen, P.; Bogan, M.; van Driel, T. B.; Doak, R. B.; Kjaer, K. S.; Frank, M.; Fromme, R.; Grotjohann, I.; Henning, R.; Hunter, M. S.; Kirian, R. A.; Kosheleva, I.; Kupitz, C.; Liang, M.; Martin, A. V.; Nielsen, M. M.; Messerschmidt, M.; Seibert, M. M.; Sjohamn, J.; Stellato, F.; Weierstall, U.; Zatsepin, N. A.; Spence, J. C.; Fromme, P.; Schlichting, I.; Boutet, S.; Groenhof, G.; Chapman, H. N.; Neutze, R., Visualizing a Protein Quake with Time-resolved X-ray Scattering at a Free-Electron Laser. *Nat. Methods* **2014,** *11*, 923-6.

(108)Percy, A. J.; Rey, M.; Burns, K. M.; Schriemer, D. C., Probing Protein Interactions with Hydrogen/Deuterium Exchange and Mass Spectrometry-a review. *Anal. Chim. Acta* **2012,** *721*, 7-21.

(109)Wang, G.; Kaltashov, I. A., Approach to Characterization of the Higher Order Structure of Disulfide-Containing Proteins Using Hydrogen/Deuterium Exchange and Top-Down Mass Spectrometry. *Anal. Chem.* **2014,** *86*, 7293-7298.

(110)Zhang, Z.; Smith, D. L., Determination of amide hydrogen exchange by mass spectrometry: A new tool for protein structure elucidation. *Protein Sci.* **1993,** *2*, 522-531.

(111)Robinson, M. S.; Sahlender, D. A.; Foster, S. D., Rapid Inactivation of Proteins by Rapamycin-induced Rerouting to Mitochondria. *Dev. Cell* **2010,** *18*, 324-31.

(112)Lin, J. Y.; Sann, S. B.; Zhou, K.; Nabavi, S.; Proulx, C. D.; Malinow, R.; Jin, Y.; Tsien, R. Y., Optogenetic Inhibition of Synaptic Release with Chromophore-assisted Light Inactivation (CALI). *Neuron* **2013,** *79*, 241-53.

(113)Boyden, E. S.; Zhang, F.; Bamberg, E.; Nagel, G.; Deisseroth, K., Millisecond-Timescale, Genetically Targeted Optical Control of Neural Activity. *Nat. Neurosci.* **2005,** *8*, 1263-1268.

(114)Muir, J.; Lopez, J.; Bagot, R. C., Wiring the Depressed Brain: Optogenetic and Chemogenetic Circuit Interrogation in Animal Models of Depression. *Neuropsychopharmacology* **2018,** *44*, 1013-1026.

(115)Bulina, M. E.; Chudakov, D. M.; Britanova, O. V.; Yanushevich, Y. G.; Staroverov, D. B.; Chepurnykh, T. V.; Merzlyak, E. M.; Shkrob, M. A.; Lukyanov, S.; Lukyanov, K. A., A Genetically Encoded Photosensitizer. *Nat. Biotechnol.* **2006,** *24*, 95-99.

(116)Jay, D. G., Selective Distruction of Protein Function by Chromophore-Assisted Laser Inactivation. *Proc. Natl. Acad. Sci. U. S. A.* **1988,** *85*, 5454-5458.

(117)Fehrentz, T.; Huber, F. M. E.; Hartrampf, N.; Bruegmann, T.; Frank, J. A.; Fine, N. H. F.; Malan, D.; Danzl, J. G.; Tikhonov, D. B.; Sumser, M.; Sasse, P.; Hodson, D. J.; Zhorov, B. S.; Klocker, N.; Trauner, D., Optical Control of L-Type Ca^{2+} Channels Using a Diltiazem Photoswitch. *Nat. Chem. Biol.* **2018,** *14*, 764-767.

(118)Ali, M. R. K.; Wu, Y.; Tang, Y.; Xiao, H.; Chen, K.; Han, T.; Fang, N.; Wu, R.; El-Sayed, M. A., Targeting Cancer Cell Integrins Using Gold Nanorods in Photothermal Therapy Inhibits Migration Through Affecting Cytoskeletal Proteins. *Proc. Natl. Acad. Sci. U. S. A.* **2017,** *114*, E5655-E5663.

(119)Jiang, W.; Kim, B. Y.; Rutka, J. T.; Chan, W. C., Nanoparticle-Mediated Cellular Response Is Size-Dependent. *Nat. Nanotechnol.* **2008,** *3*, 145-150.

(120)Dennison, J. M.; Zupancic, J. M.; Lin, W.; Dwyer, J. H.; Murphy, C. J., Protein Adsorption to Charged Gold Nanospheres as a Function of Protein Deformability. *Langmuir* **2017,** *33*, 7751-7761.

(121)Huang, H.; Delikanli, S.; Zeng, H.; Ferkey, D. M.; Pralle, A., Remote Control of Ion Channels and Neurons through Magnetic-Field Heating of Nanoparticles. *Nat. Nanotechnol.* **2010,** *5*, 602-606.

(122)Chen, R.; Romero, G.; Christiansen, M. G.; Mohr, A.; Anikeeva, P., Wireless Magnetothermal Deep Brain Stimulation. *Science* **2015,** *347*, 1477-1480.

(123)Rojas, C.; Tedesco, M.; Massobrio, P.; Marino, A.; Ciofani, G.; Martinoia, S.; Raiteri, R., Acoustic Stimulation can Induce a Selective Neural Network Response Mediated by Piezoelectric Nanoparticles. *J. Neural. Eng.* **2018,** *15*, 036016.

(124)Miller, I. C.; Gamboa Castro, M.; Maenza, J.; Weis, J. P.; Kwong, G. A., Remote Control of Mammalian Cells with Heat-Triggered Gene Switches and Photothermal Pulse Trains. *ACS Synth. Biol.* **2018,** *7*, 1167-1173.

(125)Yoo, S.; Hong, S.; Choi, Y.; Park, J.; Nam, Y., Photothermal Inhibition of Neural Activity with Near-Infrared Sensitive Nanotransducers. *ACS Nano* **2014,** *8*, 8040-8049.

(126)Paviolo, C.; Haycock, J. W.; Cadusch, P. J.; McArthur, S. L.; Stoddart, P. R., Laser Exposure of Gold Nanorods Can Induce Intracellular Calcium Transients. *J. Biophotonics.* **2014,** *7*, 761-765.

(127)de Boer, W. D. A. M.; Hirtz, J. J.; Capretti, A.; Gregorkiewicz, T.; Izquierdo-Serra, M.; Han, S.; Dupre, C.; Shymkiv, Y.; Yuste, R., Neuronal Photoactivation through Second-Harmonic Near-Infrared Absorption by Gold Nanoparticles. *Light: Sci. Appl.* **2018,** *7*, 100.

(128)Maier, C. M.; Huergo, M. A.; Milosevic, S.; Pernpeintner, C.; Li, M.; Singh, D. P.; Walker, D.; Fischer, P.; Feldmann, J.; Lohmueller, T., Optical and Thermophoretic Control of Janus Nanopen Injection into Living Cells. *Nano Lett.* **2018,** *18*, 7935-7941.

(129)Li, X.; Kang, P.; Chen, Z.; Lal, S.; Zhang, L.; Gassensmith, J. J.; Qin, Z., Rock the Nucleus: Significantly Enhanced Nuclear Membrane Permeability and Gene Transfection by Plasmonic Nanobubble Induced Nanomechanical Transduction. *Chem. Commun. (Cambridge, U. K.)* **2018,** *54*, 2479-2482.

(130)Anderson, R. R.; Parrish, J. A., Selective Photothermolysis: Precise Microsurgery by Selective Absorption of Pulsed Radiation. *Science* **1983,** *220*, 524-527.

(131)Kang, P.; Chen, Z.; Nielsen, S. O.; Hoyt, K.; D'Arcy, S.; Gassensmith, J. J.; Qin, Z., Molecular Hyperthermia: Spatiotemporal Protein Unfolding and Inactivation by Nanosecond Plasmonic Heating. *Small* **2017,** *13*, 1700841-1700847.

(132)Tillu, D. V.; Hassler, S. N.; Burgos-Vega, C. C.; Quinn, T. L.; Sorge, R. E.; Dussor, G.; Boitano, S.; Vagner, J.; Price, T. J., Protease-Activated Receptor 2 Activation Is Sufficient to Induce the Transition to a Chronic Pain State. *Pain* **2015,** *156*, 859-867.

(133)Boitano, S.; Hoffman, J.; Flynn, A. N.; Asiedu, M. N.; Tillu, D. V.; Zhang, Z.; Sherwood, C. L.; Rivas, C. M.; DeFea, K. A.; Vagner, J.; Price, T. J., The Novel PAR2 Ligand C391 Blocks Multiple PAR2 Signalling Pathways *In Vitro* and *In Vivo*. *Br. J. Pharmacol.* **2015,** *172*, 4535-4545.

(134)Giannotta, M.; Benedetti, S.; Tedesco, F. S.; Corada, M.; Trani, M.; D'Antuono, R.; Millet, Q.; Orsenigo, F.; Galvez, B. G.; Cossu, G.; Dejana, E., Targeting Endothelial Junctional Adhesion Molecule-A/ EPAC/ Rap-1 Axis as a Novel Strategy to Increase Stem Cell Engraftment in Dystrophic Muscles. *EMBO Mol. Med.* **2014,** *6*, 239-258.

(135)Dejana, E., Endothelial Cell-Cell Junctions: Happy Together. *Nat. Rev. Mol. Cell Biol.* **2004,** *5*, 261-270.

(136)Baffou, G.; Quidant, R., Thermo-Plasmonics: Using Metallic Nanostructures as Nano-Sources of Heat. *Laser Photonics Rev.* **2012,** *7*, 171-187.

(137)Muller, A.; Joseph, V.; Slesinger, P. A.; Kleinfeld, D., Cell-Based Reporters Reveal *In Vivo* Dynamics of Dopamine and Norepinephrine Release in Murine Cortex. *Nat. Methods* **2014,** *11*, 1245-1252.

(138)Boitano, S.; Flynn, A. N.; Schulz, S. M.; Hoffman, J.; Price, T. J.; Vagner, J., Potent Agonists of the Protease Activated Receptor 2 (PAR2). *J. Med. Chem.* **2011,** *54*, 1308-1313.

(139)Chattopadhyay, N.; Cai, Z.; Pignol, J. P.; Keller, B.; Lechtman, E.; Bendayan, R.; Reilly, R. M., Design and Characterization of HER-2-Targeted Gold Nanoparticles for Enhanced X-Radiation Treatment of Locally Advanced Breast Cancer. *Mol. Pharmaceutics* **2010,** *7*, 2194-2206.

(140)Moy, J. K.; Khoutorsky, A.; Asiedu, M. N.; Black, B. J.; Kuhn, J. L.; Barragan-Iglesias, P.; Megat, S.; Burton, M. D.; Burgos-Vega, C. C.; Melemedjian, O. K.; Boitano, S.; Vagner, J.; Gkogkas, C. G.; Pancrazio, J. J.; Mogil, J. S.; Dussor, G.; Sonenberg, N.; Price, T. J., The MNK-eIF4E Signaling Axis Contributes to Injury-Induced Nociceptive Plasticity and the Development of Chronic Pain. *J. Neurosci.* **2017,** *37*, 7481-7499.

(141)Schindelin, J.; Arganda-Carreras, I.; Frise, E.; Kaynig, V.; Longair, M.; Pietzsch, T.; Preibisch, S.; Rueden, C.; Saalfeld, S.; Schmid, B.; Tinevez, J. Y.; White, D. J.; Hartenstein, V.; Eliceiri, K.; Tomancak, P.; Cardona, A., Fiji: An Open-Source Platform for Biological-Image Analysis. *Nat. Methods* **2012,** *9*, 676-682.

(142)Plech, A.; Kotaidis, V.; Gresillon, S.; Dahmen, C.; von Plessen, G., Laser-Induced Heating and Melting of Gold Nanoparticles Studied by Time-Resolved X-Ray Scattering. *Phys. Rev. B* **2004,** *70*, 195423.

(143)Daw, M. S.; Baskes, M. I., Embedded-Atom Method: Derivation and Application to Impurities, Surfaces, and Other Defects in Metals. *Phys. Rev. B* **1984,** *29*, 6443-6453.

(144)MacKerell, A. D.; Bashford, D.; Bellott, M.; Dunbrack, R. L.; Evanseck, J. D.; Field, M. J.; Fischer, S.; Gao, J.; Guo, H.; Ha, S.; Joseph-McCarthy, D.; Kuchnir, L.; Kuczera, K.; Lau, F. T.; Mattos, C.; Michnick, S.; Ngo, T.; Nguyen, D. T.; Prodhom, B.; Reiher, W. E.; Roux, B.; Schlenkrich, M.; Smith, J. C.; Stote, R.; Straub, J.; Watanabe, M.; Wiorkiewicz-Kuczera, J.; Yin, D.; Karplus, M., All-Atom Empirical Potential for Molecular Modeling and Dynamics Studies of Proteins. *J. Phys. Chem. B* **1998,** *102*, 3586-3616.

(145)Bohren, C. F.; Huffman, D. R., *Absorption and Scattering of Light by Small Particles*. John Wiley & Sons, Inc: New York, 1983.

(146)Dai, Y.; Wang, S.; Tominaga, M.; Yamamoto, S.; Fukuoka, T.; Higashi, T.; Kobayashi, K.; Obata, K.; Yamanaka, H.; Noguchi, K., Sensitization of TRPA1 by PAR2 Contributes to the Sensation of Inflammatory Pain. *J. Clin. Invest.* **2007,** *117*, 1979-1987.

(147)Amadesi, S.; Cottrell, G. S.; Divino, L.; Chapman, K.; Grady, E. F.; Bautista, F.; Karanjia, R.; Barajas-Lopez, C.; Vanner, S.; Vergnolle, N.; Bunnett, N. W., Protease-activated Receptor 2 Sensitizes TRPV1 by Protein Kinase Cepsilon- and a Dependent Mechanisms in Rats and Mice. *J. Physiol.* **2006,** *575*, 555-571.

(148)Hazan, A.; Kumar, R.; Matzner, H.; Priel, A., The Pain Receptor TRPV1 Displays Agonist-Dependent Activation Stoichiometry. *Sci. Rep.* **2015,** *5*, 12278.

(149)Suen, J. Y.; Gardiner, B.; Grimmond, S.; Fairlie, D. P., Profiling Gene Expression Induced by Protease-Activated Receptor 2 (PAR2) Activation in Human Kidney Cells. *PLoS One* **2010,** *5*, e13809.

(150)Vetter, I.; Lewis, R. J., Characterization of Endogenous Calcium Responses in Neuronal Cell Lines. *Biochem. Pharmacol.* **2010,** *79*, 908-920.

(151)Lacin, E.; Muller, A.; Fernando, M.; Kleinfeld, D.; Slesinger, P. A., Construction of Cell-based Neurotransmitter Fluorescent Engineered Reporters (CNiFERs) for Optical Detection of Neurotransmitters *In Vivo*. *J. Vis. Exp.* **2016**, e53290.

(152)Jain, P. K.; Lee, K. S.; El-Sayed, I. H.; El-Sayed, M. A., Calculated Absorption and Scattering Properties of Gold Nanoparticles of Different Size, Shape, and Composition: Applications in Biological Imaging and Biomedicine. *J. Phys. Chem. B* **2006,** *110*, 7238-7248.

(153)Fales, A. M.; Vogt, W. C.; Pfefer, J.; Ilev, I. K., Size-Dependent Thresholds for Melting and Nanobubble Generation Using Pulsed-Laser Irradiated Gold Nanoparticles. *Proc. SPIE* **2019,** *10509*, 105090C.

(154)Vergnolle, N.; Bunnett, N. W.; Sharkey, K. A.; Brussee, V.; Compton, S. J.; Grady, E. F.; Cirino, G.; Gerard, N.; Basbaum, A. I.; Andrade-Gordon, P.; Hollenberg, M. D.; Wallace, J. L., Proteinase-Activated Receptor-2 and Hyperalgesia: A Novel Pain Pathway. *Nat. Med. (N. Y., NY, U. S.)* **2001,** *7*, 821-826.

(155)Goodman, A. M.; Hogan, N. J.; Gottheim, S.; Li, C.; Clare, S. E.; Halas, N. J., Understanding Resonant Light-Triggered DNA Release from Plasmonic Nanoparticles. *ACS Nano* **2017,** *11*, 171-179.

(156)Davis, A. A.; Farrar, M. J.; Nishimura, N.; Jin, M. M.; Schaffer, C. B., Optoporation and Genetic Manipulation of Cells Using Femtosecond Laser Pulses. *Biophys. J.* **2013,** *105*, 862-871.

(157)Xiong, R.; Raemdonck, K.; Peynshaert, K.; Lentacker, I.; De Cock, I.; Demeester, J.; De Smedt, S. C.; Skirtach, A. G.; Braeckmans, K., Comparison of Gold Nanoparticle Mediated Photoporation: Vapor Nanobubbles Outperform Direct Heating for Delivering Macromolecules in Live Cells. *ACS Nano* **2014,** *8*, 6288-6296.

(158)Yao, C.; Rudnitzki, F.; Huttmann, G.; Zhang, Z.; Rahmanzadeh, R., Important Factors for Cell-Membrane Permeabilization by Gold Nanoparticles Activated by Nanosecond-Laser Irradiation. *Int. J. Nanomed.* **2017,** *12*, 5659-5672.

(159)Chen, X.; Munjiza, A.; Zhang, K.; Wen, D., Molecular Dynamics Simulation of Heat Transfer from a Gold Nanoparticle to a Water Pool. *J. Phys. Chem. C* **2014,** *118*, 1285-1293.

(160)Sarkar, D.; Kang, P.; Nielsen, S. O.; Qin, Z., Non-Arrhenius Reaction-Diffusion Kinetics for Protein Inactivation over a Large Temperature Range. *ACS Nano* **2019,** *13*, 8669-8679.

(161)Mayor, U.; Guydosh, N. R.; Johnson, C. M.; Grossmann, J. G.; Sato, S.; Jas, G. S.; Freund, S. M.; Alonso, D. O.; Daggett, V.; Fersht, A. R., The Complete Folding Pathway of a Protein from Nanoseconds to Microseconds. *Nature* **2003,** *421*, 863-867.

(162)Huang, Y. C.; Lei, K. F.; Liaw, J. W.; Tsai, S. W., The Influence of Laser Intensity Activated Plasmonic Gold Nanoparticle-Generated Photothermal Effects on Cellular Morphology and Viability: a Real-Time, Long-Term Tracking and Monitoring System. *Photochem. Photobiol. Sci.* **2019,** *18*, 1419-1429.

(163)Arita, Y.; Ploschner, M.; Antkowiak, M.; Gunn-Moore, F.; Dholakia, K., Laser-Induced Breakdown of an Optically Trapped Gold Nanoparticle for Single Cell Transfection. *Opt. Lett.* **2013,** *38*, 3402-3405.

(164)Johannsmeier, S.; Heeger, P.; Terakawa, M.; Kalies, S.; Heisterkamp, A.; Ripken, T.; Heinemann, D., Gold Nanoparticle-Mediated Laser Stimulation Induces a Complex Stress Response in Neuronal Cells. *Sci. Rep.* **2018,** *8*, 6533.

(165)Kalies, S.; Antonopoulos, G. C.; Rakoski, M. S.; Heinemann, D.; Schomaker, M.; Ripken, T.; Meyer, H., Investigation of Biophysical Mechanisms in Gold Nanoparticle Mediated Laser Manipulation of Cells Using a Multimodal Holographic and Fluorescence Imaging Setup. *PLoS One* **2015,** *10*, e0124052.

(166)Burrows, N. D.; Harvey, S.; Idesis, F. A.; Murphy, C. J., Understanding the Seed-Mediated Growth of Gold Nanorods through a Fractional Factorial Design of Experiments. *Langmuir* **2017,** *33*, 1891-1907.

(167)Wu, Y.; Ali, M. R. K.; Dong, B.; Han, T.; Chen, K.; Chen, J.; Tang, Y.; Fang, N.; Wang, F.; El-Sayed, M. A., Gold Nanorod Photothermal Therapy Alters Cell Junctions and Actin Network in Inhibiting Cancer Cell Collective Migration. *ACS Nano* **2018,** *12*, 9279-9290.

(168)Scarabelli, L.; Sanchez-Iglesias, A.; Perez-Juste, J.; Liz-Marzan, L. M., A "Tips and Tricks" Practical Guide to the Synthesis of Gold Nanorods. *J. Phys. Chem. Lett.* **2015,** *6*, 4270-4279.

(169)Brink, C. B.; Harvey, B. H.; Bodenstein, J.; Venter, D. P.; Oliver, D. W., Recent Advances in Drug Action and Therapeutics: Relevance of Novel Concepts in G-Protein-Coupled Receptor and Signal Transduction Pharmacology. *Br. J. Clin. Pharmacol.* **2004,** *57*, 373-87.

(170)Bale, S. S.; Kwon, S. J.; Shah, D. A.; Banerjee, A.; Dordick, J. S.; Kane, R. S., Nanoparticle-Mediated Cytoplasmic Delivery of Proteins to Target Cellular Machinery. *ACS Nano* **2010,** *4*, 1493-1500.

(171)Miersch, S.; Sidhu, S. S., Intracellular Targeting with Engineered Proteins. *F1000Research* **2016,** *5*, 1-12.

(172)Gopinath, S. C.; Lakshmipriya, T.; Chen, Y.; Arshad, M. K.; Kerishnan, J. P.; Ruslinda, A. R.; Al-Douri, Y.; Voon, C. H.; Hashim, U., Cell-Targeting Aptamers Act as Intracellular Delivery Vehicles. *Appl. Microbiol. Biotechnol.* **2016,** *100*, 6955-6969.

(173)Herce, H. D.; Schumacher, D.; Schneider, A. F. L.; Ludwig, A. K.; Mann, F. A.; Fillies, M.; Kasper, M. A.; Reinke, S.; Krause, E.; Leonhardt, H.; Cardoso, M. C.; Hackenberger, C. P. R.,

Cell-Permeable Nanobodies for Targeted Immunolabelling and Antigen Manipulation in Living Cells. *Nature Chem.* **2017,** *9*, 762-771.

(174)Mandal, S.; Debnath, K.; Jana, N. R.; Jana, N. R., Trehalose-Functionalized Gold Nanoparticle for Inhibiting Intracellular Protein Aggregation. *Langmuir* **2017,** *33*, 13996-14003.

(175)Hoorens, M. W. H., Szymanski, W., Reversible, Spatial and Temporal Control over Protein Activity Using Light. *Trends Biochem. Sci.* **2019,** *43*, 567-575.

(176)Kim, C. K.; Adhikari, A.; Deisseroth, K., Integration of Optogenetics with Complementary Methodologies in Systems Neuroscience. *Nat. Rev. Neurosci.* **2017,** *18*, 222-235.

(177)Huang, H.; Delikanli, S.; Zeng, H.; Ferkey, D. M.; Pralle, A., Remote Control of ion Channels and Neurons through Magnetic-field Heating of Nanoparticles. *Nat. Nanotechnol.* **2010,** *5*, 602-6.

(178)Ma, X.; Xiong, Y.; Lee, L. T. O., Application of Nanoparticles for Targeting G Protein-Coupled Receptors. *Int J Mol Sci* **2018,** *19*.

(179)Hartland, G. V., Optical Studies of Dynamics in Noble Metal Nanostructures. *Chem Rev* **2011,** *111*, 3858-87.

(180)Paviolo, C.; Stoddart, P. R., Gold Nanoparticles for Modulating Neuronal Behavior. *Nanomaterials (Basel)* **2017,** *7*.

(181)Lavoie-Cardinal, F.; Salesse, C.; Bergeron, E.; Meunier, M.; De Koninck, P., Gold Nanoparticle-Assisted All Optical Localized Stimulation and Monitoring of Ca^{2+} Signaling in Neurons. *Sci Rep* **2016,** *6*, 20619.

(182)Hu, M.; Hartland, G. V., Heat Dissipation for Au Particles in Aqueous Solution: Relaxation Time versus Size. **2002**.

(183)Yakunin, A. N.; Avetisyan, Y. A.; Tuchin, V. V., Quantification of Laser Local Hyperthermia Induced by Gold Plasmonic Nanoparticles. *J. Biomed. Opt.* **2015,** *20*, 051030.

(184)Kang, P.; Li, X.; Liu, Y.; Shiers, S. I.; Xiong, H.; Giannotta, M.; Dejana, E.; Price, T. J.; Randrianalisoa, J.; Nielsen, S. O.; Qin, Z., Transient Photoinactivation of Cell Membrane Protein Activity without Genetic Modification by Molecular Hyperthermia. *ACS Nano* **2019,** *13*, 12487-12499.

(185)Dagallier, A.; Boulais, E.; Boutopoulos, C.; Lachaine, R.; Meunier, M., Multiscale Modeling of Plasmonic Enhanced Energy Transfer and Cavitation around Laser-Excited Nanoparticles. *Nanoscale* **2017,** *9*, 3023-3032.

(186)Goldenberg, H.; Tranter, C. J., Heat flow in an infinite medium heated by a sphere. *British journal of applied physics* **1952,** *3*, 296-298.

(187)Wagner, W.; Kretzschmar, H.-J., *International Steam Tables-Properties of Water and Steam Based on the Industrial Formulation IAPWS-IF97*. Springer-Verlag: Berlin/Heidelberg, 2008.

(188)Wilson, O. M.; Hu, X.; Cahill, D. G.; Braun, P. V., Colloidal metal particles as probes of nanoscale thermal transport in fluids. *Phys. Rev. B: Condens. Matter Mater. Phys.* **2002,** *66*, 224301.

(189)Ge, Z.; Cahill, D. G.; Braun, P. V., AuPd Metal Nanoparticles as Probes of Nanoscale Thermal Transport in Aqueous Solution. *J. Phys. Chem. B* **2004,** *108*, 18870-18875.

(190)Ge, Z.; Cahill, D. G.; Braun, P. V., Thermal Conductance of Hydrophilic and Hydrophobic Interfaces. *Phys. Rev. Lett.* **2006,** *96*, 186101.

(191)Schmidt, A. J.; Alper, J. D.; Chiesa, M.; Das, S. K.; Hamad-Schifferli, K., Probing the Gold Nanorod−Ligand−Solvent Interface by Plasmonic Absorption and Thermal Decay. *J. Phys. Chem. C* **2008,** *112*, 13320-13323.

(192)Merabia, S.; Shenogin, S.; Joly, L.; Keblinski, P.; Barrat, J. L., Heat Transfer from Nanoparticles: a Corresponding State Analysis. *Proc. Natl. Acad. Sci. U. S. A.* **2009,** *106*, 15113-8.

(193)Losego, M. D.; Grady, M. E.; Sottos, N. R.; Cahill, D. G.; Braun, P. V., Effects of Chemical Bonding on Heat Transport across Interfaces. *Nat. Mater.* **2012,** *11*, 502-6.

(194)Park, J.; Huang, J.; Wang, W.; Murphy, C. J.; Cahill, D. G., Heat Transport between Au Nanorods, Surrounding Liquids, and Solid Supports. *J. Phys. Chem. C* **2012,** *115*, 26335-26341.

(195)Harikrishna, H.; Ducker, W. A.; Huxtable, S. T., The Influence of Interface Bonding on Thermal Transport through Solid–liquid Interfaces. *Appl. Phys. Lett.* **2013,** *102*, 251606.

(196)Wu, X.; Ni, Y.; Zhu, J.; Burrows, N. D.; Murphy, C. J.; Dumitrica, T.; Wang, X., Thermal Transport across Surfactant Layers on Gold Nanorods in Aqueous Solution. *ACS Appl. Mater. Interfaces* **2016,** *8*, 10581-9.

(197)Wei, X.; Zhang, T.; Luo, T., Thermal Energy Transport across Hard–Soft Interfaces. *ACS Energy Letters* **2017,** *2*, 2283-2292.

(198)Huxtable, S. T.; Cahill, D. G.; Shenogin, S.; Xue, L.; Ozisik, R.; Barone, P.; Usrey, M.; Strano, M. S.; Siddons, G.; Shim, M.; Keblinski, P., Interfacial heat flow in carbon nanotube suspensions. *Nat. Mater.* **2003,** *2*, 731-4.

(199)Font, F.; Myers, T. G., Spherically Symmetric Nanoparticle Melting with a Variable Phase Change Temperature. *Journal of Nanoparticle Research* **2013,** *15*, 2086-2099.

(200)Chen, X.; Munjiza, A.; Zhang, K.; Wen, D., Molecular Dynamics Simulation of Heat Transfer from a Gold Nanoparticle to a Water Pool. *J. Phys. Chem. C* **2014,** *118*, 1285-1293.

(201)Piana, S.; Lindorff-Larsen, K.; Shaw, D. E., Protein Folding Kinetics and Thermodynamics from Atomistic Simulation. *Proc. Natl. Acad. Sci. U. S. A.* **2012,** *109*, 17845-50.

(202)Plech, A.; Kotaidis, V.; Grésillon, S.; Dahmen, C.; von Plessen, G., Laser-Induced Heating and Melting of Gold Nanoparticles Studied by Time-Resolved X-ray Scattering. *Phys. Rev. B: Condens. Matter Mater. Phys.* **2004,** *70*, 195423.

(203)Takami, A.; Kurita, H.; Koda, S., Laser-Induced Size Reduction of Noble Metal Particles. *The Journal of Physical Chemistry B* **1999,** *103*, 1226-1232.

(204)Kucsko, G.; Maurer, P. C.; Yao, N. Y.; Kubo, M.; Noh, H. J.; Lo, P. K.; Park, H.; Lukin, M. D., Nanometre-scale Thermometry in a Living Cell. *Nature* **2013,** *500*, 54-58.

(205)Ziefuss, A. R.; Reich, S.; Reichenberger, S.; Levantino, M.; Plech, A., *In Situ* Structural Kinetics of Picosecond Laser-Induced Heating and Fragmentation of Colloidal Gold Spheres. *Phys. Chem. Chem. Phys.* **2020,** *22*, 4993-5001.

(206)Baffou, G.; Bordacchini, I.; Baldi, A.; Quidant, R., Simple Experimental Proceduces to Discern Photothermal Processes in Plasmon-Driven Chemistry. *arXiv* **2020,** *2001*, 08402.

BIOGRAPHICAL SKETCH

Peiyuan Kang was born and raised in Xi'an, China. Prior to arriving to U.S., he earned a bachelor's degree in engineering at Harbin Engineering University with a focus on thermal energy and power engineering. In 2014, Peiyuan entered The University of Texas at Dallas to pursue his master's degree in Mechanical Engineering. In 2015, he joined in Dr. Zhenpeng Qin's lab as a PhD student. During his PhD studies, Peiyuan has been exposed to various research frontiers in the fields of nanotechnology and biomedical sciences. Peiyuan is interested in understanding the interaction between metal nanostructures and biological systems. He spends much of his free time watching movies, cooking Chinese food and playing the violin.

CURRICULUM VITAE

Peiyuan (Alvin) Kang

Peiyuan.Kang@utdallas.edu
(972)595-4284
UTDallas Mechanical Engineering
800 West Campbell Rd. BSB 13.816

EDUCATION

The University of Texas at Dallas — **Richardson, TX**
Doctor of Science in Mechanical Engineering — *06. 2015 – 05. 2020 (expected)*
Advisor: Dr. Zhenpeng Qin
GPA: 3.734

The University of Texas at Dallas — **Richardson, TX**
Master of Science in Mechanical Engineering — *06. 2014 – 05. 2016*
GPA: 3.7

Harbin Engineering University — **Harbin, China**
Bachelor of Engineering in Mechanical Engineering — *06. 2010 – 05. 2014*
GPA: 3.3

REPRESENTATIVE PUBLICATIONS

1. **Kang, P.**, Li, X., Shiers, I.S., Xiong, H., Giannotta, M., Dejana, E., Price, T.J., Randrianalisoa, J., Nielsen, S.O., Qin, Z., "Transient Photoinactivation of Cell Membrane Protein Activity without Genetic Modification by Molecular Hyperthermia", **ACS Nano**, 2019, 13, 11, 12487.
2. **Kang, P.**, Chen, Z., Nielsen, S.O., Hoyt, K., D'Arcy, S., Gassensmith, J.J., Qin, Z., **"**Molecular Hyperthermia: Spatiotemporal Protein Unfolding and Inactivation by Nanosecond Plasmonic Heating", **Small**, 2017, 13 (36), 1700841.
3. Sarkar, D. †, **Kang, P.†**, Nielsen, S.O., and Qin, Z., "Non-Arrhenius Reaction-Diffusion Kinetics for Protein Unfolding and Inactivation over a Large," **ACS Nano**, 2019, 13, 8, 8669. **(† co-first authors).**
4. Godakhindi, V.S. †, **Kang, P. †**, Serre, M†., Revuru, N.A., Zou, J.M., Roner, M. R., Levitz, R., Kahn, J. S., Randrianalisoa, J., Qin, Z., "Tuning the Gold Nanoparticle Colorimetric Assay by Nanoparticle Size, Concentration, and Size Combinations for Oligonucleotide Detection", **ACS Sensors**, 2017, 2 (11), 1627. **(† co-first authors)**
5. Xiong, H., Li, X., **Kang, P.**, Perish, J., Neuhaus, F., Ploski, J. E., Kroener, S., Ogunyankin, M. O., Shin, J., Zasadzinski, J. A., Wang, H., Slesinger, P. A., Zumbuehl, A., Qin, Z., "Near-infrared Light Triggered-release in Deep Brain Regions Using Ultra-photosensitive Nanovesicles", **Angew. Chem. Int. Ed.**, 2020, Accepted.
6. Benjamin, C.E., Chen, Z., **Kang, P.,** Wilson, B.A., Li, N., Nielsen, S.O., Qin, Z., Gassensmith, J.J., "Site-Selective Nucleation and Size Control of Gold Nanoparticle Photothermal Antennae on the Pore Structure of a Virus", **J. Am. Chem. Soc.**, 2018, 140 (49), 17226.
7. Li, X., **Kang, P.,** Chen, Z., Lal, S., Zhang, L., Gassensmith, J. J., Qin, Z., "Rock the Nucleus: Significantly Enhanced Nuclear Membrane Permeability and Gene Transfection by Plasmonic Nanobubble Induced Nanomechanical Transduction", **Chem. Commun.** 2018, 54 (20), 2479.
8. Karim, M.R., Li, X., **Kang P.,** Randrianalisoa, J., Qin, Z., and Qian, D., "Ultrafast Pulsed Laser Induced Nanocrystal Transformation in Colloidal Plasmonic Vesicles", **Adv. Optical Mater.** 2018, 6, 1800726.

MANUSCRIPT SUBMITTED OR IN PREPARATION

1. **Kang, P.†,** Xie, C. †, Fall, O., Randrianalisoa, J., and Qin, Z., "Computational Investigation of Protein Photoinactivation by Molecular Hyperthermia", **J. Biomech. Eng.** 2020, in submission. († co-first authors)
2. **Kang, P.,** Xie, C., Dawkrajai, N., and Qin, Z., "Picosecond Laser Induced Fragmentation of Plasmonic Gold Nanoparticles: Coulomb Explosion *versus* Photothermal evaporation", in preparation.
3. **Kang, P.,** Youn, J., Liu, Y., Wilson, B. A., and Qin, Z., "Mechanism of Enhanced Thermal Transport and Photoacoustic Effect of Gold Nanoparticle by Silica Coating", in preparation.

RESEARCH EXPERIENCE

The University of Texas at Dallas – Research assistant **Richardson, TX**

Project 1 – Molecular hyperthermia *06. 2015 – Present*

Significance: Invented and examined a novel method to inactivate proteins of interest with great accuracy both in solution and in live cells.

- Led the project and collaborated with three research groups (Dr. Jeremiah Gassensmith, Dr. Steven Nielsen and Dr. Theodore Price)
- Developed a protocol to conjugate 6 proteins including antibodies on gold nanoparticles with good stability.
- Designed and constructed a laser optical setup.
- Discovered the feasibility of using CNiFERs cell model to study protease activated receptor 2 (PAR2) activity. Made the experiment much easier and cheaper.
- Demonstrated nanosecond plasmonic heating of plasmonic nanoparticles can be used to inactivate PAR2 on live cells with great accuracy.
- Published 3 peer-reviewed papers in high impact journals as either first author or co-first author.
- Presented the project at 3 conferences.

Project 2 – Point-of-care diagnosis by nanoparticle aggregation *03. 2015 – 08. 2017*

Significance: Provided a guideline to design POC devices to meet the signal and sensitivity needs for infectious disease diagnosis and other applications.

- Developed a colorimetric diagnostic assay using gold nanoparticle to detect DNA target from malaria.
- Investigated gold nanoparticle size and concentration effects.
- Improved the assay performance.
- Presented the project at 1 conference. 1 peer-reviewed paper is published in high impact journal.

Project 3 – Computational simulation of molecular hyperthermia *06. 2017 – Present*

Significance: Developed a computational framework to interpret protein inactivation by molecular hyperthermia. Provided a method to investigate thermal effect in photo enhanced chemical reactions.

- Solved and programmed the analytical solution in MATLAB.
- Built a numerical model in COMSOL Multiphysics.
- Mentored and trained 2 graduate students.
- Presented the project at 1 conference. 1 paper is in submission.

Project 4 – Particle fragmentation under short laser pulses *06. 2018 – Present*

Significance: Provided a guide to design nanostructures with better laser stability.

- Developed a super sensitive method to analyze UV-vis spectrum and detect the fragmentation of gold nanoparticles with MATLAB.
- Investigated the fragmentation of gold nanoparticles induced by nanosecond and picosecond laser.
- Developed a two-temperature based numerical model to study the particle fragmentation with COMSOL.
- Presented the project at 1 conference. 1 paper is in preparation.

TEACHING EXPERIENCE

UTD – Teaching assistant **Richardson, TX**

Course 1 – Conductive & Radiative Heat Transfer (graduate level) *08. 2015 – 12. 2015*

- Organized discussion sessions for students every week.
- Developed course homework answers and graded students' homework.
- Gave a presentation for class on special topic area.

Course 2 – Heat Transfer *01. 2016 – 06. 2016*
Course 3 – Thermodynamics *07. 2017 – 12. 2017*

- Taught weekly problem practice session for 50 undergraduate students.
- Graded students' homework.

SKILLS

Nanomaterials

- Electron transmission microscope (TEM).
- UV-vis, DLS, ICP-MS, FTIR.
- Gold nanoparticle synthesize.
- Bio-conjugation methods (EDC/NHS, Au-S, Ni-NTA).
- Small angle x-ray scattering (SAXS) operation and data analysis (Argonne National Lab, 2017).

Bioengineering

- Confocal laser scanning microscopy.
- Multiphoton microscopy.
- Primary cell culture: DRG neuron extraction and culture.
- Cell culture: HEK293 cell.
- Animal work: nanoparticle distribution in animal organs by ICP-MS.
- Calcium imaging with fluorescent microscope system and 2-photon imaging system.
- Cell toxicity study: MTT, PI staining, Annexin V, WST-1 assay.

Numerical simulation

- MATLAB (Proficient).
- COMSOL Multiphysics (Proficient).
- Fluid mechanics: ANSYS-Fluent.
- Nanophotonic simulation with MNPBEM, DDA.
- Monte Carlo simulation for light propagation in biological tissue (MCML).
- Solidworks.
- AutoCAD.

HONORS & AWARDS

PhD small grant program. The University of Texas at Dallas. (2016)

REPRESENTATIVE CONFERENCE PRESENTATIONS

1. **Kang, P.**, Li, X., Shiers, I.S., Xiong, H., Giannotta, M., Dejana, E., Price, T.J., Qin, Z., "*In situ* Photo-Inactivation of Proteins by Molecular Hyperthermia," **Summer Biomechanics**, **Bioengineering, and Biotransport Conference (SB^{3}C),** Seven Springs, PA, (2019).
2. **Kang, P.**, Sarkar, D., Qin, Z., "Ultrashort Laser Fragmentation of Plasmonic Gold Nanoparticles: Coulomb Explosion versus Photothermal Evaporation," **SB^{3}C,** Seven Springs, PA, (2019).
3. Youn, J., Kim, P., **Kang, P.**, Qin, Z., Lee, J., "Tyrosine-assisted fluorescent gold nanoclusters for sensing Fe^{3+} and Cu^{2+}", **American Chemical Society National Meeting** (2019).
4. **Kang P**., Sarkar, D., Price, T.J., Qin Z., "Molecular Hyperthermia of Protease-Activated Receptor 2," **NanoEngineering for Medicine and Biology Conference (NEMB)**, Los Angeles, CA, (2018).
5. Sarkar, D., **Kang, P.**, Nielsen, S.O., Qin, Z., "Reaction-Diffusion Kinetics during Selective Photo-Inactivation of Proteins by Molecular Hyperthermia," **NEMB**, Los Angeles, CA, (2018).
6. **Kang P**., Sarkar, D., Price, T.J., Qin Z., "Molecular Hyperthermia: the nal frontier of bio-thermal science," **Photothermal Effects in Plasmonics (PEP18)**, Summer school, Special focus on biology, Porquerolles island, France, (2018).
7. Sarkar, D., **Kang, P.**, Nielsen, S.O., Qin, Z., "Non-Arrhenius Reaction-Diffusion Kinetics for Protein Unfolding, Inactivation and Inhibition Over a Large Temperature Range," **The Bluebonnet Symposium on Thermal Fluid Sciences**, UTD, TX, (2018)

8. **Kang P**., Chen Z., Nielsen S.O., Hoyt K., D'Arcy S. Gassensmith J. J., Qin Z., *Nanosecond Protein Unfolding and Inactivation by Plasmonic Nanoparticle Laser Heating.* **Biophysical Society 61st Annual Meeting**, New Orleans, LA, (2017).
9. **Kang P**., Fall O., Ouyang H., Nielsen S.O., Randrianalisoa J., Qin Z., *Nanosecond Thermal Inactivation of Plasmonic Nanoparticle Laser Heating.* **SB^{3}C,** National harbor, MD, (2016).
10. **Kang P**., Fall O., Ouyang H., Nielsen S.O., Randrianalisoa J., Qin Z., *Nanosecond Thermal Inactivation of Plasmonic Nanoparticle Laser Heating.* **NEMB** Houston, TX, (2016).
11. **Kang P.**, Revuru A. N., Qin Z., *Point-of-care Diagnosis by Nanoparticle Aggregation: Tuning the Sensitivity by Nanoparticle Size and Concentration* **NEMB** Houston, TX, (2016).